OBSERVATIONS OF DISKS AROUND THE YOUNGEST PROTOSTARS: CHARACTERIZING FREQUENCY, DUST PROPERTIES, AND MAGNETIC FIELDS AT THE EARLIEST TIMES

BY

DOMINIQUE M. SEGURA-COX

DISSERTATION

Submitted in partial fulfillment of the requirements
for the degree of Doctor of Philosophy in Astronomy
in the Graduate College of the
University of Illinois at Urbana-Champaign, 2017

Urbana, Illinois

Doctoral Committee:

Professor Leslie Looney, Chair
Professor Charles Gammie
Associate Professor Athol Kemball
Associate Professor Tony Wong

Abstract

Circumstellar disks are fundamental for accretion and angular momentum distribution during the early phases of star formation. Class 0 objects are the youngest protostars and most embedded in their natal envelopes, and circumstellar disks can form even at this earliest stage of star formation. Less-embedded Class I protostars have cleared part of their surrounding envelope, yet the envelopes enshrouding Class 0 and Class I protostars have made detection of young protostellar disks difficult; before this work, only ∼15 total Class 0 and 10 Class I disks were known. While work has begun with Class 0 disks, due to their deeply enshrouded nature, there is still much left to examine regarding disk frequency, disk radii, dust populations, disk evolution, disk structure, and presence of planetesimals in the youngest protostellar disks. Through observational work with the CARMA, VLA, and ALMA telescope arrays towards some of the youngest protostars, this dissertation addresses a variety of important and outstanding questions regarding the frequency, dust properties, and role of magnetic fields at the earliest times.

How is the presence of a young protostellar disk influenced by the magnetic fields of the system? We examine subarcsecond (∼0.35″) resolved CARMA polarization observations of the 1.3 mm dust polarization from the disk around the Class 0 protostar L1527 to understand the inferred magnetic field morphology of the system on 50 AU size scales. L1527 is the first Class 0 protostar with direct detection of linearly polarized dust emission from the circumstellar disk, indicating magnetic fields are aligned perpendicular to the rotation axis of the disk, consistent with disk-wrapped toroidal field lines. By studying disk-scale fields, we can explore if misaligned magnetic fields and rotation axis can allow enough angular

momentum to remain in the system at early times to support a disk.

What is the frequency of large Class 0 and I protostellar disks, and what are their properties? We analyze dust continuum emission data toward all young protostellar disk candidates around Class 0 and I sources in the Perseus molecular cloud from the 8 mm VLA Nascent Disk and Multiplicity (VANDAM) survey with $\sim$0.05″ or 12 AU resolution, revealing 19 new candidate disks in the Class 0 and I phases. The survey of young protostars is the most sensitive and complete survey to-date, allowing us to understand how common large young disks are. Because we lack kinematic data on small scales to confirm any resolved, elongated structures as rotationally supported disks, we fit the deprojected, averaged, and binned data in the u,v-plane to a disk-shaped profile to determine which sources are disk candidates and model disk properties.

How early can disk dust substructures, possible signs of early planet formation, be found in young disks? We study the 1.3 mm ALMA dust continuum of the disk around the Class I source IRS 63 with 7 AU resolution to search for rings and gaps in a young protostellar disk. We found a series of concentric rings and gaps in the disk, centered around the protostar. Gaps are usually attributed to planet-disk interactions, although other phenomena such as volatile snowlines, dead zones, and gravitational instabilities can produce structures in protostellar disks. Previous studies of disk substructure have revealed gaps in only the disks of more evolved Class II sources such as HL Tau. Since rings and gaps are observed in IRS 63, then planet formation or other associated disk sculpting must have started early in the Class I phase or before.

Thank you, Leslie.

Table of Contents

List of Tables

List of Figures

List of Abbreviations

ALMA	Atacama Large Millimeter/submillimeter Array
BIMA	Berkeley-Illinois-Maryland Association Telescope Array
c2d	Cores to Disks Survey
CARMA	Combined Array for Research in Millimeter-wave Astronomy
CASA	Common Astronomy Software Applications Package
CSO	Caltech Submillimeter Observatory
FWHM	Full Width at Half Maximum
IRAS	Infrared Astronomical Satellite
JCMT	James Clerk Maxwell Telescope
MCMC	Markov Chain Monte Carlo
MHD	Magnetohydrodynamics
MIRIAD	Multichannel Image Reconstruction, Image Analysis and Display Package
MRI	Magnetorotational Instabilities
RMS	Root Mean Square
SCUBA	Submillimeter Common-User Bolometer Array
SED	Spectral Energy Distribution
SHARC	Submillimeter High Angular Resolution Camera
SHARP	SHARC-II Polarimeter
SMA	Submillimeter Array
TADPOL	Telescope Array Doing Polarization Survey
VANDAM	VLA Nascent Disk and Multiplicity Survey
VLA	Very Large Array

Chapter 1

Introduction

Many details of the star formation process are still unknown. Star formation spans many orders of magnitude in density and size scale, and studying protostars involves many diverse physical phenomena such as disk rotation, jets and outflows, magnetic fields, dust grain evolution, and planetesimal formation. The earliest discovered objects recognized to be protostars are T Tauri stars. Joy (1942, 1945, 1949) first recognized T Tauri stars as a distinct group of faint objects with optical emission however their protostellar nature was not yet realized. Herbig (1962) argued that T Tauri stars must be young objects because they are elevated above the main sequence in the HR diagram and may correspond to an object on the Hayashi track (Hayashi, 1966), contracting towards the main sequence but not yet burning hydrogen. Herbig (1977) found that the T Tauri stars were associated both spatially and kinematically with the molecular clouds they were presumably born in. Additional groups of protostars were later discovered with infrared and submillimeter observations (e.g., Andre et al., 1993).

Protostellar cores have been observed to be rotating. During the collapse of a rotating core with conservation of angular momentum, a centrifugally-supported circumstellar disk will form (McKee & Ostriker, 2007), surrounded by a larger scale dense infalling envelope. They are observed clearly in T Tauri protostars, as components of the infrared excess in the SED. Slightly older protostars have some remnant material around them, likely the leftovers of a protostellar disk after they have stopped accreting. This remnant disk will likely form a planetary system as the protostar approaches the main sequence, at least around low-mass protostars. For low-mass cores, observed sizes and rotation parameters predict disk

sizes ∼1000 AU in the absence of strong magnetic fields, which is roughly in agreement with observations of the sizes of disk around T Tauri stars with R ∼200 AU (Andrews & Williams, 2005). Disks are also thought to be the driving mechanism behind bipolar collimated jets and wide-angle molecular outflows, which accelerate material away from the protostar and remove angular momentum from the system, and allowing accretion of gas and dust onto the central protostar from the disk.

Bipolar molecular outflows were completely unpredicted by theory when they were discovered (Snell et al., 1980); however they are ubiquitous in the early stages of protostellar formation and in fact lead to the discovery of the first Class 0 object (Andre et al., 1993, see Section 1.1). Observed structure and kinematics of molecular outflows show that there are two outflow components, often both present (Lee et al., 2002): (1) a high-velocity, collimated core seen as a jet and (2) a lower velocity, wide-angled molecular outflow. Highly collimated jets and wide-angled outflows have been typically examined separately but are often observed together in the same source (McKee & Ostriker, 2007). Arce & Sargent (2006) have revealed outflows to become wider and more varied with protostellar age. The widening of the outflow cavity with age, along with infall and accretion of the envelope onto the central protostar, provide a mechanism for the clearing of the envelope as a protostar advances through the evolutionary classes.

1.1 Protostellar Classification

Protostellar SEDs have been typically divided into four empirical classes based on observations. Classes I-III were first introduced by Lada (1987), and Class 0 was introduced later by Andre et al. (1993). Because many wavelength ranges are required to represent a protostellar SED, from the ultraviolet to submillimeter, the whole SED of a source can be difficult to obtain. Infrared observations of protostellar sources in the Ophiuchus molecular cloud from 1-20 μm (Wilking & Lada, 1983; Lada & Wilking, 1984) allowed construction of

infrared SEDs for a large number of sources. From the infrared SEDs alone, Lada & Wilking (1984) noticed that the shapes of the SEDs could be divided into three morphological classes, identified as Class I-III in Lada (1987). These classes were quantified by the slope of the SED over the wavelength range ∼1-20 μm, α_{IR}.

Class I sources have SEDs that are broader than that of a blackbody and rise in wavelengths longer than 2 μm. Quantitatively, the $\alpha_{IR} > 0$ (Lada, 1987). Class I sources are invisible in the optical, and the infrared excess is due to heated grains near the embedded protostellar source. The standard view of Class I objects is a hydrostatic stellar core surrounded by a dense circumstellar disk with a radius of ∼10-100 AU and an infalling envelope $\sim 10^4$ AU in size (Adams et al., 1987).

Class II sources also have distributions that are broader than blackbody distributions, but have either flat or decreasing energy distributions beyond 2 μm, with $-2 < \alpha_{IR} < 0$ (Lada, 1987). These sources are visible in the optical and are thought to be pre-main sequence stars with circumstellar disks and no longer possess a significant envelope. The SED is dominated by optical and near infrared emission from the exposed protostar with infrared excess from the circumstellar disk. Because the Class II sources maintain their disk but have lost their envelope, they are considered to be a later stage of evolution than Class I objects.

Class III sources have energy distributions that resemble reddened blackbodies with very little infrared excess and emit almost entirely in the optical. Like Class II sources, Class III sources have SEDs with slopes decreasing in the infrared however the Class III slope is steeper, with $-3 < \alpha_{IR} < -2$ (Lada, 1987). Class III sources are pre-main sequence stars that no longer accrete significant amounts of mass from the envelope and have accreted most of their disk mass.

With submillimeter observations, Andre et al. (1993) found that a CO bipolar outflow emanated from the symmetric, cold clump VLA 1623 that could only indicate that the clump was an extremely young protostar. The submillimeter emission revealed a ∼1000 AU circumstellar structure where infrared observations showed no compact emission from the area.

Andre et al. (1993) suggested that because this source was invisible in the infrared yet strong in the submillimeter, it made up an entirely new class of objects called Class 0 protostars. Class 0 sources are undetectable at $\lambda < 10$ μm (and hence cannot be classified with α_{IR}). Protostars are thought to assemble most of their mass in the Class 0 phase of evolution (McKee & Ostriker, 2007). Because Class 0 objects are so heavily obscured, their emission tends to peak in centimeter wavelengths. The emission at (sub)millimeter/centimeter wavelengths is entirely from warm dust, which enshrouds the protostellar core and re-radiates absorbed energy. Class 0 sources are assumed to be even younger than Class I sources, due to the complete lack of infrared emission.

The Class 0 sources cannot be classified using the infrared, SED slope α_{IR}. One alternative method is the bolometric temperature (Myers & Ladd, 1993). The bolometric temperature (T_{bol}) of a source is the temperature of a blackbody with the same average frequency as the SED of the source. Since the SEDs of each class of protostar all have different spreads in wavelength and different peak temperatures, each source should have a different bolometric temperature. Chen et al. (1995) found that T_{bol} increased monotonically from Class 0 to Class III sources and so must indicate an evolutionary development of Class 0 $\rightarrow$ Class I $\rightarrow$ Class II $\rightarrow$ Class III. Protostars with known SED classes were found to have the following T_{bol} ranges:

$$\text{Class 0: } T_{bol} < 70 \text{ K}$$

$$\text{Class I: } 70 < T_{bol} < 650 \text{ K}$$

$$\text{Class II: } 651 < T_{bol} < 2280 \text{ K}$$

$$\text{Class III: } T_{bol} > 2880 \text{ K}.$$

Because the bolometric temperature system of classification can encompass all four protostellar classes, where the SED slope can only accommodate Classes I-III, T_{bol} is widely used as an evolutionary indicator, especially when working with the youngest protostars.

1.2 Sparse Observational Evidence of Disks in the Class 0 and I Phases

Theoretically the formation of protostellar disks is expected due to conservation of angular momentum during core-collapse in the very earliest phases of star formation (Terebey et al., 1984). Even small rotational velocity gradients in the initial prestellar core will result in high rotational velocities at disk size scales as the material collapses inwards. Disks do appear observationally to be a pervasive feature of protostars: they are observed clearly in Class II and Class III sources with ∼100 total well-studied disks (e.g., Andrews et al., 2009, 2010). While much is now known about evolved protoplanetary disks, in the younger Class 0 and Class I phases of star formation there is currently sparse observational evidence of circumstellar disks.

Direct observations of protostellar disks in the embedded phases, especially the Class 0 phase, were not possible until (sub)millimeter interferometers such as the BIMA, SMA, CARMA, and ALMA telescopes were constructed. These facilities are capable of directly detecting embedded circumstellar disks because ∼mm wavelengths are required to penetrate through the dense envelope by spatially resolving out the large scale structure with the interferometer, and sub-arcsecond resolution is required to spatially resolve disks. In the past, surveys of the youngest protostars with BIMA, SMA, and CARMA have revealed compact dust emission around Class 0 and I protostars that cannot be explained by envelope surface density distributions alone (e.g., Looney et al., 2000; Jørgensen et al., 2009; Enoch et al., 2011). The excess emission not explained by envelope emission is interpreted as emission from highly embedded disks. In addition, molecular line observations with the SMA have traced barely-resolved rotational signatures of disks in some compact structures around Class I protostars and a bright Class 0 protostar (Jørgensen et al., 2009; Tobin et al., 2012). Now with ALMA, continuum and molecular line observations of Class 0 and I protostars with higher resolution than ever before can be conducted, which spatially filter out even more of

the envelope emission and better resolve rotational velocity gradients.

The details of dust and gas disks around Class 0 and I sources have hence just begun to be studied observationally. Keplerian rotation is a tell-tale sign of true, rotationally supported disks that exist for long enough timescales to form planets; flattened structures without rotation quickly collapse inward (e.g., Ohashi et al., 2014). Keplerian rotation has been clearly detected with (sub)millimeter gas kinematic information in disks around only 4 total Class 0 protostars (Ohashi et al., 2014; Tobin et al., 2012; Murillo et al., 2013; Codella et al., 2014; Yen et al., 2017); however, they are bright disks and may not represent typical disks at this stage of evolution. Class I protostars have longer lifetimes and have cleared enough of their mass reservoir that more Class I disks with Keplerian rotation have been detected ($\sim$10 total; Harsono et al., 2014) than in Class 0 systems, though not nearly as many as in Class II sources. The first discovered Class 0 disk, L1527 (Tobin et al., 2012), was revealed to have R $\sim$50 AU (Ohashi et al., 2014) through using centimeter interferometry to spatially resolve out the larger envelope. The other Class 0 protostellar disks are VLA 1623 with R $\sim$189 AU (Murillo et al., 2013), Lupus 3 MMS with R $\sim$100 AU (Yen et al., 2017), and HH212 with R $>$30 AU (Codella et al., 2014).

The existence of these 30-100 AU disks in the Class 0 and I phases is somewhat puzzling when magnetic fields are taken into account. Initial theoretical studies of disk formation with magnetic fields encountered the magnetic braking problem, where ionized particles are flux-frozen into the magnetic field which runs parallel to the rotation axis; as the magnetic field lines are wrapped around the rotating protostar, magnetic forces exert torques on envelope material and transport angular momentum away from the central protostar. Due to the magnetic braking problem, rotationally-supported disk formation was nearly completely suppressed (e.g., Allen et al., 2003; Mellon & Li, 2008; Hennebelle & Fromang, 2008). Including non-ideal MHD effects allowed disk formation, though magnetic braking was still so effective for Class 0 protostars that disk radii were theoretically limited to $<$10 AU (Dapp & Basu, 2010), with disks growing to R $\sim$100 AU sizes at the beginning of the Class II

stage when there is less envelope material and magnetic braking is inefficient (e.g., Dapp et al., 2012; Mellon & Li, 2009; Machida et al., 2011). The relatively large sizes of the so-far observed Class 0 disks could be a consequence of misalignment between the magnetic field and rotation axis, which theoretically modifies the strength of magnetic braking and allows formation of $R \sim$100 AU disks in the Class 0 phase (Hennebelle & Ciardi, 2009; Joos et al., 2012; Krumholz et al., 2013). Of course, the majority of yet-undetected Class 0 disks could be small, <10 AU, and in agreement with the non-ideal MHD models with magnetic fields parallel to the rotation axis of the disk. More observations of Class 0 disks and magnetic fields associated with them are necessary to understand the role of magnetic fields in disk growth at early times.

1.3 Disks as Sites of Planet Formation

Exoplanets appear to be extremely common, with over 4,000 planet candidates detected by the Kepler Mission so far (Coughlin et al., 2016). Even though planet (and planetesimal) formation is clearly typical in circumstellar disks, the exact formation mechanism remains unknown. Planetesimals are generally not directly detectable, and indirect evidence of their existence such as observations of substructure—radial and azimuthal variations in the disk surface density profile—are required. Circumstellar disks of dust and gas set the initial physical conditions to grow small dust grains into planetesimals, as well as how solid planets form from planetesimals. Even once solid planets form, the disk continues to contribute to planet formation by providing the gas reservoir to create gas giant planet atmospheres (e.g., Bromley & Kenyon, 2011). Already, problems have been encountered with forming planets from protoplanetary disks. Solids encounter a headwind in the disk as they orbit, removing angular momentum from the solid particles and causing inspiral, which is most efficient when solids are in the millimeter to meter size range. This phenomena poses a problem in forming larger solids such as planet-sized bodies and is known as the mass accretion problem, or

"meter-size barrier," of planetesimals (Weidenschilling, 1977). More observational information about the initial conditions for planet formation is required to understand exactly how planetesimals accrete their mass at early times.

Substructures such as gaps, holes, and asymmetries have been long-known in older (mostly transition) disks around pre-main sequence stars (e.g., Calvet et al., 2005; Piétu et al., 2006; Espaillat et al., 2007, 2008; Hughes et al., 2009; Casassus et al., 2013; van der Marel et al., 2013; Pérez et al., 2014). Spiral structures are also possible in disks around protostars, with spirals from disk fragmentation in a Class 0 protostellar disk (Tobin et al., 2016a) and spiral density waves in a Class II disk (Pérez et al., 2016). ALMA observations of concentric rings and gaps in protostellar disks have only been observed in disks more evolved than the Class 0 and I phases including the Class II protostar HL Tau (ALMA Partnership et al., 2015), Herbig Ae star HD 163296 (Isella et al., 2016), TW Hydrae (Andrews et al., 2016), and AA Tau (Loomis et al., 2017). Even though observations of substructure in disks around the youngest protostars can give initial conditions for planet-forming disks around protostars closer to the main sequence, so far substructure has been reported in the disk of only one protostar from either the Class 0 or I phases (L1448 IRS3B; Tobin et al., 2016a).

The Class 0 and I protostellar stages have the largest mass reservoirs available to form disks and planetesimals; therefore understanding the properties of disks and their substructures at the earliest possible epochs is necessary to determine the formation mechanism behind circumstellar disks and the initial pathway to planet formation. Alternative to planet-disk interactions, other phenomena that produce disk substructures (both axisymmetric gaps or non-symmetric features like spirals) including volatile snowlines, magnetized disks, and gravitational instabilities (e.g., Zhang et al., 2015; Flock et al., 2015; Takahashi & Inutsuka, 2014) may be at work. Substructures such as sharp jumps in surface density or rings can reveal information about different radial zones of dust grain growth, and observational evidence of the existence of large, pebble-sized dust grains at early times could help explain how to overcome the or meter-size barrier of planetesimals (Weidenschilling,

1977). Analysis of disk substructure can both reveal signs of disk-planet interactions and determine properties of dust grain growth, which ultimately leads to planetesimal growth and eventually planet formation. More observations of dust substructures in the Class 0 and I phases are required to provide information on initial conditions for planetesimal growth, chemical freeze-out in the disk, and presence of instabilities in disks around protostars at early times.

Chapter 2

The Magnetic Field in the Class 0 Protostellar Disk of L1527

We present subarcsecond ($\sim$0.35″) resolved observations of the 1.3 mm dust polarization from the edge-on circumstellar disk around the Class 0 protostar L1527. The inferred magnetic field is consistent with a dominantly toroidal morphology; there is no significantly detected vertical poloidal component to which observations of an edge-on disk are most sensitive. This suggests that angular momentum transport in Class 0 protostars (when large amounts of material are fed down to the disk from the envelope and accreted onto the protostar) is driven mainly by magnetorotational instability rather than magnetocentrifugal winds at 50 AU scales. In addition, with the data to date there is an early, tentative trend that R >30 AU disks have so far been found in Class 0 systems with average magnetic fields on the 1000 AU scale strongly misaligned with the rotation axis. The absence of such a disk in the aligned case could be due to efficient magnetic braking that disrupts disk formation. If this is the case, this implies that candidate Class 0 disk systems could be identified by the average magnetic field direction at $\sim$1000 AU spatial scales.

2.1 Introduction

Circumstellar disks are a key component of the star formation process and are fundamental for accretion and angular momentum distribution during the early phases of star formation. Class 0 objects are the youngest and most embedded protostars, and circumstellar disks form at this earliest stage of star formation if angular momentum is conserved during cloud collapse

This chapter is published in the The Astrophysical Journal Letters as Segura-Cox, D. M., Looney, L. W., Stephens, I. W., et al. 2015, ApJ, 798, L2

(e.g., Cassen & Moosman, 1981). Class 0 disks are extremely obscured by envelopes, which contribute $\gtrsim$90% of the total emission (Looney et al., 2000), making the search for Class 0 disks challenging. However, observations of Class 0 disks and their properties are essential to provide the initial conditions for mass accretion onto the central protostar and planet formation. To date, only a few Class 0 systems have observed disks with clear Keplerian rotation (e.g., Tobin et al., 2012; Murillo et al., 2013; Codella et al., 2014); L1527, VLA 1623, and HH212 have Keplerian disks with R >30 AU, sizes larger than magnetic braking models predict.

In addition to the properties of young disks and envelopes, the morphology and strength of the magnetic field in these systems also play an important role in star formation (e.g., Crutcher, 2012). For example, the morphology of the magnetic field in the young disk provides important clues into angular momentum transport: disk accretion driven by magnetorotational instabilities (MRI, Balbus & Hawley, 1998) favor toroidal fields while angular momentum removal via magnetocentrifugal winds arising from the disk favor poloidal fields (e.g., Blandford & Payne, 1982). The magnetic field morphology in the envelope and disk can be inferred; dust grains preferentially align with their long-axis perpendicular to the magnetic field, causing the dust emission to be polarized (e.g., Lazarian, 2007). An interferometric survey of dust polarization around 26 low-mass Class 0/I protostars has been recently conducted (TADPOL, Hull et al., 2013, 2014). For these sources, the average magnetic field axes are generally misaligned with the rotation axes of the systems (as proxied by the outflow). In the case of L1527 and VLA 1623, TADPOL observations show that the magnetic field lines are perpendicular to the outflows. However, the TADPOL results only probe envelope size scales and do not approach disk scales. The magnetic field morphology on smaller scales has been observed in the Class 0 protostars L1157 and IRAS 16293-2422 B. L1157, whose disk is yet to be resolved and has R <20 AU (Tobin et al., 2013c), has vertical poloidal component magnetic fields aligned with the rotation axis of the system in the inner envelope (Stephens et al., 2013). IRAS 16293-2422 B—which is thought to have a face-on

disk and hence no clear Keplerian motion—has resolved observations of the candidate disk with a polarization pattern indicative of a toroidal magnetic field component (Rao et al., 2014), although the face-on geometry makes the detection of any vertical poloidal component impossible.

In this Chapter, we present high-resolution CARMA 1.3 mm dust polarimetric observations of the Class 0 protostar L1527. Lower-resolution CARMA 1.3 mm polarimetric observations of L1527 were previously conducted as a part of the TADPOL survey, probing the magnetic field morphology on ∼1000 AU envelope size scales. Here we report the magnetic field morphology on ∼50 AU disk size scales. The data presented are the first detection of polarized dust emission emanating directly from a Class 0 Keplerian disk.

2.2 Observations

CARMA 1 mm full-Stokes observations of L1527 were obtained in 6 tracks of the B array (∼0.35″ resolution) from 2013 December 9–13 and 15 for a total of 21 hours on-source. The correlator was set up with a local oscillator frequency of 233.731 GHz and four 500 MHz-wide bands centered at intermediate frequency values of 2.187, 2.740, 4.716, and 5.544 GHz. We used the MIRIAD software package (Sault et al., 1995) to reduce the data. The polarization calibration followed the standard process for CARMA (Hull et al., 2014). The phase and polarization leakage calibrator for all tracks was 0510+180. The preferred bandpass calibrator was 3C84, and 3C454.3 was used when 3C84 was unavailable. For most tracks, the flux calibrator was MWC349 with a calibration accuracy estimation of ∼15%, but only statistical uncertainties are considered in this Chapter. When this calibrator was not observed, the flux was interpolated from the observations of MWC349 in other tracks. To maximize sensitivity, maps of the 4 Stokes parameters (I, Q, U, and V) were created using natural weighting. From these, we derive the polarization position-angle and intensity maps. We also generated new maps of L1527 data from the TADPOL survey (Hull et al., 2014). The

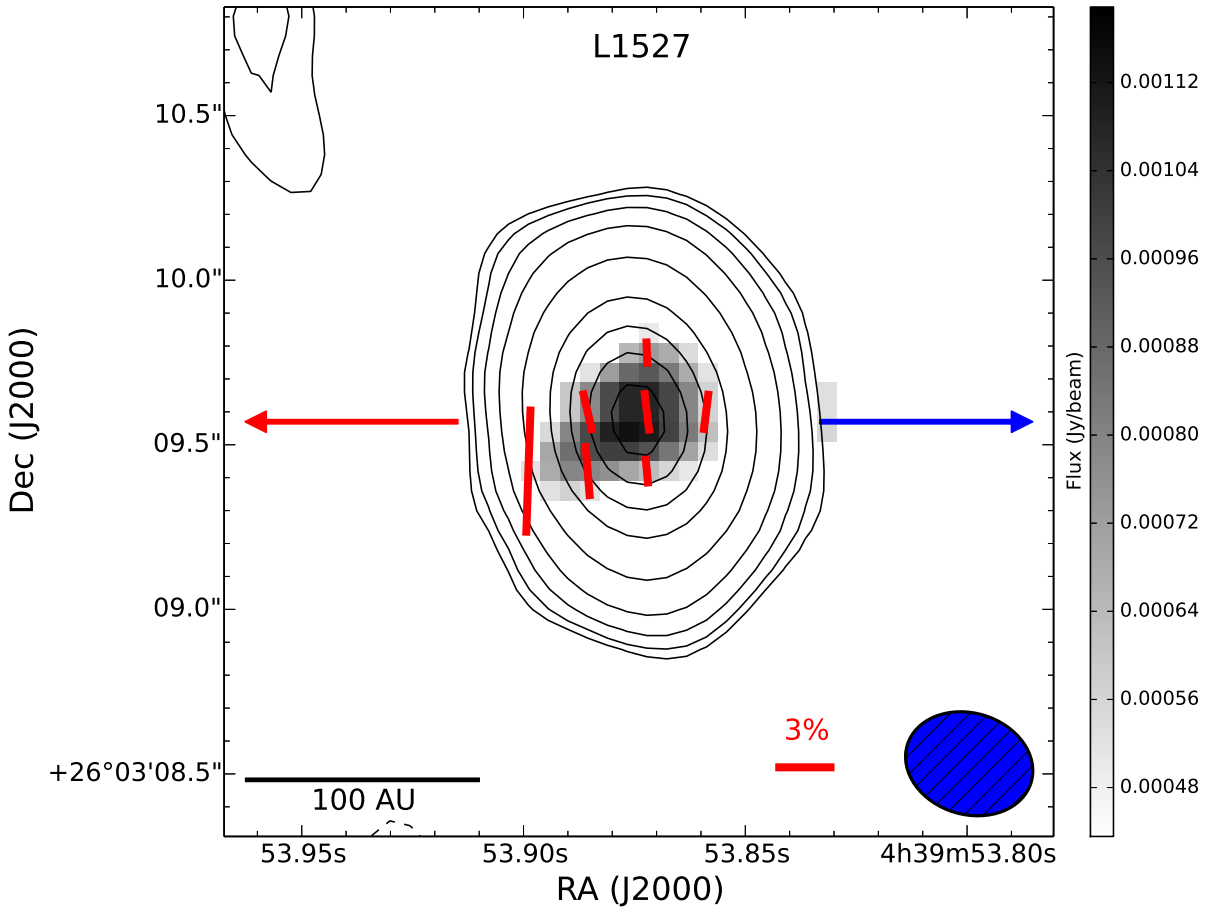

Figure 2.1 Polarimetric map (polarization vectors rotated by 90° to show inferred magnetic field orientation) of the L1527 disk from CARMA data with a 0.39″×0.31″ beam. Fractional polarization vectors ≥3σ displayed. Contours are Stokes I data with levels of [-6, -4, -3, 3, 4, 6, 10, 20, 40, 60, 80, 100]×σ, σ=0.45 mJy beam^{-1}. Grayscale shows the polarized intensity ≥3σ. Outflows in the plane of the sky are marked by red and blue arrows.

data include 5 tracks between 2011 May and 2013 April in D and E arrays.

2.3 Results

The 1.3 mm dust emission map of L1527 is presented in Figure 2.1 and is consistent with the known edge-on disk (Tobin et al., 2013a). The disk has been resolved previously at 3.4 mm and 870 μm (Tobin et al., 2012) and also has been shown to have Keplerian motion and a radius of 54 AU (Ohashi et al., 2014). Our observations are the first resolved detection of the disk at 1.3 mm. At a resolution of ∼0.35″ and a distance of 140 pc (Loinard et al.,

2007), our interferometric observations probe L1527 on size scales of ∼50 AU. An elliptical Gaussian fit to the high-resolution 1.3 mm Stokes I data measures a deconvolved size of $0.53'' \times 0.23''$ with position angle of 5.2° (PA, measured counterclockwise), consistent with the deconvolved sizes at 3.4 mm, 870 μm (Tobin et al., 2013a), and 1.3 mm (Ohashi et al., 2014). In addition, our flux density at 1.3 mm (139±4 mJy) is consistent with detection of the L1527 disk seen in Tobin et al. (2013a). Using the measured fluxes at 3.4 mm and 870 μm and the derived β=0 from Tobin et al. (2013a), we can estimate the expected disk emission at 1.3 mm (116 mJy and 96 mJy, respectively), which is congruent with our measured 1.3 mm fluxes when taking account a 20% extrapolating and amplitude uncertainty. Based on this evidence, our observations are dominated by disk emission of the L1527 system, with little contamination from the large-scale envelope emission.

We detect dust polarization of the young disk over 2 synthesized beams with an average polarization of 2.5%±0.6% and a position angle of 5°±5° measured counterclockwise from north, aligning well with the Stokes I elliptical Gaussian fitted position angle of 5.2°±0.4°. The inferred magnetic field (with polarization vectors rotated by 90°) is shown in Figure 2.1. The morphology of the inferred field is parallel to the disk axis, as is expected from an edge-on toroidal field—uniform and aligned with the disk. We compare a uniform field at a 5° PA (the same as the dust emission) to the data and find a reduced $\chi^2 < 1$. The polarization fraction of the circumstellar disk of L1527 is larger than the 1.4% polarization fraction found in the face-on candidate disk of IRAS 16293-2422 B (Rao et al., 2014), although the lower polarization fraction of IRAS 16293-2422 B may be due in part to beam-averaging; due to orientation, an edge on toroidal field is less beam-averaged as the vectors are more uniform. Our polarization percentage is similar to the theoretically predicted 2-3% polarization fraction found in simulations of magnetized disks (Cho & Lazarian, 2007). On the other hand, observations of the disks of older T Tauri systems have much lower polarization percentages <1% (Hughes et al., 2009, 2013), which may be an outcome of dust processing or de-alignment mechanisms during disk evolution (Stephens et al., 2014).

A uniform field in the plane of the disk is physically unlikely for a rapidly-rotating, Keplerian disk system. One expects either poloidal, toroidal, or a combination of the two in such a disk (e.g. Balbus & Hawley, 1998; Konigl & Pudritz, 2000). For an edge-on disk, observations are most sensitive to vertical poloidal field components because they are expected to vertically thread the disk and thus lay roughly in the plane of the sky. However, our data does not exhibit any obvious poloidal morphology which would be perpendicular to the disk. To show that a toroidally dominant morphology is consistent with our observations, we compare to a purely toroidal, a purely vertical poloidal, and combinations of toroidal and vertically poloidal toy models (see captions of Figures 2.2 though 2.7 for details). We used the best-fit disk parameters of Tobin et al. (2013a): disk inclination angle of 85°, 0° PA, $M_{disk} = 0.0075\ M_{\odot}$, $R_{inner} = 0.1$ AU, $R_{outer} = 125$ AU, and stellar and accretion luminosity of 2.75 $L_{\odot}$. The temperature distribution was calculated using the Monte-Carlo radiative code RADMC-3D (Dullemond & Dominik, 2004). The Stokes I, Q, and U maps were numerically solved using dust radiative transfer in the disk along the line of sight with an assumed constant polarization fraction. The magnetic field vectors at each integral element have been tilted and rotated based on the inclination and position angles of the disk model. Finally, all maps are convolved with the synthesized beam from the polarization observations (for more details see Stephens et al., 2014). As shown in Figures 2.2 though 2.7, the detected polarization is characterized well by our toroidally dominant toy models with up to 40% poloidal field (Figures 2.2, 2.3, 2.4), with a reduced χ^2 $\sim$1.8 for all three cases as fit to the morphology in the image plane with the vectors shown in Figure 2.1. The scenarios where the vertical poloidal component is equally strong as the toroidal component (Figure 2.5) or the vertical poloidal component is dominant (Figures 2.6, 2.7) do not reproduce the observed magnetic field morphology. The purely toroidal simple model exhibits more extensive polarization than the observations, which is likely due to our assumption of constant polarization in the disk.

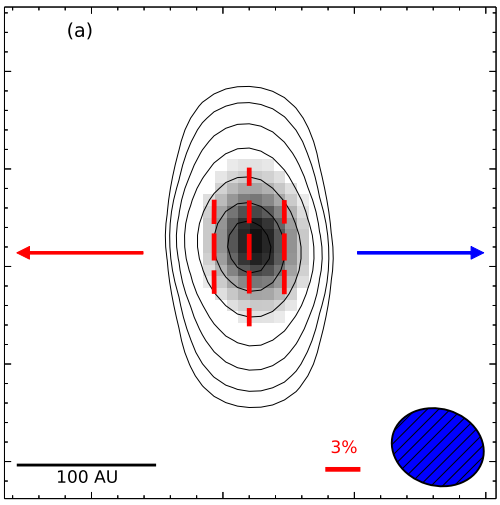

Figure 2.2: Toroidal field only synthetic map of the L1527 disk magnetic field morphology. Contours, grayscale, and vectors are the same as Figure 2.1.

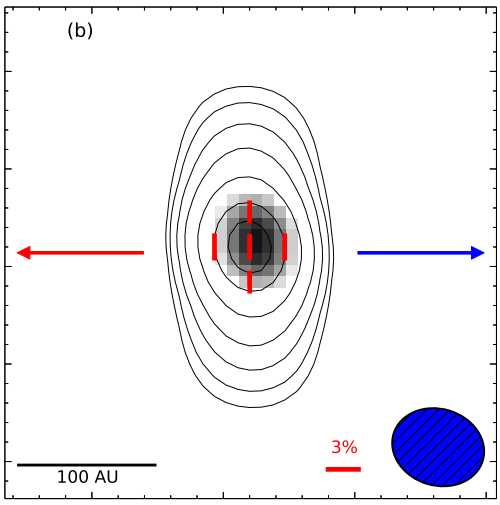

Figure 2.3: Same as Figure 2.1 for 70% toroidal/30% vertical poloidal field.

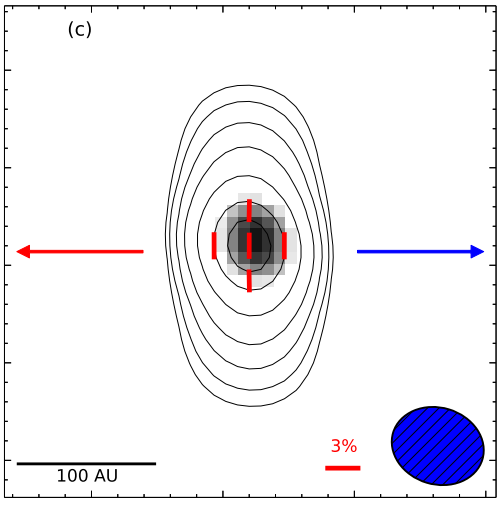

Figure 2.4: Same as Figure 2.1 for 60% toroidal/40% vertical poloidal field.

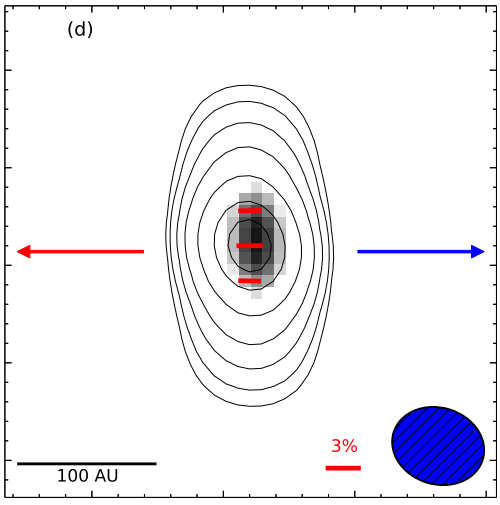

Figure 2.5: Same as Figure 2.1 for 50% toroidal/50% vertical poloidal field.

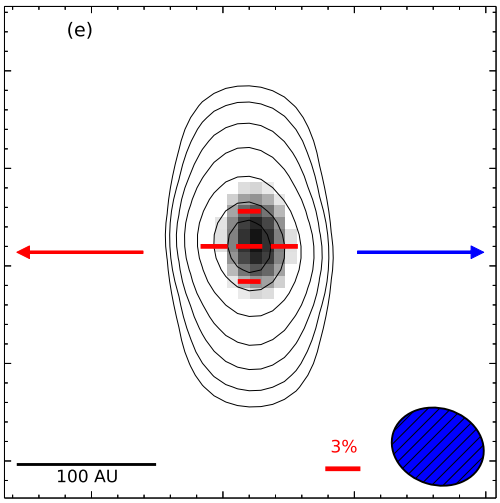

Figure 2.6: Same as Figure 2.1 for 40% toroidal/60% vertical poloidal field.

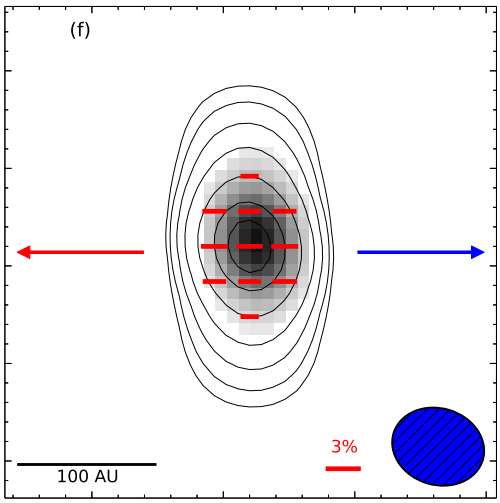

Figure 2.7: Same as Figure 2.1 for vertical poloidal field only.

2.4 Discussion

In quiescent (non-turbulent) systems with aligned magnetic field and disk rotation axes, magnetic braking can have a significant effect on the infalling material in the ideal MHD limit, removing angular momentum (Mellon & Li, 2008; Hennebelle & Fromang, 2008), and suppressing growth of the early circumstellar disk by allowing larger accretion rates (Li et al., 2011). A differential movement of flux-frozen magnetic field lines at different radii causes twisted magnetic field lines, which create a braking torque on the faster-rotating inner material and inhibit the formation of large, rotationally supported disks. Magnetic braking can be so effective in Class 0 sources that rotationally supported disks are limited to R <10 AU, where centrifugal balance is achieved in axisymmetric resistive MHD calculations (e.g., Dapp & Basu, 2010); centrifugal balance is a necessary condition for the formation of a protostellar disk. Other theoretical studies indicate that disks only reach R$\sim$100 AU at the end of the main mass accretion phase when the envelope is less massive and magnetic braking becomes inefficient (e.g., Dapp et al., 2012; Mellon & Li, 2009; Machida et al., 2011). Conversely to this prediction, Keplerian disks have been detected in Class 0 sources with sizes larger than expected from magnetic braking models. L1527 and VLA 1623 have disk

sizes of R∼54 AU and R∼189 AU respectively (Ohashi et al., 2014; Murillo et al., 2013), and HH212 has a disk of R >30 AU (Codella et al., 2014).

There are large disks in some young systems, suggesting that significant magnetic braking has not happened, has already occurred, or the magnetic field has diffused to the point where a R >10 AU disk could form. On the other hand, similar high resolution observations of the Class 0 protostar L1157 have not detected a circumstellar disk down to spatial resolutions of ∼15 AU (Tobin et al., 2013c). This result suggests that magnetic braking may have been more significant in L1157 than L1527. Of course, there are differences in age since L1527 is an older source and could have been classified as a Class I source, were it not viewed edge-on (Tobin et al., 2008). What is clear is that some Class 0 sources have R >10 AU circumstellar disks and others do not. Such differences in disk size could be a consequence of misalignment between the magnetic field and rotation axis, which modifies the strength of magnetic braking in simulations with detailed analysis of angular momentum transport in collapsing cores (Hennebelle & Ciardi, 2009; Joos et al., 2012; Li et al., 2013; Krumholz et al., 2013).

Table 2.1: B array and TADPOL Results

Data Set	Stokes I Flux (mJy)	Polarized Flux (mJy)	$\bar{P}_{\%}$ (%)	PA °	Beam ($''$)
B array	139±4	1.1±0.2	2.5±0.6	5±5	0.39×0.31
TADPOL	188±5	2.3±0.3	2.8±0.7	1±5	2.63×2.26

Uncertainties are statistical. Results were found using data >3σ. Position angles are measured counterclockwise. Stokes I flux is measured across the entire disk or inner envelope; polarized flux and $\bar{P}_{\%}$ are measured in the polarized region only.

To better understand the role of the magnetic field in the early disk and envelope, we can compare the magnetic field of L1527 presented here with the larger-scale magnetic field detected with TADPOL (Figure 2.8 and Table 2.1). When comparing the polarization at 1000 AU and 50 AU, the two scales have the same average field angle: perpendicular to the outflow and well aligned with the disk plane. The higher resolution observations have less

than half of the polarized emission, which suggests we are resolving out large-scale emission. The projected field morphology on the 1000 AU scale is consistent with the view that the initial magnetic field on this scale is greatly misaligned with respect to the rotation axis, although it is also possible that the field on this scale is already modified by the collapsing and rotating motions in the envelope. The magnetic fields on even larger scales are expected to be affected less by rotation and collapse, and are more likely to keep their initial configuration. The fields are better traced by single dish observations using SHARP on CSO Davidson et al. (2011) and SCUPOL on JCMT (Figure 17 of Hull et al., 2014; Matthews et al., 2009). These single dish data are modeled by Davidson et al. (2014) together with CARMA

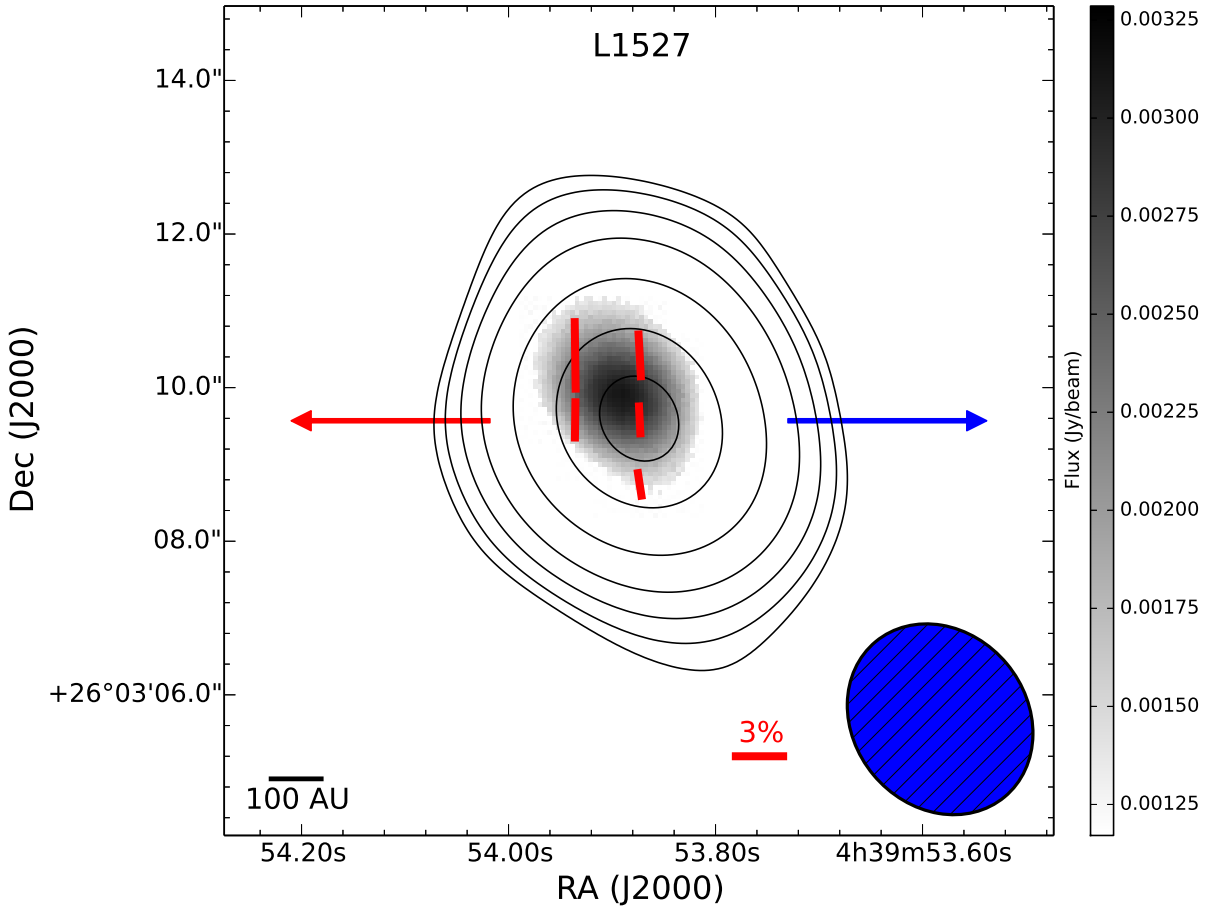

Figure 2.8 Polarimetric map of the L1527 inner envelope from the CARMA TADPOL data with a 2.63″×2.26″ beam. Contours are Stokes I data with levels of [-6, -4, -3, 3, 4, 6, 10, 20, 40, 60, 80, 100]×σ, σ=2.34 mJy beam^{-1}. Grayscale and vectors are the same as Figure 2.1.

data; we refer the reader to that paper for a detailed discussion of the magnetic field on large-scales. In any case, on the small scale of the disk, the available data are consistent with the field being predominantly toroidal, and such a toroidally dominant disk magnetic field is also consistent with the magnetorotational instability (e.g., Balbus & Hawley, 1998) driving accretion during the main accretion phase. We do not detect significant vertical poloidal component fields that are needed to launch magnetocentrifugal winds; such winds are probably not the dominant driver of angular momentum transport during the main accretion phase at the $\sim$50 AU size scale. On the other hand, a disk wind would likely be launched from the disk upper layers that are not well traced by our observations, which are most sensitive to the dust in the midplane. If the poloidal field is somehow limited to the surface layers, then our observations would be less constraining on the existence or absence of a disk wind.

Table 2.2: Class 0/I Magnetic Field Morphologies and Candidate Disks

Source	α (J2000)	δ (J2000)	Class	Mag-Rot-Axis[a]	Evidence of Disk?	References
L1551 NE	04:31:44.5	18:08:31.5	I	Perpendicular	Yes[b,c]	1,7
L1527	04:39:53.9	26:03:09.6	0	Perpendicular	Yes[b]	2,7
IRAS 16293-2422 B	16:23:22.9	-24:28:35.7	0	Perpendicular	Yes	3
VLA 1623	16:26:26.4	-24:24:30.5	0	Perpendicular	Yes[b]	4,7
NGC 1333-IRAS 4A	03:29:10.5	31:13:31.3	0	Unaligned, 40°	Yes	5,8
HH 211 mm	03:43:56.8	32:00:50.0	0	Unaligned, 48°	Yes	5,8
NGC 1333-IRAS 2A	03:28:55.6	31:14:37.0	0	Perpendicular	Yes	5,7
L1157	20:39:06.2	68:02:15.8	0	Parallel	No	6,7

Notes: [a] Orientation of the magnetic field compared to the rotation axis of the system.
[b] Confirmed Keplerian disk. [c] Disk is circumbinary.

References: (1) Takakuwa et al. (2012); (2) Tobin et al. (2012); (3) Rao et al. (2014); (4) Murillo & Lai (2013); (5) Segura-Cox et al. (2016); (6) Tobin et al. (2013c); (7) Hull et al. (2014); (8) Hull et al. (2013)

With dust polarization observations and high-resolution searches for disks, we can compare the magnetic field orientations and morphologies with disk properties. L1527, VLA 1623, L1157, and NGC 1333-IRAS 2A, along with other embedded disk systems (also see Table 2.2), have been observed with CARMA dust polarization at 500 AU or better resolution (Stephens et al., 2013; Hull et al., 2014). L1527 and VLA 1623, the only two systems with known Keplerian disks to-date, have average magnetic fields perpendicular to the rotation axes (inferred from the outflow). In contrast, L1157, a system with a disk R <15 AU in size, has an inferred average magnetic field parallel to the rotation axis. NGC 1333-IRAS 2A also has an inferred magnetic field parallel to the rotation axis of the system and has also been observed with the Very Large Array, detecting circumstellar structure with a resolution of ∼12 AU (Segura-Cox et al., 2015). Although we have few examples so far (Table 2.2), this observational, tentative trend is intriguing and suggested from theory (e.g., Joos et al., 2012); the magnetic field morphology at the earliest stages of collapse may play an important role in the formation of the earliest disk, with strongly misaligned magnetic fields and rotation axes producing R >10 AU disks at early times. Clearly more objects are necessary to better establish this relationship.

We therefore suggest that the morphology of the magnetic field in the inner envelope (∼1000 AU, TADPOL scales) could be another method to help identify candidate Class 0 disk sources with R >10 AU. Sources with R >10 AU disks may have a projected magnetic field on the 1000 AU scale perpendicular to the rotation axis, and the magnetic field would appear uniform for edge-on disk cases like L1527. At more oblique viewing angles at high resolution, a purely toroidal field would be observed as two maxima of fractional polarization along the axis of rotation on either side of the protostar, with the magnetic field oriented perpendicular to the outflow axis within the maxima regions (e.g., see Figure 1 in Hughes et al., 2013). A purely toroidal disk field observed directly down the rotation axis will appear as a pattern of concentric circles (e.g., Padovani et al., 2012). Sources with R <10 AU disks may have dominant vertical poloidal component fields misaligned with the axis of rotation,

as is the case with L1157 with a characteristic hourglass pinch near the protostar. Such a poloidal morphology observed at viewing roughly perpendicular to the rotation axis of the system can appear either symmetric or asymmetric on either side of the pinch (Kataoka et al., 2012), especially for more oblique viewing angles: L1157 has a slight asymmetry. When a purely poloidal field is observed directly down the rotation axis, the poloidal pinch is not observed, but rather has a convergent, spoke-like morphology. In the extreme cases of purely toroidal and purely poloidal magnetic field components, the observed morphology alone can be used to distinguish between the two cases and point towards R >10 AU candidate Class 0 disks.

2.5 Conclusions

L1527 is the first Class 0 protostar with a known Keplerian disk and direct detection of linearly polarized dust emission from the circumstellar disk, indicating magnetic fields are aligned perpendicular to the rotation axis of the disk. The magnetic field is consistent with toroidally dominant field lines. It may be that L1527's large disk arises from the strongly misaligned rotation axis and magnetic field on large scales, while aligned rotation axes and magnetic fields inhibit disk formation on R >10 AU scales. The toroidally dominant field morphology favors the magnetorotational instability (Balbus & Hawley, 1998) as the dominant angular momentum transport process in Class 0 circumstellar disks.

L1527 is one of two Class 0 sources (with VLA 1623) where both magnetic fields and Keplerian disks have been detected. Both of these sources have perpendicular magnetic fields and rotation axes (Murillo & Lai, 2013; Tobin et al., 2012; Hull et al., 2013) on 1000 AU scales. The alternative case is where the magnetic field and rotation axes are parallel on envelope scales, such as the Class 0 source L1157 with no disk detected down to 20 AU (Tobin et al., 2013c). It is possible that aligned magnetic fields may have braked rotation so efficiently as to inhibit the disk formation and growth at early times. The magnetic

field morphology during early collapse may play an important role in the formation of the youngest disks, with strongly misaligned magnetic fields and rotation axes forming large disks at early times. The tentative trend of misaligned magnetic field and rotation axes in Class 0 systems with disks is suggestive and expected from theory, requiring follow-up to make hard conclusions about Class 0 disk formation.

We thank Chat Hull and Dick Plambeck for assistance with data reduction. This research made use of APLpy, an open-source plotting package for Python hosted at http://aplpy.github.com.

Support for CARMA construction was derived from the states of California, Illinois, and Maryland, the James S. McDonnell Foundation, the Gordon and Betty Moore Foundation, the Kenneth T. and Eileen L. Norris Foundation, the University of Chicago, the Associates of the California Institute of Technology, and the NSF. Ongoing CARMA development and operations are supported by the NSF under a cooperative agreement and by the CARMA partner universities.

J. Tobin acknowledges support provided by NASA through Hubble Fellowship grant #HST-HF-51300.01-A awarded by the STScI, which is operated by AURA, Inc., for NASA, under contract NAS 5-26555. The NRAO is a facility of the NSF operated under cooperative agreement by Associated Universities, Inc.

Z.-Y. Li is supported in part by NASA 14AB38G and NSF 1313083.

Chapter 3

The VLA Nascent Disk and Multiplicity Survey: First Look at Resolved Candidate Disks around Class 0 and I Protostars in the Perseus Molecular Cloud

We present the first dust emission results toward a sample of seven protostellar disk candidates around Class 0 and I sources in the Perseus molecular cloud from the VLA Nascent Disk and Multiplicity (VANDAM) survey with $\sim$0.05″ or 12 AU resolution. To examine the surface brightness profiles of these sources, we fit the Ka-band 8 mm dust-continuum data in the u,v-plane to a simple, parametrized model based on the Shakura-Sunyaev disk model. The candidate disks are well-fit by a model with a disk-shaped profile and have masses consistent with known Class 0 and I disks. The inner-disk surface densities of the VANDAM candidate disks have shallower density profiles compared to disks around more evolved Class II systems. The best-fit model radii of the seven early-result candidate disks are R_c >10 AU; at 8 mm, the radii reflect lower limits on the disk size since dust continuum emission is tied to grain size and large grains radially drift inwards. These relatively large disks, if confirmed kinematically, are inconsistent with theoretical models where the disk size is limited by strong magnetic braking to <10 AU at early times.

This chapter is published in the The Astrophysical Journal Letters as Segura-Cox, D. M., Harris, R. J., Tobin, J. J., et al. 2016, ApJ, 817, L14

3.1 Introduction

Disks around young protostars are intrinsically linked to planet formation, binary formation, and protostellar mass accretion (Williams & Cieza, 2011; Armitage, 2011). In spite of their importance in star formation, when and how disks form–and their properties at early times–are poorly constrained. Hence, whether large and massive disks can form in young protostars (i.e. Class 0/I stages, Andre et al., 2000; Dunham et al., 2014b) is subject to debate (e.g., Jørgensen et al., 2009; Chiang et al., 2008; Maury et al., 2010, respectively). Theoretical studies demonstrate magnetic fields can affect the formation timescales and properties of disks. In particular, strong magnetic fields can remove angular momentum from a collapsing envelope via magnetic braking, reducing forming disks to R <10 AU (e.g., Mellon & Li, 2008; Dapp & Basu, 2010; Machida et al., 2011; Li et al., 2011; Dapp et al., 2012). Complicating the issue, several mechanisms can lessen the effects of magnetic braking, leading to larger disks: misalignment between the rotation axis and magnetic field of the system (e.g., Joos et al., 2012; Li et al., 2013), turbulence (e.g., Seifried et al., 2013; Joos et al., 2013), and initial conditions (e.g., Machida et al., 2014). The protostellar stage represents the stage with the largest mass reservoir available to form disks, therefore understanding the properties of disks at early epochs is crucial to determine the formation mechanism behind these structures.

Protostellar disks, however, are difficult to observe. Class 0 protostars and disks are so enshrouded that $\gtrsim$90% of their millimeter emission comes from the envelope (Looney et al., 2000). The three Class 0 protostars that have been observed with enough resolution and sensitivity to determine their disk properties and detect Keplerian rotation (L1527, VLA 1623, and HH212) have R >30 AU disks, larger than expected from strong magnetic braking models (Ohashi et al., 2014; Tobin et al., 2012; Murillo et al., 2013; Codella et al., 2014). Observational limitations prevent smaller disks from being detected; these Class 0 disks may not represent typical disks at this stage of evolution. Class I protostars are less embedded and have cleared enough of their mass reservoir that more disks have been detected than in

Class 0 systems (e.g., Harsono et al., 2014), though not as many disks have been revealed as in more-evolved Class II sources (e.g., Andrews et al., 2009, 2010). Without detection and study of more disks around the youngest protostellar systems, we cannot characterize early conditions of mass accretion onto the central protostar and planet formation because evolutionary mechanisms can change disk properties by the Class II phase (Williams & Cieza, 2011).

To characterize the properties of the youngest disks and binaries, we are using the Karl G. Jansky Very Large Array (VLA) to conduct the VLA Nascent Disk and Multiplicity (VANDAM) continuum survey at $\lambda \sim 8, 10, 40, 64$ mm toward all identified protostars in the Perseus molecular cloud (Tobin et al., 2015b). The Perseus molecular cloud is relatively close (d $\sim$230 pc; Hirota et al., 2008, 2011) and has a significant number of Class 0 and I protostars (43 and 37 systems, respectively; Tobin et al., 2016b). The early results of the VANDAM survey have already revealed several candidate disk sources in both Class 0 and I sources at 10 AU scales. We consider these to be candidate disks because we lack kinematic data on small scales to determine whether these structures are rotationally supported. Nevertheless, so little is known about this early stage of disk evolution that even continuum-only imaging of young disks provides useful constraints on their properties.

In this Chapter, we present the first results toward some of the protostellar disk candidates around Class 0 and Class I sources from the VANDAM survey. We show the observed structures are consistent with disks by fitting the 8 mm dust-continuum data in the u,v-plane to a simple, parameterized emission model based on the Shakura-Sunyaev disk model. VANDAM survey data provide an unparalleled opportunity to study the youngest disks: the unsurpassed resolution, sample size, and sensitivity for Class 0 and I protostars, permit a detailed examination of typical continuum properties of young disks.

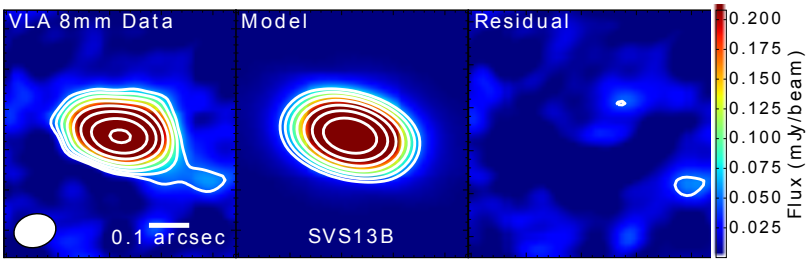

Figure 3.1: VLA A+B array data (left), $q = 1.0$ model from u,v-plane best-fit (center), and residual (right) of SVS13B. Images were produced with robust = 0.25 weighting. Contours start at 3σ (σ $\sim$15μJy) with a factor of $\sqrt{2}$ spacing. The synthesized beam is in the lower left.

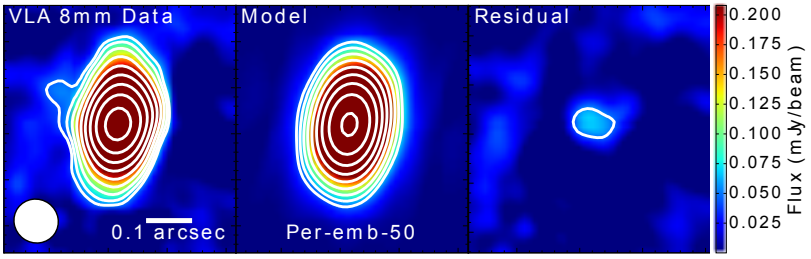

Figure 3.2: Same as Figure 3.1, for Per-emb-50, with $q = 0.25$.

3.2 Observations

The VANDAM survey includes Ka-band lower-resolution ($\sim$0.28″ or 65 AU) B-array data and high-resolution ($\sim$0.05″ or 12 AU) A-array data. We detected 16 protostellar candidate disk sources in the Perseus molecular cloud with the data collected in 2013, 2014, and 2015 (Segura-Cox et al. in prep). Here we focus on seven of the candidate disks (Table 3.1; Figures 3.1 through 3.7, left) which were observed with A-array prior to 2015 and can be well modeled with the prescription described in Section 3.4. The observations were made in three-bit correlator mode, with a bandwidth of 8 GHz divided into 64 sub-bands. Each sub-band has 128 MHz bandwidth, 2 MHz channels, and full polarization products. The two 4 GHz basebands are centered at 36.9 GHz ($\sim$8.1 mm) and 29.0 GHz ($\sim$10.5 mm). Three sources were observed in each 3.5 hour block, and two sources were observed in each 2.75 hour block. Some observations were conducted as 1.5 hour blocks. 3C48 served as the flux calibrator, and 3C84 was the bandpass calibrator. The observations were taken in fast-switching mode

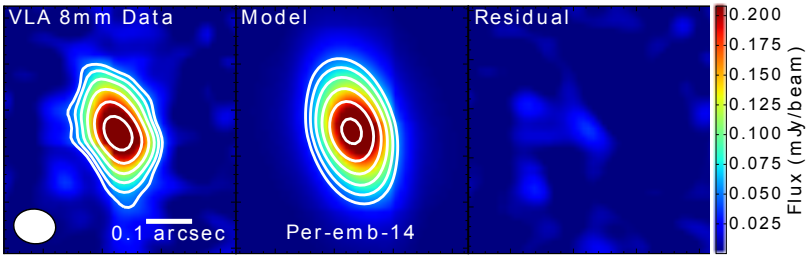

Figure 3.3: Same as Figure 3.1, for Per-emb-14, with $q = 0.25$.

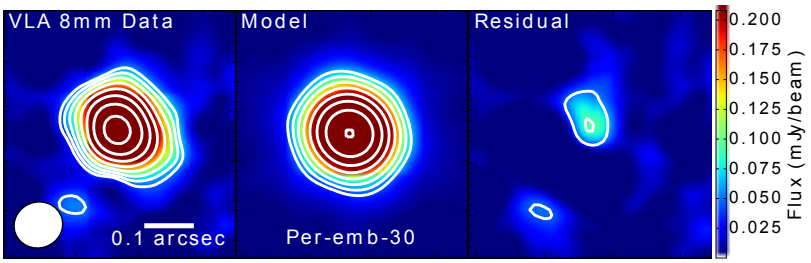

Figure 3.4: Same as Figure 3.1, for Per-emb-30, with $q = 0.25$.

to account for rapid atmospheric phase variations, with a 2.5 minute total cycle time to switch between the target source and the complex gain calibrator, J0336+3218. The total integration time on each source was ∼30 minutes for both A-array and B-array. We reduced the data with CASA 4.1.0 and the VLA pipeline (version 1.2.2). We executed additional flagging beyond pipeline flagging by inspecting the phase, gain and bandpass calibration solutions. VLA Ka-band data sets have an estimated amplitude calibration uncertainty of ∼10%, but only statistical uncertainties are considered in our analysis.

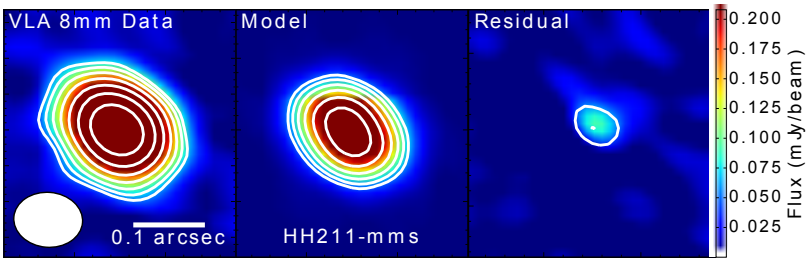

Figure 3.5: Same as Figure 3.1, for HH211-mms, with $q = 0.25$.

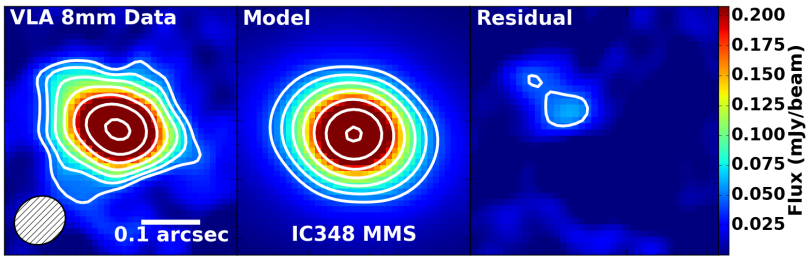

Figure 3.6: Same as Figure 3.1, for IC348 MMS, with $q = 0.25$.

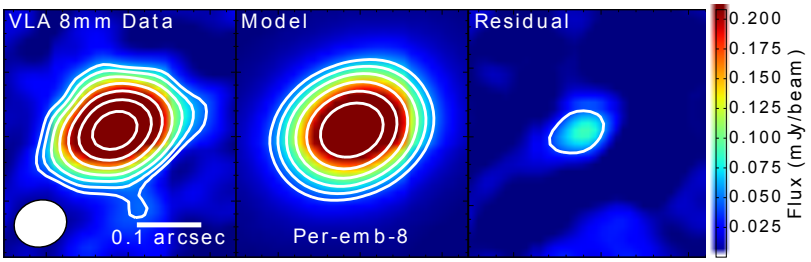

Figure 3.7: Same as Figure 3.1, for Per-emb-8, with $q = 0.25$.

Table 3.1: Observations

Source	α (J2000)	δ (J2000)	A-array Obs. Date	B-array Obs. Date	Combined Beam (mas×mas)	Beam P.A. (°)
SVS13B	03:29:03.078	+31:15:51.740	03 May 2014	22 Oct 2013	105 × 83	-74.8
Per-emb-50	03:29:07.768	+31:21:57.125	01 Jun 2014	26 Oct 2013	97 × 94	54.0
Per-emb-14	03:29:13.548	+31:13:58.153	25 Feb 2014	22 Oct 2013	91 × 75	82.4
Per-emb-30	03:33:27.303	+31:07:10.161	16 May 2014	23 Oct 2013	99 × 92	-71.5
HH211-mms	03:43:56.805	+32:00:50.202	24 Feb 2014	21 Oct 2013	96 × 77	85.4
IC348 MMS	03:43:57.064	+32:03:04.789	23 Mar 2014	22 Oct 2013	89 × 80	-57.7
Per-emb-8	03:44:43.982	+32:01:35.209	22 Feb 2014	01 Oct 2013	82 × 72	-71.6

Observation dates mark the start of the observations. Combined beam sizes reflect robust = 0.25 weighting.

3.3 Estimated Masses

Two key quantities that describe disks are their masses and radii. While accurately determining disk radii requires modeling, masses are estimated from flux measurements (Table 3.2). By assuming optically thin emission, we estimate disk masses from the 8 mm dust continuum flux with the relation (Hildebrand, 1983):

$$M = \frac{d^2 F_\nu}{B(T_d)\kappa_\nu}, \tag{3.1}$$

where F_ν, d, κ_ν, and $B_\nu(T_d)$, are respectively the total observed flux, distance, grain opacity, and blackbody intensity at dust temperature T_d. We estimate κ_ν at 8.1 mm by normalizing to Ossenkopf & Henning (1994) at 1.3 mm using a dust to gas ratio of 1/100: $\kappa_\nu = (1/100)(\nu/231\text{GHz}))^\beta$ cm^2 g^{-1}. $\beta = 1$ is typically assumed for protostellar disks (Andrews et al., 2009), giving $\kappa_\nu = 0.00146$ cm^2 g^{-1}. Mass estimates are inherently ambiguous within an order of magnitude due to uncertainties in the dust-to-gas ratio, T_d, and β; rather than compute a single mass estimate, we calculate lower and upper mass estimates for each source by varying T_d. Lower masses were estimated by assuming $T_d = 40$ K, and we determined upper estimates using $T_d = 20$ K. These candidate disks range in flux from 867.5 μJy to 1664.9 μJy, providing estimated masses of 0.09–0.36 M$_\odot$ (Table 3.2).

Table 3.2: Source Data

Source	Class	Deconvolved Size (mas×mas)	Disk P.A. (°)	Disk Inclination (°)	F_{8mm} (μJy)	M_d ($M_\odot$)	$F_{>1700k\lambda}$ (μJy)
SVS13B	0	163×80	71.4±2.5	61	1352.7±11.6	0.14 - 0.29	82.0
Per-emb-50	I	137×53	170.0±0.3	67	1664.9±12.5	0.18 - 0.36	133.2
Per-emb-14	0	174×76	12.7±0.9	64	882.1±13.0	0.09 - 0.19	68.8
Per-emb-30	0	87×74	40.0±23.0	31	957.0±9.4	0.10 - 0.21	130.9
HH211-mms	0	93×59	34.8±9.6	51	867.5±8.1	0.09 - 0.19	42.9
IC348 MMS	0	145×105	70.8±2.2	44	1126.5±10.3	0.12 - 0.24	0.0
Per-emb-8	0	111×84	116.1±2.8	41	1120.7±10.3	0.12 - 0.24	126.5

Sizes and angles are measured from image-plane 2D Gaussian fits. Angles are measured counterclockwise from north. Uncertainties on the deconvolved sizes are ∼5.0 mas. Uncertainties on inclinations are ∼10°.

3.4 Modeling

We modeled the 8 mm A+B array continuum data by fitting a symmetric disk intensity profile to the continuum emission of each source. In this modeling, we deprojected the 8 mm visibility data to a fixed position angle (P.A.) and fixed inclination as determined through image-plane 2D Gaussian fitting of the disk candidates and assumed the disks are circularly symmetric (Table 3.2). We azimuthally averaged the visibility data in the u,v-plane and binned the data in linearly spaced bins of width 50 kλ from 0 to 1500 kλ, switching to 30 log-spaced bins from 1500 to 4000 kλ where the data becomes noisier in order to boost the signal-to-noise level at large u,v-distances. We accounted for a lower-limit free-free point source component emanating from shocks in the protostellar jets (Anglada et al., 1998). Because point sources in the image domain have constant flux density at all u,v-distances, we account for the free-free component by calculating the average real component of the binned data with u,v-distance >1700 kλ and include the average as a flat, linear component of the model (Table 3.2); the profiles become flat at values >1700 kλ in all seven sources (e.g., Figure 3.8).

We fitted the real components of the deprojected, averaged, and binned profile to a simple disk model using a C-based implementation of `emcee`, an affine-invariant Markov chain Monte Carlo ensemble sampler (Goodman & Weare, 2010; Foreman-Mackey et al., 2013). The imaginary components were assumed to be zero in the model since the disk is positioned at the phase center and assumed to be symmetric. The model mimics a Shakura-Sunyaev disk (Shakura & Sunyaev, 1973) with a power law temperature profile; the resultant model disk surface brightness profile is

$$I(r) \propto \left(\frac{r}{R_c}\right)^{-(\gamma+q)} \exp\left\{-\left(\frac{r}{R_c}\right)^{(2-\gamma)}\right\}, \tag{3.2}$$

where $I(r)$ is the radial surface brightness distribution, q is the temperature exponent, γ is

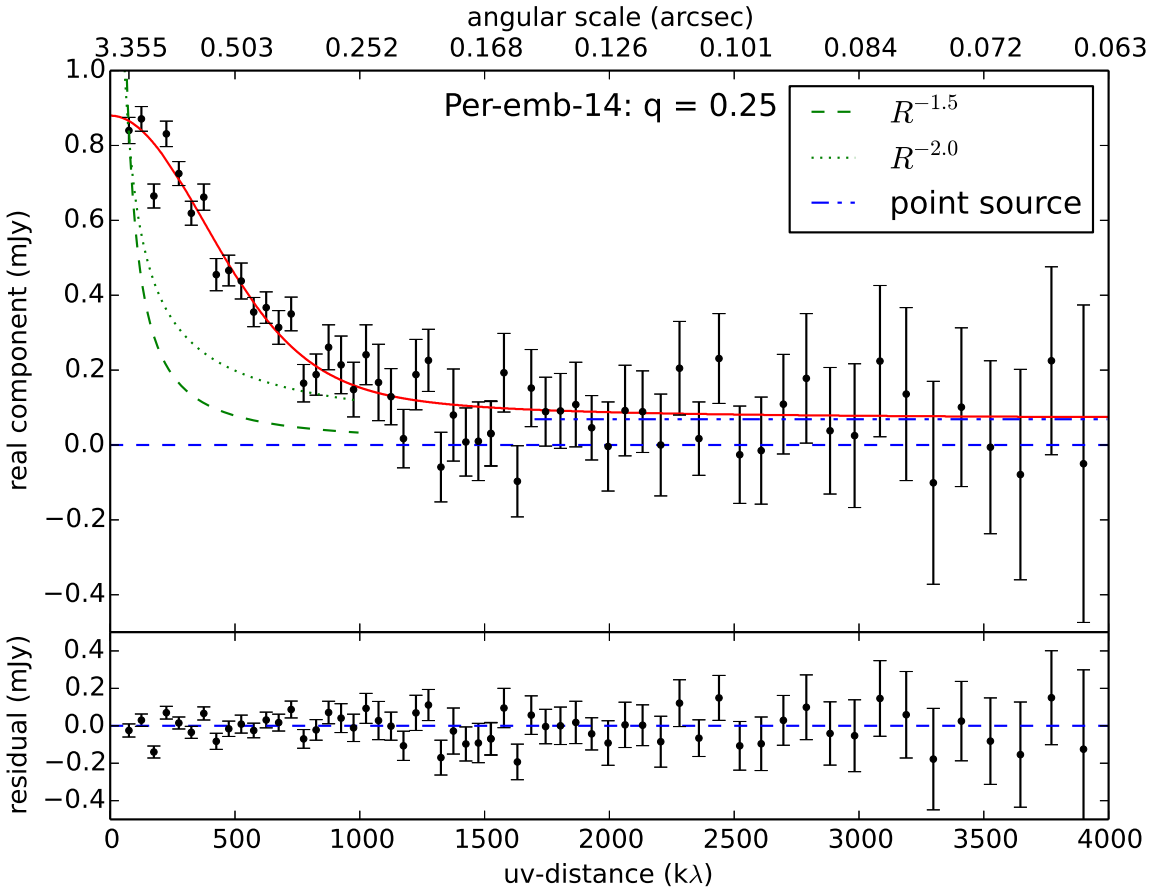

Figure 3.8: Sample real vs u,v-distance plot of 8 mm data. Top: real component of data. The blue dashed line indicates real component of zero. The red solid line is the best-fit model. The green lines represent envelope profiles scaled to the zero-baseline flux. Bottom: residual of real component minus model.

the power-law of the inner-disk surface density, and r is radius. R_c is a characteristic radius at which there is significant optical depth and disk material, making it a proxy for outer disk radius. This flux density profile is appropriate here because the 8 mm data is expected to be in the Rayleigh-Jeans tail of the dust emission. Flux is given by $F = \int_0^\infty I(r)\ 2\pi r\ dr$. Flux, disk radius, and gradient were free parameters in the fitting. We fitted a model disk for values of $q = [0.25, 0.50, 0.75, 1.00]$ to the observations in order to avoid over-fitting the data while exploring reasonable physical values of q.

3.5 Results

Once model fitting was completed on the candidate disks, we generated disk model visibilities corresponding to the best-fit parameters. The best-fit model and residuals for each source were Fourier transformed, sampled at the same u,v-points as the data, and imaged using the same weighting as the data (Figures 3.1 through 3.7, center). We subtracted the model visibility from the data to produce a residual visibility set. Synthetic maps were created of the best-fit model disks. Residual maps were made by imaging the Fourier transformed visibilities after subtracting the model from the data in the u,v-plane (Figures 3.1 through 3.7, right). An example of the binned observational data, model fits, and residuals is also shown in Figure 3.8 .

Fit results are shown in Table 3.3. The $\chi^2_{\rm reduced}$ values near one and the nearly empty residual maps indicate the seven candidate disk sources were well-modeled by our simple-shaped disk profile and are hence likely to be Class 0 and young Class I disks rather than inner envelope structure (Chiang et al., 2008). All candidate disks have modeled R_c >10 AU, and except for HH211-mms the disks are large compared to the $R = 10$ AU upper limit predicted by magnetic braking models of Dapp & Basu (2010) at the Class 0 stage.

The model includes a disk and point-source component but does not take into account envelope emission. The observations filter out the majority of the contaminating envelope emission, demonstrated by the visibility profiles corresponding to $R^{-1.5}$ and $R^{-2.0}$ envelope surface density profiles plotted in Figure 3.8. These envelope density profiles represent, respectively, free-fall collapse and the singular isothermal sphere (Shu, 1977). The best-fit models were determined from the maximum likelihood, i.e. the lowest χ^2 value, of all models fit to the data. Values of q near 0.5 are predicted by theory (e.g., Chiang & Goldreich, 1997) for Class II protostars, which are more evolved than the protostars in our sample. Lower values of q result in lower values of $\chi^2_{\rm reduced}$ for six candidate disks. Values of $q <$ 0.5 for Class 0 and younger Class I sources are favored since the envelope mass reservoir

is still large, and radiation is reprocessed from the protostar and directed back onto the disk, increasing the brightness of the outer disk relative to the inner regions of the disk and flattening the brightness distribution (D'Alessio, 1996). Compared to the other modeled protostars, $\chi^2_{\rm reduced}$ is notably higher for SVS13B which may be a more complicated source and not well described by the model.

Table 3.3: 8mm Best-fit Disk Modeling Results

Source	q	γ	R_c (AU)	$\chi^2_{\rm reduced}$
SVS13B	0.25	$0.21^{+0.23}_{-0.20}$	$24.28^{+2.1}_{-1.7}$	2.194
	0.50	$0.42^{+0.25}_{-0.21}$	$25.50^{+1.9}_{-1.5}$	2.185
	0.75	$0.63^{+0.24}_{-0.22}$	$26.46^{+1.6}_{-1.4}$	2.175
	1.00	$0.85^{+0.26}_{-0.23}$	$27.28^{+1.4}_{-1.2}$	2.164
Per-emb-50	0.25	$0.08^{+0.02}_{-0.16}$	$21.9^{+0.8}_{-0.9}$	1.556
	0.50	$0.26^{+0.15}_{-0.17}$	$23.3^{+1.1}_{-1.0}$	1.558
	0.75	$0.44^{+0.16}_{-0.17}$	$24.6^{+1.4}_{-1.1}$	1.560
	1.00	$0.64^{+0.16}_{-0.18}$	$25.7^{+1.4}_{-1.3}$	1.563
Per-emb-14	0.25	$-0.11^{+0.16}_{-0.00}$	$28.5^{+2.3}_{-2.1}$	1.110
	0.50	$0.09^{+0.08}_{-0.21}$	$30.6^{+2.8}_{-2.3}$	1.114
	0.75	$0.27^{+0.17}_{-0.24}$	$32.5^{+2.2}_{-2.8}$	1.119
	1.00	$0.48^{+0.19}_{-0.23}$	$33.9^{+3.6}_{-3.1}$	1.123
Per-emb-30	0.25	$0.02^{+0.18}_{-0.31}$	$14.0^{+1.0}_{-0.9}$	1.100

Continued on Next Page...

Values of q are fixed. Values of γ and R_c are determined from best-fit models. Uncertainties reflect 90% confidence intervals.

Table 3.3 – Continued

Source	q	γ	R_c (AU)	$\chi^2_{\rm reduced}$
	0.50	$0.20^{+0.04}_{-0.32}$	$14.9^{+1.9}_{-1.1}$	1.102
	0.75	$0.39^{+0.30}_{-0.34}$	$15.8^{+1.9}_{-1.3}$	1.104
	1.00	$0.59^{+0.14}_{-0.33}$	$16.5^{+31.3}_{-1.6}$	1.107
HH211-mms	0.25	$0.48^{+0.40}_{-0.78}$	$10.5^{+0.8}_{-0.8}$	1.009
	0.50	$0.65^{+0.43}_{-0.82}$	$11.0^{+1.0}_{-0.9}$	1.009
	0.75	$0.81^{+0.42}_{-0.79}$	$11.5^{+1.2}_{-1.2}$	1.009
	1.00	$1.01^{+0.44}_{-0.81}$	$11.9^{+1.4}_{-1.3}$	1.009
IC348 MMS	0.25	$-0.58^{+0.11}_{-0.11}$	$25.7^{+2.8}_{-2.2}$	1.085
	0.50	$-0.39^{+0.19}_{-0.11}$	$29.0^{+3.2}_{-2.6}$	1.096
	0.75	$-0.19^{+0.11}_{-0.27}$	$31.6^{+4.1}_{-2.9}$	1.107
	1.00	$0.02^{+0.07}_{-0.11}$	$33.7^{+4.3}_{-3.1}$	1.118
Per-emb-8	0.25	$0.01^{+0.16}_{-0.19}$	$19.0^{+1.2}_{-1.1}$	1.099
	0.50	$0.20^{+0.17}_{-0.20}$	$20.2^{+1.4}_{-1.3}$	1.107
	0.75	$0.40^{+0.17}_{-0.21}$	$21.2^{+1.6}_{-1.4}$	1.114
	1.00	$0.61^{+0.17}_{-0.20}$	$22.1^{+1.8}_{-1.6}$	1.122

Values of q are fixed. Values of γ and R_c are determined from best-fit models.

Uncertainties reflect 90% confidence intervals.

3.6 Discussion

The estimated masses of the candidate disks are consistent with known disks around Class 0 and I protostars. The seven VANDAM candidate Class 0 and I disks range in estimated masses of 0.09–0.36 $M_\odot$. Scaling to our value of κ_ν, the Class 0 protostar L1527's disk is 0.013 $M_\odot$ (Tobin et al., 2013b) with $T_d = 30$ K. A recent interferometric study of Class I disks in Taurus (Harsono et al., 2014) revealed the disks around TMC1A, TMC1, TMR1 and L1536 to have masses of 0.4–3.3$\times10^{-2}$ $M_\odot$ with $T_d = 30$ K and Ossenkopf & Henning (1994) opacities. All mass estimates have uncertainties of a factor of $\sim$10 due to the unknown gas-to-dust ratio, T_d, β, and varying choices of κ_ν.

Values of γ, the power-law of the inner-disk surface density, for the VANDAM sources can be compared to values found for older Class II sources. The best-fit models for our seven sources yield $-0.58 < \gamma < 0.45$. Negative values of γ indicate increasing surface density with radius, inconsistent with disks, yet for all sources at least one value of q exists which produces a positive best-fit γ (Table 3.3). Andrews et al. (2010) determined γ at 880 μm for disks around Class II objects using a two-dimensional parametric model with a prescription of the surface density profile similar to the radial surface brightness distribution applied in this Chapter. The Class II sources have values of $0.4 < \gamma < 1.1$, larger than VANDAM results. The modeled, surface density profiles of the Class 0 and I systems taper off less quickly with radius compared to the Class II systems inside the characteristic radius R_c.

The best-fit model radii of the candidate Class 0 disks are between $\sim$15-30 AU, except HH211-mms with R_c $\sim$10 AU. These are smaller than the Keplerian disks found in L1527 and VLA 1623 at 1.3 mm (Ohashi et al., 2014; Murillo et al., 2013, R $\sim$54 AU and R $\sim$189 AU respectively) but consistent with the size of HH212 (Codella et al., 2014, R > 30 AU). The modeled radii (Table 3.3) are a factor of 1 to 1.5 times larger than the deconvolved sizes (Table 3.2). The radii of the new candidate disks may represent lower limits on disk sizes because continuum emission from dust is biased by dust grain size. Radial drift (Birnstiel

et al., 2010; Weidenschilling, 1977) sends large grains inward in the disk, and so the long wavelength observations preferentially trace inner disk emission (Pérez et al., 2012). We expect the 8 mm dust-modeled radii to be less than the gas disk radius, and so the 8 mm radii are lower-limits on disk size; multi-wavelength observations that include gas tracers are required to further constrain disk radii. Per-emb-14 was resolved at 1.3 mm by Tobin et al. (2015a) with $R \sim$100 AU; thus the disk is indeed likely larger than the 8 mm radius quoted here. In all cases, the previously known disks and new candidate Class 0 disks are larger than the expected upper limit of 10 AU from strong magnetic braking models (e.g., Dapp & Basu, 2010).

The seven VANDAM candidate disks are well-fit by a disk-shaped model and have disk masses, values of γ, and radii consistent with known disks. These candidate disks can be compared to the well-studied Class 0 systems with disks: L1527 (Tobin et al., 2012) and VLA 1623 (Murillo & Lai, 2013). L1527 and VLA 1623 have large Keplerian disks ($R \sim$50 AU, Ohashi et al., 2014; Murillo et al., 2013) as well as misaligned magnetic fields and rotation axes (Hull et al., 2014), suggesting that misaligned fields and large disks may be linked (Segura-Cox et al., 2015). The discrepancy between theoretical and observed disk sizes could be due to misalignment between the magnetic field and rotation axis, which changes the strength of magnetic braking, allowing disks to grow at early times (Hennebelle & Ciardi, 2009; Joos et al., 2012; Li et al., 2013; Krumholz et al., 2013). Similarly, aligned orientations would strengthen magnetic braking and limit disk size, as seen in the Class 0 source B335 with a disk of $R <$5 AU (Yen et al., 2015; Hull et al., 2014). The large Keplerian Class 0 disks and new candidate disks indicate significant magnetic braking either has already occurred, has not happened, or the magnetic field is weak enough for disks with $R >$10 AU around these Class 0 protostars to form, though other configurations are possible.

It is illustrative to compare the presence of VANDAM candidate disks to the magnetic field morphology of the systems. The TADPOL survey examines protostellar dust polarization and hence plane-of-sky magnetic field orientation. (Hull et al., 2014). For sources

with detected magnetic fields, we are able to determine which systems have misaligned orientations between the outflow (a proxy for rotation axis) and the average magnetic field orientation. The magnetic field morphologies of two of the seven VANDAM sources in this Chapter (HH211-mms and SVS13B) were also examined as a part of the TADPOL survey. A qualitative comparison between the VANDAM data and the TADPOL magnetic field orientation reveals that HH211-mms and SVS13B morphologies agree with the tentative link between R >10 AU disks and misaligned orientations (Segura-Cox et al., 2015). HH211-mms has a clearly misaligned orientation (Hull et al., 2014), agreeing with theoretical predictions that disks with R >10 AU disks form at early times in systems with non-parallel orientations. SVS13B has a more complicated magnetic field morphology with an average aligned orientation (Hull et al., 2014) with the outflow (Bachiller et al., 1998), however the TADPOL data has lower resolution than our data ($\sim 3''$, or 700 AU), and the innermost regions of the magnetic field has misaligned orientation near the candidate disk. The small-scale, misaligned orientation in SVS13B could be caused by magnetic fields being wrapped up with the rotating disk, and the aligned magnetic field lines further from the disk are less influenced by the disk wrapping.

3.7 Conclusions

The first results of the VANDAM survey revealed new candidate Class 0 and I disks in continuum emission in the Perseus molecular cloud and is the most sensitive, most complete, and highest resolution survey of young protostellar disks to-date. For seven of the VANDAM systems, we fit the deprojected, averaged, and binned data in the u,v-plane to a disk-shaped profile, accounting for a free-free point source potentially contaminating the dust emission, to affirm the disk candidacy of the sources and to begin to model disk properties. To confirm that these disks are true, rotationally-supported disks, kinematic follow-up observations are required. The seven VANDAM candidate disks are well-fit by a model with a disk-shaped

profile and have masses comparable to known disks. The inner-disk surface densities of the Class 0 and I candidate disks taper off less quickly with radius than their Class II counterparts.

The best-fit model radii of the new candidate disks are R_c >15 AU, except HH211-mms with R_c ∼10 AU. Since magnetic braking is expected to suppress Class 0 disks to R <10 AU, this suggests that magnetic braking has already ended or is inconsequential in some Class 0 sources. At 8 mm, the modeled radii are lower limits on the disk size since dust continuum emission is tied to grain size and large grains radially drift inwards in the disk; the actual sizes of the disks may be larger. Multi-wavelength observations are needed to put added constraints on disk radii. Furthermore, theory predicts larger disk growth in systems with misaligned outflow axes and magnetic field orientations, and the early VANDAM candidate disk results combined with polarization data for two of the sources indicate that indeed R >10 AU disks have formed in systems with misaligned orientations.

This research made use of APLpy, an open-source plotting package for Python hosted at http://aplpy.github.com.

DMSC is currently supported by NRAO Student Observing Support grant SBC NRAO 2015-06997. JJT is currently supported by grant 639.041.439 from the Netherlands Organisation for Scientific Research (NWO). ZYL is supported by NASA NNX14AB38G and NSF AST-1313083.

The National Radio Astronomy Observatory is a facility of the National Science Foundation operated under cooperative agreement by Associated Universities, Inc.

Chapter 4

The VLA Nascent Disk and Multiplicity Survey: Full Results from Modeling Candidate Disks around Class 0 and I Protostars in Perseus

In this Chapter, we present the full results from the disk portion of the VANDAM survey of all Class 0 and I protostars in the Perseus molecular cloud. We have 19 new protostellar disk candidates around Class 0 and I sources, which are well described by a simple, parametrized disk model fit to the deprojected, azimuthally averaged, and radially binned 8 mm dust-continuum observations. 35% of Class 0 protostars and just 11% of Class I protostars have candidate disks larger than the 12 AU resolution of the VLA data. 76% of Class 0 and I protostars do not have signs of disks within our 12 AU resolution limit, indicating that at 8 mm most disks in the Class 0 and I phases are small (<10 AU). Modeled disk parameters indicate that more evolved Class II disks are generally more centrally concentrated than our Class 0 and I disks. Modeled 8 mm radii are similar to the radii of known Class 0 disks found to have Keplerian rotation in ∼mm wavelengths. Since our 8 mm data trace a population of larger dust grains which radially drift towards the protostar and are lower limits on true disk size, large disks at early times do not seem to be particularly rare. By combining our candidate disk properties with previous polarization observations, we find a qualitative indication that misalignment between inferred magnetic fields on envelope scales and outflows may be a signpost of disks on smaller scales in Class 0 sources with geometrically-thick disks.

4.1 Introduction

Disks of gas and dust around young protostars are fundamental to protostellar mass accretion and act as the mass reservoir from which stars and planetesimals form (Armitage, 2011; Williams & Cieza, 2011). Circumstellar disks form around even the youngest Class 0 protostars which are embedded in their dense natal dust and gas envelope. Class I protostars are less embedded, having cleared a portion of their envelopes (McKee & Ostriker, 2007). Until recently, disks around Class 0 and Class I protostars have remained elusive because ∼millimeter wavelengths are required to penetrate through the dense envelope (Looney et al., 2000), and sub-arcsecond resolution is required to spatially resolve the disk. Keplerian rotation is a tell-tale sign of true, rotationally supported disks which exist for long enough timescales to form long-lived disk structures and eventually planets; flattened structures without rotation quickly collapse inward (e.g., Ohashi et al., 2014). So few young Keplerian disks are known that questions concerning disk frequency, disk radii, dust populations, disk evolution, and presence of planetesimals in the youngest protostellar disks are only beginning to be addressed.

Keplerian rotation has been detected in disks around only 4 total Class 0 protostars with R >30 AU (Ohashi et al., 2014; Tobin et al., 2012; Murillo et al., 2013; Codella et al., 2014; Yen et al., 2017); however they are bright disks and may not represent typical disks at this stage of evolution. Class I protostars have longer lifetimes and have cleared enough of their mass reservoir that more Class I disks have been detected (∼10 total; Harsono et al., 2014) than in Class 0 systems (3 total) though not nearly as many as the ∼100 total in more-evolved Class II sources (e.g., Andrews et al., 2009, 2010). By the Class II stage the envelope has mostly dispersed, clearly revealing the circumstellar disk. Recent observations of a disk around a Class II protostar have revealed the earliest known evidence of planet formation (ALMA Partnership et al., 2015). The Class 0 and I protostellar stages have the largest mass reservoirs available to form disks and planetesimals; therefore understanding

the properties of disks at the earliest possible epochs is crucial to determine the formation mechanism behind circumstellar disks and the initial pathway to planet formation.

The morphology and strength of the magnetic fields in protostellar systems also play an important role in star and disk formation (e.g., Crutcher, 2012). Magnetic field effects on the small size scale of circumstellar disks ($\sim$0.5″ or $\sim$100 AU) of young stellar objects have started to be theoretically and observationally quantified in individual systems (Mellon & Li, 2008; Hennebelle & Fromang, 2008; Stephens et al., 2014; Segura-Cox et al., 2015; Cox et al., 2015). Magnetic field morphology can be inferred from dust emission; spinning dust grains align their long axes perpendicular to the magnetic field, polarizing the dust emission (e.g., Lazarian, 2007). When a strong magnetic field and rotation axis of the circumstellar disk are aligned, magnetic braking can have a significant effect on disk formation by transporting away angular momentum, reducing forming disks to R <10 AU (e.g., Mellon & Li, 2008; Dapp & Basu, 2010; Machida et al., 2011; Li et al., 2011; Dapp et al., 2012). In this scenario, disks only reach R $\sim$100 AU at the end of the Class I when the envelope is less massive and magnetic braking becomes inefficient (e.g., Dapp et al., 2012; Mellon & Li, 2009; Machida et al., 2011). Conversely, recent works have highlighted the critical importance of the magnetic field direction relative to the rotation axis: when the field and rotation axis are misaligned, magnetic braking becomes less efficient, and $\sim$100 AU disks can form (Joos et al., 2012; Li et al., 2013; Krumholz et al., 2013; Segura-Cox et al., 2015, 2016). Because so few young embedded disks are currently known via observations, expanding the number of known Class 0 and I disks is critical to determining the role of magnetic braking in disk growth at early times.

To characterize the properties of the youngest disks, we used the Karl G. Jansky Very Large Array (VLA) to make observations with the VLA Nascent Disk and Multiplicity (VANDAM) continuum survey at $\lambda \sim 8, 10, 40, 64$ mm toward all identified protostars in the Perseus molecular cloud (Tobin et al., 2015b). The continuum observations trace dust emission and free-free emission from jets near the central protostar. The VANDAM observations

form an unbiased survey of young protostellar disks down to ∼10 AU size scales, giving us the opportunity potentially double the number known disks in Class 0 and I protostars from ∼15 total to over 30. We use the term "candidate disks" because we do not have kinematic data on small scales to determine whether these structures are rotationally supported. Our sample contains all currently known Class 0 and I protostars in the Perseus, with 37 Class 0 protostars, 8 Class 0/I protostars, and 37 Class I protostars. The 21 resolved sources in the VANDAM survey we examine in this Chapter (Table 4.1) are the most complete sample of embedded sources in Perseus to-date (see Tobin et al., 2016b, for discussion of target selection). Per-emb-XX designations originate from Enoch et al. (2009). We define resolved or extended sources as having spatial extents at least 1.1× the size of the beam, meaning we include marginally resolved sources in this study. We fit disk models to all protostars with relatively axisymmetric resolved emission (17 of 21 sources, see Table 4.2 and Section 4.4); however, only sources with either axisymmetric resolved emission and a modeled disk-like profile or non-symmetric emission and other indirect evidence of a disk are considered candidate disks (see Section 4.6).

In this Chapter, we present the full results toward the protostellar disk candidates around the Class 0 and Class I sources from the VANDAM survey. This Chapter expands on the work done in Segura-Cox et al. (2016) (Chapter 3), which reported a subset of the candidate disks studied here. We show the observed structures are consistent with disks by fitting the 8 mm dust-continuum data in the u,v-plane to a simple, parameterized emission model based on the Shakura-Sunyaev disk model. VANDAM survey data provide an unparalleled opportunity to study the youngest disks: the unsurpassed resolution, sample size, and sensitivity for Class 0 and I protostars, permit a detailed examination of typical continuum properties of young disks, with the potential to double the number of known Class 0 and I disks.

4.2 Observations

The VANDAM survey includes Ka-band lower-resolution ($\sim$0.28″ or 65 AU) B-array data and high-resolution ($\sim$0.05″ or 12 AU) A-array data. We detected 21 protostars with extended emission larger than the size of the beam in the Perseus molecular cloud with the data collected in 2013, 2014, and 2015 (Table 4.1). The observations were made in three-bit correlator mode, with a bandwidth of 8 GHz divided into 64 sub-bands. Each sub-band has 128 MHz bandwidth, 2 MHz channels, and full polarization products. The two 4 GHz basebands are centered at 36.9 GHz ($\sim$8.1 mm) and 29.0 GHz ($\sim$10.5 mm). Three sources were observed in each 3.5 hour block, and two sources were observed in each 2.75 hour block. Some observations were conducted as 1.5 hour blocks. 3C48 served as the flux calibrator, and 3C84 was the bandpass calibrator. The observations were taken in fast-switching mode to account for rapid atmospheric phase variations, with a 2.5 minute total cycle time to switch between the target source and the complex gain calibrator, J0336+3218. The total integration time on each source was $\sim$30 minutes for both A-array and B-array. We reduced the data with CASA 4.1.0 and the VLA pipeline (version 1.2.2). We executed additional flagging beyond pipeline flagging by inspecting the phase, gain and bandpass calibration solutions. VLA Ka-band data sets have an estimated amplitude calibration uncertainty of $\sim$10%, but only statistical uncertainties are considered in our analysis.

Table 4.1: Observed Target Positions and Beam Sizes

Source	α (J2000)	δ (J2000)	Combined Beam (mas×mas)	Beam P.A. (°)
SVS13B	03:29:03.078	+31:15:51.740	105 × 83	-74.8
Per-emb-50	03:29:07.768	+31:21:57.125	97 × 94	54.0
Per-emb-14	03:29:13.548	+31:13:58.153	91 × 75	82.4
Per-emb-30	03:33:27.303	+31:07:10.161	99 × 92	-71.5
Per-emb1/HH211-mms	03:43:56.805	+32:00:50.202	96 × 77	85.4
Per-emb-11/IC348 MMS	03:43:57.064	+32:03:04.789	89 × 80	-57.7
Per-emb-8	03:44:43.982	+32:01:35.209	82× 72	-71.6
Per-emb-13/NGC 1333 IRAS4B	03:29:12.016	+31:13:08.031	111×92	-85.3
Per-emb-25	03:26:37.511	+30:15:27.813	70×50	-88.3
Per-emb-35A/NGC 1333 IRAS1 A	03:28:37.090	+31:13:30.788	83×74	99.9
Per-emb-62	03:44:12.977	+32:01:35.419	61×52	-69.7
Per-emb-63	03:28:43.271	+31:17:32.931	61×52	-69.7
SVS13C	03:29:01.970	+31:15:38.053	83×74	-79.2
Per-emb-12/NGC 1333 IRAS4A	03:29:10.537	+31:13:30.933	74×53	78.2
Per-emb-2/IRAS 03292+3039	03:32:17.928	+30:49:47.825	107×87	117.1
Per-emb-5/IRAS 03282+3035	03:31:20.939	+30:45:30.273	93×89	-85.4
Per-emb-18	03:29:11.258	+31:18:31.073	106×94	84.2
Per-emb-33A/L1448 IRS3B	03:25:36.379	+30:45:14.728	102×89	-63.2
Per-emb-27/NGC 1333 IRAS2A	03:28:55.569	+31:14:37.025	91×82	-75.5
Per-emb-35B/NGC 1333 IRAS1 B	03:28:37.090	+31:13:30.788	83×74	99.9
Per-emb-53/ B5-IRS1	03:47:41.591	+32:51:43.672	73×64	-76.5

Combined beam sizes reflect robust = 0.25 weighting of A+B array data. Position angle is measured counterclockwise from north.

Table 4.2: Source Data

Source	Class	Deconvolved Size (mas×mas)	Disk P.A. (°)	Disk Inc. (°)	F_{8mm} (μJy)	M_d ($M_\odot$)	$F_{>1700k\lambda}$ (μJy)
SVS13B	0	163×80	71.4±2.5	61	1352.7±11.6	0.14 - 0.29	82.0
Per-emb-50	I	137×53	170.0±0.3	67	1664.9±12.5	0.18 - 0.36	133.2
Per-emb-14	0	174×76	12.7±0.9	64	882.1±13.0	0.09 - 0.19	68.8
Per-emb-30	0	87×74	40.0±23.0	31	957.0±9.4	0.10 - 0.21	130.9
HH211-mms	0	93×59	34.8±9.6	51	867.5±8.1	0.09 - 0.19	42.9
IC348 MMS	0	145×105	70.8±2.2	44	1126.5±10.3	0.12 - 0.24	0.0
Per-emb-8	0	111×84	116.1±2.8	41	1120.7±10.3	0.12 - 0.24	126.5
NGC 1333 IRAS4B	0	344×224	90.9±6.6	49	1537.2±14.0	0.16 - 0.33	0.0
Per-emb-25	0/I	91×55	11.1±16.0	52	613.6±27.6	0.06 - 0.13	95.0
NGC 1333 IRAS1 A	I	77×44	34±1.8	55	586.2±12.4	0.06 - 0.13	0.0
Per-emb-62	I	106×65	107.7±2.8	52	730.9±12.6	0.08 - 0.16	121.1
Per-emb-63	I	78×52	109.7±4.1	48	270.6±10.9	0.03 - 0.06	115.2
SVS13C	0	275×70	95±1.3	75	212.8±11.5	0.02 - 0.05	27.4
NGC 1333 IRAS4A	0	250×205	95.7±5.2	35	14836.1±43.2	1.57 - 3.2	81.0
IRAS 03292+3039	0	...	...	...	3289.3±15.4	0.35 - 0.71	...
IRAS 03282+3035	0	...	...	...	1481.2±12.0	0.16 - 0.32	...
Per-emb-18	0	...	...	...	636.5±11.8	0.07 - 0.14	...
L1448 IRS3B	0	...	...	...	95.6±9.5	0.01 - 0.02	...
NGC 1333 IRAS2A	0/I	65×45	110.9±12.3	46	1935.1±8.9	0.20 - 0.42	494.8
NGC 1333 IRAS1 B	I	67×52	32.1±9.6	39	296.0±14.3	0.03 - 0.06	72.3
B5-IRS1	I	120×83	118±6.2	46	255.8±11.1	0.03 - 0.06	116.9

Sizes and angles are measured from image-plane 2D Gaussian fits. Angles are measured counterclockwise from north. Uncertainties on the deconvolved sizes are ∼5.0 mas. Uncertainties on inclinations are ∼10°. IRAS4A and IRAS4B measurements were made with baselines < 350 kλ excluded to better filter out envelope emission.

4.3 Estimated Masses for All Extended Sources in the VANDAM Survey

Protostellar disks are typically quantified by their radii and masses. We must model the continuum emission to determine the radii accurately (Section 4.4), yet we can straightforwardly estimate masses from flux measurements, assuming no free-free contribution from the jets near the central protostar. By assuming optically thin emission, we estimate disk masses from the 8 mm dust continuum flux with the relation (Hildebrand, 1983):

$$M = \frac{d^2 F_\nu}{B(T_d)\kappa_\nu}, \tag{4.1}$$

where F_ν, d, κ_ν, and $B_\nu(T_d)$, are respectively the total observed flux, distance, grain opacity, and blackbody intensity at dust temperature T_d. We estimate κ_ν at 8.1 mm by normalizing to Ossenkopf & Henning (1994) at 1.3 mm using a dust to gas ratio of 1/100: $\kappa_\nu = (1/100)(\nu/231\text{GHz}))^\beta$ cm^2 g^{-1}. $\beta = 1$ is typically assumed for protostellar disks (Andrews et al., 2009), giving $\kappa_\nu = 0.00146$ cm^2 g^{-1}. Mass estimates are inherently ambiguous within an order of magnitude due to uncertainties in the dust-to-gas ratio, T_d, and β; rather than compute a single mass estimate, we calculate lower and upper mass estimates for each source by varying T_d. Lower bound masses were estimated by assuming $T_d = 40$ K, and we determined upper estimates using $T_d = 20$ K.

The extended sources range in flux from 95.6 μJy to 14836.1 μJy, providing estimated masses of 0.01–3.2 M$_\odot$ (Table 4.2). The mass of Per-emb-33/L1448 IRS3B is likely grossly underestimated because it is a triple system embedded in a larger disk (Tobin et al., 2016a) which is marginally detected at 8 mm.

4.4 Modeling the u,v-data

We modeled the 8 mm A+B array continuum data by fitting an axisymmetric intensity profile to the continuum emission of each source. For all models, we deprojected the 8 mm visibility data to a fixed position angle (P.A.) and fixed inclination as determined through image-plane 2D Gaussian fitting of the disk candidates, and assumed the disks are circularly symmetric (Table 4.3). We discuss the validity of using a 2D Gaussian to estimate the inclination angle of these non-Gaussian candidate disks in Section 4.10. We azimuthally averaged the visibility data in the u,v-plane and binned the data in linearly spaced bins of width 50 kλ from 0 to 1500 kλ, switching to log-spaced bins from 1500 to 4000 kλ where the data becomes noisier in order to boost the signal-to-noise level at large u,v-distances. For bright sources with high signal-to-noise, we used 30 log-spaced bins for the long baselines, and we use 20 log-spaced bins for the long baselines in dimmer sources with lower signal-to-noise levels at large u,v-distances.

We fitted the real components of the deprojected, averaged, and binned profile to a simple disk model using a C-based implementation of `emcee`, an affine-invariant Markov chain Monte Carlo ensemble sampler (Goodman & Weare, 2010; Foreman-Mackey et al., 2013). While we do not model the envelope here, we do take into account a fixed free-free component of the emission. The imaginary components were assumed to be zero in the model since the sources are positioned at the phase center and assumed to be symmetric.

For sources with binary components or other nearby sources in the field of view, we subtracted the other sources in the field from the u,v-data before modeling to reduce ringing from off-center sources in the field when we deproject, azimuthally average, and bin the data. Fewer residuals from non-disk components allows for a better fit of the disk model to the u,v-data of the extended VANDAM sources. We used the CASA task CLEAN with a region around only the companions we wish to subtract out and with option usescratch=True to save model visibilities of the companions to the model data column of the MS file. We then

used the task UVSUB to subtract the model data column from the corrected data column with the residuals of only the extended source we wish to model written to the corrected data column.

For all sources we used CASA task FIXVIS to place the extended source we wish to model at the phase center of the visibility data set to reduce ringing in the final real component vs. u,v-distance plots (see Section 4.9).

4.4.1 Disk Model

The disk model mimics a Shakura-Sunyaev disk (Shakura & Sunyaev, 1973) with a power law temperature profile; the resultant model disk surface brightness profile is

$$I(r)_{disk} \propto \left(\frac{r}{R_c}\right)^{-(\gamma+q)} \exp\left\{\left(\frac{r}{R_c}\right)^{(2-\gamma)}\right\}, \tag{4.2}$$

where $I(r)_{disk}$ is the radial surface brightness distribution of the disk, q takes into account the temperature structure of the disk, γ is the power-law of the inner-disk surface density, and r is radius. R_c is a characteristic radius at which there is significant optical depth and disk material, making it a proxy for outer disk radius. This flux density profile is appropriate here because the 8 mm data is expected to be in the Rayleigh-Jeans tail of the dust emission. We assume our 8 mm data to be optically thin, because we do not expect optical depth effects at this long wavelength. Flux is given by $F = \int_0^\infty I(r)\ 2\pi r\ dr$. Flux, disk radius, and the power-law of the inner-disk surface density were free parameters in the fitting. We fitted a model disk for values of $q = [0.25, 0.50, 0.75, 1.00]$ to the observations in order to avoid over-fitting the data while exploring reasonable physical values of q.

We accounted for a lower-limit free-free point source component emanating from shocks in the protostellar jets (Anglada et al., 1998). Because point sources in the image domain have constant flux density at all u,v-distances, we account for the free-free component by calculating the average real component of the binned data with u,v-distance >1700 kλ and

include the average as a flat, linear component of the model (Table 4.2); the profiles become flat at values >1700 kλ in all sources (see visibility plots in Section 4.9). For sources where the average real component of the binned data at values >1700 kλ is less than or equal to zero, we do not subtract a lower-limit free-free point source component.

For the bright sources IRAS4A and IRAS4B, we do not fit the shortest (<350 kλ) baselines (corresponding to emission from scales larger than 0.71″ or 165 AU) to remove a majority of the envelope contamination. This does not completely eliminate the envelope emission, but it removes enough large-scale emission to model a disk component. We do not model an envelope component because for the majority of sources a disk model can explain most of the continuum flux. As demonstrated in Chapter 3 for Per-emb-14 (Figure 3.8), visibility profiles corresponding to $R^{-1.5}$ and $R^{-2.0}$ envelope surface density profiles (free-fall collapse and singular isothermal sphere envelopes) cannot alone account for the vast majority of the dust emission.

We note that while the observations have 12 AU resolution, we can model slightly smaller size scales in the u,v-plane. Also, 12 AU resolution reflects a minimum resolvable disk diameter, whereas we model disk radii; we expect to model radii accurately down to ∼8 AU, representing 1.5 beams resolved across the major axis of the disk.

4.5 Full VANDAM Survey Disk Modeling Results

Once model fitting was completed on the candidate disks, we generated disk model visibilities corresponding to the best-fit parameters. The best-fit model and residuals for each source were Fourier transformed, sampled at the same u,v-points as the data, and imaged using the same weighting as the data. We subtracted the model visibility from the data to produce a residual visibility set. Synthetic maps were created of the best-fit model disks. Residual maps were made by imaging the Fourier transformed visibilities after subtracting the model from the data in the u,v-plane. For each source, the binned observational data, best fit

model, and residuals are also shown. We image the data with robust=0.25 weighting, which is a trade off between slightly higher resolution at the expense of slightly worse sensitivity. With robust=0.25 weighting, the disks are extended and the outer parts of the disks are relatively well-detected over the noise level. We do not model the data in the image plane, however examining the results in both the image and u,v-planes is useful to study the full extent of the disks. See Section 4.9 for plots of modeling results both in image and u,v-planes.

The results of the disk only models are shown in Table 4.3. For most sources, $\chi^2_{reduced}$ values are near 1, indicating that our disk model accounts for the majority of the emission from the candidate disks. Thus, these sources are likely to be Class 0 and Class I disks rather than simply dominated by inner envelope structure (Chiang et al., 2008). The majority of the modeled candidate disks have modeled disk radii larger than 10 AU. $R = 10$ AU is an upper limit predicted by magnetic braking models (Dapp & Basu, 2010) during the Class 0 stage. While varying the fixed values of q with each model, the best fit γ will change enough that even when including uncertainties, the values γ between $q = 0.25$ and $q = 1.00$ will not be in agreement. Despite the uncertainty of γ in these sources as q varies, R_c—our proxy for outer disk radius—typically remains in agreement across all best fit models for each candidate disk.

Negative values of γ are unphysical for disks, indicating that the surface brightness would increase with increasing radius as distance from the central protostar increased. For most resolved sources, we find positive values of γ in at least one of the best fit models where $q = [0.25, 0.50, 0.75, 1.00]$. These trends, along with the $\chi^2_{reduced}$ values near 1 and relatively empty residual maps in the image plane (Section 4.9), indicate that Class 0 and I disks are likely present in the Perseus molecular cloud.

Table 4.3: 8 mm Best-fit Disk Modeling Results for Full VANDAM Survey

Source	q	γ	R_c (AU)	$\chi^2_{\rm reduced}$
SVS13B	0.25	$0.21^{+0.23}_{-0.20}$	$24.28^{+2.1}_{-1.7}$	2.194
	0.50	$0.42^{+0.25}_{-0.21}$	$25.50^{+1.9}_{-1.5}$	2.185
	0.75	$0.63^{+0.24}_{-0.22}$	$26.46^{+1.6}_{-1.4}$	2.175
	1.00	$0.85^{+0.26}_{-0.23}$	$27.28^{+1.4}_{-1.2}$	2.164
Per-emb-50	0.25	$0.08^{+0.02}_{-0.16}$	$21.9^{+0.8}_{-0.9}$	1.556
	0.50	$0.26^{+0.15}_{-0.17}$	$23.3^{+1.1}_{-1.0}$	1.558
	0.75	$0.44^{+0.16}_{-0.17}$	$24.6^{+1.4}_{-1.1}$	1.560
	1.00	$0.64^{+0.16}_{-0.18}$	$25.7^{+1.4}_{-1.3}$	1.563
Per-emb-14	0.25	$-0.11^{+0.16}_{-0.00}$	$28.5^{+2.3}_{-2.1}$	1.110
	0.50	$0.09^{+0.08}_{-0.21}$	$30.6^{+2.8}_{-2.3}$	1.114
	0.75	$0.27^{+0.17}_{-0.24}$	$32.5^{+2.2}_{-2.8}$	1.119
	1.00	$0.48^{+0.19}_{-0.23}$	$33.9^{+3.6}_{-3.1}$	1.123
Per-emb-30	0.25	$0.02^{+0.18}_{-0.31}$	$14.0^{+1.0}_{-0.9}$	1.100
	0.50	$0.20^{+0.04}_{-0.32}$	$14.9^{+1.9}_{-1.1}$	1.102
	0.75	$0.39^{+0.30}_{-0.34}$	$15.8^{+1.9}_{-1.3}$	1.104
	1.00	$0.59^{+0.14}_{-0.33}$	$16.5^{+31.3}_{-1.6}$	1.107
HH211-mms	0.25	$0.48^{+0.40}_{-0.78}$	$10.5^{+0.8}_{-0.8}$	1.009
	0.50	$0.65^{+0.43}_{-0.82}$	$11.0^{+1.0}_{-0.9}$	1.009

Continued on Next Page...

Values of q are fixed. Values of γ and R_c are determined from best-fit models.

Uncertainties reflect 90% confidence intervals.

Table 4.3 – Continued

Source	q	γ	R_c (AU)	$\chi^2_{\rm reduced}$
	0.75	$0.81^{+0.42}_{-0.79}$	$11.5^{+1.2}_{-1.2}$	1.009
	1.00	$1.01^{+0.44}_{-0.81}$	$11.9^{+1.4}_{-1.3}$	1.009
IC348 MMS	0.25	$-0.58^{+0.11}_{-0.11}$	$25.7^{+2.8}_{-2.2}$	1.085
	0.50	$-0.39^{+0.19}_{-0.11}$	$29.0^{+3.2}_{-2.6}$	1.096
	0.75	$-0.19^{+0.11}_{-0.27}$	$31.6^{+4.1}_{-2.9}$	1.107
	1.00	$0.02^{+0.07}_{-0.11}$	$33.7^{+4.3}_{-3.1}$	1.118
Per-emb-8	0.25	$0.01^{+0.16}_{-0.19}$	$19.0^{+1.2}_{-1.1}$	1.099
	0.50	$0.20^{+0.17}_{-0.20}$	$20.2^{+1.4}_{-1.3}$	1.107
	0.75	$0.40^{+0.17}_{-0.21}$	$21.2^{+1.6}_{-1.4}$	1.114
	1.00	$0.61^{+0.17}_{-0.20}$	$22.1^{+1.8}_{-1.6}$	1.122
NGC 1333 IRAS4B	0.25	$-0.43^{+0.42}_{-0.27}$	$14.7^{+3.8}_{-2.3}$	1.286
	0.50	$-0.25^{+0.29}_{-0.22}$	$16.3^{+3.8}_{-2.4}$	1.289
	0.75	$-0.07^{+0.30}_{-0.22}$	$17.7^{+4.2}_{-2.9}$	1.293
	1.00	$0.13^{+0.30}_{-0.20}$	$18.9^{+4.4}_{-3.2}$	1.297
Per-emb-25	0.25	$0.15^{+0.50}_{-0.35}$	$28.4^{+4.1}_{-3.3}$	1.321
	0.50	$0.36^{+0.49}_{-0.34}$	$27.5^{+4.6}_{-3.6}$	1.327
	0.75	$0.56^{+0.49}_{-0.34}$	$26.3^{+5.0}_{-4.0}$	1.334
	1.00	$0.78^{+0.52}_{-0.35}$	$25.0^{+5.5}_{-4.5}$	1.340

Continued on Next Page...

Values of q are fixed. Values of γ and R_c are determined from best-fit models.

Uncertainties reflect 90% confidence intervals.

Table 4.3 – Continued

Source	q	γ	R_c (AU)	$\chi^2_{\rm reduced}$
NGC 1333 IRAS1 A	0.25	$0.52^{+1.58}_{-0.66}$	$11.1^{+2.1}_{-1.5}$	1.087
	0.50	$0.68\ ^{+2.59}_{-0.99}$	$11.6^{+7.4}_{-2.2}$	1.089
	0.75	$0.88^{+2.24}_{-0.73}$	$12.0^{+3.3}_{-2.2}$	1.093
	1.00	$1.06^{+2.26}_{-1.10}$	$12.4^{+11.7}_{-2.9}$	1.096
Per-emb-62	0.25	$0.04^{+0.33}_{-0.27}$	$21.5^{+2.6}_{-2.0}$	1.059
	0.50	$0.22^{+0.34}_{-0.28}$	$23.0^{+3.0}_{-2.3}$	1.058
	0.75	$0.41^{+0.35}_{-0.29}$	$24.2^{+3.5}_{-2.6}$	1.058
	1.00	$0.61^{+0.35}_{-0.29}$	$25.3^{+3.9}_{-2.9}$	1.057
Per-emb-63	0.25	$1.95^{+11.28}_{-0.96}$	$20.8^{+7.3}_{-7.5}$	1.092
	0.50	$2.13^{+14.46}_{-0.99}$	$21.2^{+9.4}_{-7.5}$	1.093
	0.75	$2.33^{+7.78}_{-0.91}$	$21.6^{+12.0}_{-8.9}$	1.095
	1.00	$2.59^{+15.77}_{-1.35}$	$21.8\ ^{+12.1}_{-6.6}$	1.097
SVS13C	0.25	$-0.32^{+0.11}_{-0.10}$	$32.9^{+1.6}_{-1.4}$	1.638
	0.50	$-0.13^{+0.12}_{-0.11}$	$35.8^{+2.1}_{-1.8}$	1.656
	0.75	$0.08^{+0.13}_{-0.12}$	$38.2^{+2.6}_{-2.2}$	1.674
	1.00	$0.29^{+0.15}_{-0.12}$	$40.2^{+3.0}_{-2.8}$	1.691
NGC 1333 IRAS4A	0.25	$0.07^{+0.03}_{-0.03}$	$38.1^{+1.1}_{-1.0}$	1.642
	0.50	$0.27\ ^{+0.03}_{-0.03}$	$39.8^{+1.0}_{-1.0}$	1.588

Continued on Next Page...

Values of q are fixed. Values of γ and R_c are determined from best-fit models.

Uncertainties reflect 90% confidence intervals.

Table 4.3 – Continued

Source	q	γ	R_c (AU)	$\chi^2_{\rm reduced}$
	0.75	$0.48^{+0.03}_{-0.02}$	$41.2^{+1.0}_{-1.0}$	1.553
	1.00	$0.69^{+0.03}_{-0.02}$	$42.2^{+0.9}_{-0.9}$	1.535
NGC 1333 IRAS2A	0.25	$1.65^{+1.74}_{-0.72}$	$9.1^{+0.4}_{-0.4}$	3.853
	0.50	$1.86^{+2.40}_{-0.42}$	$9.3^{+1.0}_{-1.2}$	3.855
	0.75	$1.99^{+2.51}_{-0.73}$	$9.5^{+1.4}_{-1.3}$	3.861
	1.00	$2.18^{+2.35}_{-1.81}$	$9.7^{+1.1}_{-1.9}$	3.864
NGC 1333 IRAS1 B	0.25	$42.02^{+10.92}_{-1.55}$	$6.8^{+160.6}_{-2.4}$	1.302
	0.50	$42.46^{+12.25}_{-2.08}$	$6.8^{+8.8}_{-1.3}$	1.302
	0.75	$53.96^{+14.61}_{-2.00}$	$6.8^{+106.2}_{-1.9}$	1.302
	1.00	$36.71^{+8.72}_{-1.47}$	$6.8^{+970.4}_{-2.7}$	1.302
B5-IRS1	0.25	$-1.41^{+4.20}_{-0.22}$	$55.8^{+37383.5}_{-79.3}$	1.050
	0.50	$-1.21^{+5.30}_{-0.30}$	$88.6^{+395.2}_{-25.7}$	1.049
	0.75	$-0.99^{+5.47}_{-0.35}$	$116.8^{+728.8}_{-25.9}$	1.048
	1.00	$-0.76^{+2.77}_{-0.27}$	$135.9^{+1686.0}_{-74.0}$	1.047

Values of q are fixed. Values of γ and R_c are determined from best-fit models. Uncertainties reflect 90% confidence intervals.

The disk model includes a disk and point-source component but does not take into account envelope emission. The best-fit models were determined from the maximum likelihood, i.e.∼the lowest χ^2 value, of all models fit to the data. Values of q near 0.5 are predicted by theory (e.g., Chiang & Goldreich, 1997) for Class II protostars, which are more evolved than

the protostars in our sample. Values of q <0.5 for Class 0 and younger Class I sources are favored since the envelope mass reservoir is still large, and radiation is reprocessed from the protostar and directed back onto the disk, increasing the brightness of the outer disk relative to the inner regions of the disk and flattening the brightness distribution (D'Alessio, 1996). Indeed, the majority of our sources have lowest $\chi^2_{reduced}$ across all disk-only models for each source when $q = 0.25$.

4.5.1 Marginally Resolved Sources

We performed the disk modeling on all extended sources from the VANDAM survey which were nearly axisymmetric. Not all of these extended sources are disk candidates: disk modeling has revealed that Per35B and Per53 are not well-described by a disk. The results of the disk models have marginally resolved disks or are unphysical for disks, and their values of R_c have large uncertainties (Table 4.3). NGC 1333 IRAS1 B was marginally resolved and has extremely high, unphysical values of γ, and a disk radius less than a half beam. For NGC 1333 IRAS1 B, the model, with its steep γ and small radius, is approximating more closely an envelope profile than a disk profile, therefore we do not consider it a disk candidate. B5-IRS1 has no positive values for γ for any value of model q and is therefore inconsistent with a disk profile and not a candidate disk. On the other hand, NGC 1333 IRAS2A has the highest $\chi^2_{reduced}$ value of all modeled sources, and with a modeled disk radius of just ∼9 AU, the disk diameter is barely larger than the beam. We do consider NGC 1333 IRAS2A to be a candidate disk, but we note that this source may be a barely resolved disk with large amounts of envelope contamination to consider.

4.5.2 Description of Candidate Disk Modeling Results

The best-fit disk models for the candidate disks modeled in Segura-Cox et al. (2016) are reported and described in Chapter 3. We include the best-fit disk models in Table 4.3 with the rest of the VANDAM extended source model results for completeness. Plots of

the best fit results for each source in the image- and u,v-planes are included in Section 4.9, for the full sample of VANDAM extended sources. Here were discuss irregularities in the visibility profiles, as they were not included in Chapter 3. SVS13B and Per-emb-8 have minor extensions to the southwest, contributing to minor ringing in their respective visibility profiles. Per-emb-30 also has ringing in the visibility profile, likely due in-part to the small peak of emission to the southeast of the source. The candidate disk of IC348 MMS is irregularly shaped, also producing ringing in the visibility profile.

Per-emb-25 was estimated to have a disk along the north-south direction from image-plane Gaussian fitting. Gaussian fitting for the inclination and position angles is most uncertain in this source due to the asymmetric extensions protruding from the central protostar; however, the estimated disk position angle is roughly perpendicular to a known jet (Dunham et al., 2014a). The best-fit models of Per-emb-25 have $\chi^2_{reduced} \sim 1.33$, an intermediate value among the candidate disks. A central residual component is seen in the Figure 4.23, likely due to a small unmodeled envelope component. The modeled flux of the disk also falls below the zero-baseline flux (Figure 4.24), indicating that the inner few baselines may have a small envelope component. Figure 4.24 also shows ringing, especially at long baselines, likely due to the asymmetric dust extensions seen in the 8 mm data.

Per-emb-62 and Per-emb-63 and NGC 1333 IRAS1 A all have relatively low $\chi^2_{reduced}$ values near 1.10 despite mild ringing in the visibility profile. Per-emb-62 and Per-emb-63 have R_c slightly larger than 20 AU with irregular emission in the immediate vicinity surrounding the protostars, contributing to the ringing in Figures 4.28 and 4.30. Per-emb-63 is one of the least bright candidate disk sources and the point source component estimate is likely grossly overestimated from long baselines due to the ringing. The overestimate of the point source forces a dip in the model (Figure 4.30). A better-fit disk model for Per-emb-63 may be found by simply setting the point source component to zero. NGC 1333 IRAS1 A has a small peak of emission to the northwest (seen in Figure 4.25) as well as a companion that was subtracted from the visibility profile further from the candidate disk, both of which probably contribute

to the ringing seen.

The 8 mm emission from SVS13C is extended in both the east-west and north-south directions (Figure 4.31). A jet is present in the system along the north-south direction (see Section 4.6.2). The north-south emission is non-Gaussian and irregular, making subtraction of the north-south emission difficult. Because the east-west emission likely arises from a disk, we chose not to apply a taper by removing the shortest (<350 kλ) baselines to remove the larger scale north-south emission. A taper would also remove the the east-west emission to which we apply a disk model. We chose to proceed with the standard modeling procedure described in Section 4.4.1, without accounting for the jet-like north-south emission. The resulting best-fit models (Table 4.3) have a $\chi^2_{reduced} \sim 1.65$, an intermediate $\chi^2_{reduced}$ value for our modeled sources. The two model with the lowest $\chi^2_{reduced}$ have $q = [0.25, 0.50]$ with negative values of γ. While negative γ could indicate a hole in the innermost unresolved regions of a disk (Tazzari et al., 2017), the close to edge-on orientation of SVS13C ($\sim$75° inclination) would cause a hole to be hidden by disk emission. The models with $q = [0.75, 1.00]$ however have positive values of γ, consistent with a disk profile. All four best-fit models have $R_c \sim 35$ AU, revealing SVS13C to be the second largest modeled candidate disk in the VANDAM survey.

NGC 1333 IRAS4A is by far the brightest candidate disk in our sample (Table 4.2) with a known dense envelope (e.g., Looney et al., 2000). For imaging, we apply a taper to the shortest (<350 kλ) baselines, corresponding to large-scale emission, to remove a majority of the envelope contamination from the source and better reveal the disk component. As described in Section 4.4, we also do not fit the inner 350 kλ baselines to our disk model. A central component is left in the residuals (Figure 4.33), also seen in the inner baselines where the zero-baseline model flux does not match the zero-baseline data (Figure 4.34). We attribute this discrepancy to the unmodeled envelope component. The best fit model has a relatively steep $q = 1.00$ value for an embedded source, possibly influenced by the dense envelope.

NGC 1333 IRAS4B, like NGC 1333 IRAS 4A, also has a dense envelope of which we remove a majority of the emission by applying a taper to the inner 350 kλ during the imaging process. We also do not fit our disk model to these inner baselines (Section 4.4). In the Figure 4.21, we see there is a slight offset between the center of the 8 mm candidate disk and the center of the model. The off-center fit causes an over-subtraction of the east side of the candidate disk and an under-subtraction on the west side of the candidate disk. We also note that in the 8 mm data, the peak of the emission is slightly offset from candidate disk center. Both the offset peak and the offset from phase center likely contribute to the ringing seen in Figure 4.22. We can refine this model by recentering the 8 mm data to align with phase center in the *u,v*-data. The intermediate baselines of the visibility profile, where the disk emission dominates, remains well modeled, with $\chi^2_{reduced} \sim 1.29$, an intermediate value of $\chi^2_{reduced}$ amongst our candidate disks. R_c also remains near 16 AU for all best-fit models. Most values of q give negative best-fit values for γ, though the $q = 1.00$ best-fit model does give a positive value for γ consistent with disk emission.

NGC 1333 IRAS2A is the smallest candidate disk we model (Table 4.3). The small disk radius is reflected in Figure 4.36, with the disk-like gentle slope feature extending further in *u,v*-distance than any candidate disk source. NGC 1333 IRAS2A has a small asymmetric extension in the northwest direction, likely leading to the low-amplitude ringing in the visibility profile. A small residual is seen toward the center of the disk in the image plane, which we attribute to a small amount of unmodeled envelope emission.

4.6 Gallery of Candidate Disk Sources

In this Section we report the available information from literature for each VANDAM candidate disk source. We include available information on first observations, young stellar object classification, outflows, indirect evidence of disks, polarization observations, and notable features. The young stellar object classifications are based on T_{bol} from Enoch et al. (2009),

Sadavoy et al. (2014), and Young et al. (2015) unless otherwise noted. Outflow position angles are measured counterclockwise from north. Polarization observations are typically interpreted as tracing the magnetic fields of the environment surrounding the protostars, with the inferred magnetic field morphology rotated 90° from the polarized morphology (see Chapter 2), though we discuss other polarization mechanisms in Section 4.7.6.

4.6.1 Modeled Single Sources

Sources with no detected companions within 10,000 AU.

HH211-mms

Disk candidate HH211-mms is a Class 0 protostar in the IC 348 region of the Perseus molecular cloud with no known companions. A well-collimated jet was first detected in H_2 near infrared observations (McCaughrean et al., 1994), with HH211-mms confirmed as the driving source of the jet with CO observations (Gueth & Guilloteau, 1999). The position angle of the jet is ∼116° (Hull et al., 2014). The kinematic structure of the envelope was studied in N_2H^+ by CARMA, revealing a velocity gradient perpendicular to the jet (Tobin et al., 2011). HH211-mms was well-modeled by a disk profile in 8 mm continuum emission (Segura-Cox et al., 2016), with the disk parallel to the velocity gradient and perpendicular to the outflows.

A SCUPOL map with ∼4500 AU resolution toward HH211-mms showed inferred magnetic field morphology from polarization that is misaligned with the both bipolar outflow and VANDAM modeled disk orientation (Matthews et al., 2009). The orientation of the TADPOL survey CARMA ∼600 AU resolution polarized emission is consistent with the misaligned inferred magnetic field morphology on larger scales (Hull et al., 2014) and also traces a slight hourglass morphology (Girart et al., 2006). Polarization towards HH211-mms was also detected with the SMA with ∼150 AU resolution (Lee et al., 2014). The SMA polarized emission is present across only some parts of the protostar and has an unclear

inferred magnetic field morphology (see Section 4.7.6).

Per-emb-14

The single Class 0 protostar Per-emb-14 lies in the NCG 1333 region of Perseus, first noted by Wootten & Mangum (1993). This source has been referred to as NGC 1333 IRAS4C by some (e.g., Looney et al., 2000), though the IRAS4C name is typically used for the source $\sim$40″ from NGC 1333 IRAS4A (e.g., Rodríguez et al., 1999; Sandell & Knee, 2001). CARMA CO observations revealed bipolar outflows with a 95° position angle (Tobin et al., 2015a). Tobin et al. (2015a) also found a velocity gradient in $C^{18}O$ perpendicular to the outflow orientation. The VANDAM 8 mm continuum emission was modeled and consistent with a disk (Segura-Cox et al., 2016) parallel to the $C^{18}O$ velocity gradient, making Per-emb-14 a likely young embedded disk. Per-emb-14 was also resolved in continuum dust emission at 1.3 mm (Tobin et al., 2015a). The extent of the dust disk at 1.3 mm is a factor of $\sim$3 larger than the modeled 8 mm radius (Segura-Cox et al., 2016).

Per-emb-30

The Barnard 1 region hosts the Class 0 protostar Per-emb-30, first detected by Hatchell et al. (2005). This single source drives a monopolar H_2 jet with a position angle of 109° to the northwest of the source (Davis et al., 2008). An HCO^+ northwestern monopolar outflow was also detected near Per-emb-30 with a similar position angle (Storm et al., 2014). The outflow emission could be monopolar because an unseen southeastern component may be interacting with dense gas near the protostar while the ambient medium is less dense towards the northwest where we see the monopolar flow. The 8 mm continuum VANDAM data for Per-emb-30 was well-fit by a disk profile (Segura-Cox et al., 2016) with a mostly face-on ($\sim$30°) inclination.

Per-emb-50

The Class I protostar Per-emb-50 is located in the NGC 1333 region and was first detected in the near-infrared (Lada et al., 1996), with the detection confirmed later at submillimeter wavelengths with the JCMT (Hatchell et al., 2005). Per-emb-50 has no detected companions. Outflows were detected in CO with a position angle of $\sim$72° (Curtis et al., 2010), roughly perpendicular to the position angle of the 8 mm VANDAM continuum emission which was well-fit by a disk profile (Segura-Cox et al., 2016).

Per-emb-25

Per-emb-25 is a Class 0/I protostar first detected with *IRAS* (Ladd et al., 1993), near the L1452 region in Perseus. Outflows were detected in CO with JCMT and CSO with position angles near 110° (Dunham et al., 2014a). This protostar has no detected companions.

Per-emb-62

The Class I protostar Per-emb-62 is a single protostar and lies in the IC 348 region. It was first observed as part of an optical and near-infrared survey of the IC 348 region (Herbig, 1998) and has since been observed in millimeter/submillimeter wavelengths. A monopolar outflow emanating from Per-emb-62 was detected in CO with the JCMT (Hatchell & Dunham, 2009) with a position angle of $\sim$35°.

Per-emb-63

The Class I protostar Per-emb-63 is found in the NGC 1333 region. It was discovered with observations made by the Palomar Observatory (Cohen, 1980) and later confirmed with millimeter/submillimeter observations. This source is not known to have any companions, and it is unclear if it drives any outflows.

4.6.2 Modeled Multiple Sources

Sources with at least 1 companion detected within 10,000 AU, as reported in Tobin et al. (2016b).

Per-emb-8

The Class 0 protostar Per-emb-8 is a part of a wide binary system (∼2200 AU separation) along with the Class I protostar Per-emb-55 (Tobin et al., 2016b) in the IC 348 region of Perseus. Per-emb-8 was first detected in the *Spitzer* c2d survey (Rebull et al., 2007). Per-emb-55 contains two protostars separated by less than 150 AU (Tobin et al., 2016b), bringing the total protostellar count of the system to three. CO observations revealed bipolar outflows emanating from Per-emb-8 with a position angle of ∼15° (Lee et al., 2016). We modeled the 8 mm VANDAM continuum in Segura-Cox et al. (2016) with a disk-shaped profile, roughly perpendicular to the bipolar outflows.

IC348 MMS

IC348 MMS is a Class 0 source in the IC 348 region, detected first via its molecular H_2 outflows (Eislöffel et al., 2003). IC348 MMS is a multiple with ∼1500 AU separation (Chen et al., 2013), with a third closer component identified more recently (Rodríguez et al., 2014). Tobin et al. (2016b) denotes our candidate disk modeled here as Per-emb-11-A. The closer companion, Per-emb-11-B appears to be directly between outflow cavities detected in CO with a position angle of ∼150° (Pech et al., 2012) while Per-emb-11-A lies to the side of the outflow cavity (Tobin et al., 2016b), indicating that our candidate disk may not be the central driving source of the outflows in the system. In Segura-Cox et al. (2016), we found the 8 mm VANDAM continuum data was well-fit by a disk profile extended perpendicular to the outflows.

As a part of our larger VANDAM survey, we are analyzing the polarized continuum

emission towards all Class 0 and I protostars in Perseus with ∼65 AU resolution (Cox et al. in preparation). Polarized 8 mm emission was detected towards IC348 MMS. The inferred magnetic field orientation is parallel to the outflows and perpendicular to the orientation of the modeled disk.

NGC 1333 IRAS4A

NGC 1333 IRAS4A is the brightest protostar in our sample of disk candidates (Table 4.2). Located in the NGC 1333 region, NGC 1333 IRAS4A has been long known to be a Class 0 protostar based on it's SED (Sandell et al., 1991; Andre et al., 1993), and was first observed at 50 and 100 μm with *IRAS* (Jennings et al., 1987). To date, there has been no confirmation of Keplerian rotation, hard evidence of a disk, in NGC 1333 IRAS4A due to the dense envelope surrounding the protostar, making observations difficult. NGC 1333 IRAS4A has a close Class 0 companion (separation ∼580 AU, Hull et al., 2014) called NGC 1333 IRAS4A2, first detected at 0.84 mm (Lay et al., 1995), with the binary system sharing a common envelope (Looney et al., 2000). The binary system has been resolved at multiple wavelengths (Looney et al., 2000; Jørgensen et al., 2007; Reipurth et al., 2002). Distinct outflows from each source were resolved in SiO, SO, and CO (Santangelo et al., 2015). Lee et al. (2016) found the outflows of our candidate disk NGC 1333 IRAS4A, as traced by CO, to have a position angle of ∼19°. The line-of-sight velocities detected in the CO outflows indicate that the system has an inclination of <45° (Hull et al., 2014), consistent with our measured inclination (Table 4.2). NGC 1333 IRAS 4A revealed low- and high-density molecular lines tracers with inverse P-Cygni profiles (Jørgensen et al., 2007; Di Francesco et al., 2001). The inverse P-Cygni profiles are consistent with material infalling onto the binary protostar system. Inner-envelope scale kinematic observations have revealed a velocity gradient in the east-west direction across the source (Yen et al., 2015), roughly perpendicular to the outflows and consistent with a disk present in the system.

Polarized observations of dust emission towards NGC 1333 IRAS4A have been made at

850 μm, 1.3 mm, and 8 mm with SCUPOL, SMA and CARMA, and the VLA respectively (Matthews et al., 2009; Girart et al., 2006; Hull et al., 2014; Cox et al., 2015). The SCUPOL data, on ∼4500 AU scales traces a uniform inferred magnetic field oriented in the northeast-southwest direction. The SMA data, with ∼300 AU resolution, shows an inferred magnetic field consistent with the larger scale SCUPOL field and reveals one of the first hourglass-shaped inferred magnetic field morphologies towards a low-mass protostar. The TADPOL survey CARMA data also have an inferred magnetic field with an hourglass shape. The 8 mm VLA polarization data (∼65 AU resolution) was observed as a part of the larger VANDAM survey; 10 mm VANDAM polarized emission was also detected with the same morphology as the 8 mm data (Cox et al., 2015). The inferred magnetic field orientation from the polarized VLA emission reveals a circular morphology circling the face of the modeled candidate disk, a stark contrast to the hourglass morphology on larger scales.

NGC 1333 IRAS4B

Candidate disk NGC 1333 IRAS4B is a Class 0 protostar in the NGC 1333 region, with the wide binary Class 0 companion IRAS4B0 at a separation of ∼2450 AU (Tobin et al., 2016b). While NGC 1333 IRAS4B was first discovered at 800 and 450 μm (Sandell et al., 1991), IRAS4B0 is the dimmer companion and was discovered later (Sandell & Knee, 2001; Di Francesco et al., 2001). Both protostars drive compact outflows, which lie in almost perpendicular directions (Hull et al., 2014), with NGC 1333 IRAS4B's bipolar outflow lying in the north-south direction with a position angle of 15°° in CO (Lee et al., 2016). Proper motions of water masers in the outflow of NGC1333 IRAS4B indicate that the outflow-driving disk is viewed mostly edge-on (Marvel et al., 2008).

Polarization observations with SCUPOL (∼4500 AU; Matthews et al., 2009) and CARMA (∼600 AU; Hull et al., 2014) both have inferred magnetic field morphologies aligned east-west near protostar NGC 1333 IRAS4B. The inferred magnetic fields are perpendicular to the outflow and parallel to the candidate disk modeled in 8 mm.

NGC 1333 IRAS2A

NGC 1333 IRAS2A is a relatively well-studied Class 0/I protostar in NGC 1333, reported first in Jennings et al. (1987). The IRAS2 core hosts at least three embedded young stellar objects (Sandell & Knee, 2001), with NGC 1333 IRAS2A emitting the brightest at millimeter wavelengths. Two bipolar outflows, almost orthogonal to each other, appear to arise from NGC 1333 IRAS2A in both single dish (Sandell et al., 1994) and higher-resolution interferometric CO observations (Engargiola & Plambeck, 1999). The north-south outflow has a position angle of $\sim$25° while the east-west outflow has a position angle of $\sim$104° (Hull et al., 2014). Two orthogonal outflows do not have a clear, theoretical launching mechanism from a single disk, so this is taken as evidence of a close multiple system (Jørgensen et al., 2004). High-resolution observations of NGC 1333 IRAS2A did not find close companions (Looney et al., 2000; Maury et al., 2010) until the VANDAM survey resolved a binary source with $\sim$140 AU separation (Tobin et al., 2015b). The close binary components are referred to as VLA1 and VLA2; our candidate disk is VLA 1. Tobin et al. (2015b) concluded that our candidate disk drives the the north-south outflow, with VLA2 likely driving the east-west outflow.

NGC 1333 IRAS2A has polarization emission, with the inferred magnetic field orientation directly associated with the protostellar peak oriented in the east-west direction (Hull et al., 2014). The inferred magnetic field is misaligned with both the north-south outflow associated with NGC 1333 IRAS2A and the candidate disk orientation and may reflect an hourglass morphology (Girart et al., 2006).

NGC 1333 IRAS1 A

The Class I protostar NGC 1333 IRAS1 A is located on the edge of the NGC 1333 region, and has a binary source $\sim$440 AU away (Tobin et al., 2016b). This source was first detected by *IRAS* observations of the NGC 1333 region (Jennings et al., 1987). The outflow which originates from the system has an S-shape (Gutermuth et al., 2008), likely due to binary

interactions altering outflow morphology (Tobin et al., 2016b). The outflow has a position angle of ∼110° (Lee et al., 2015).

SVS13B

SVS13B is a Class 0 protostar in NGC 1333. It is a part of the larger protostellar multiple system SVS13 (Strom et al., 1976), which is comprised of SVS13A, SVS13B, and SVS13C (Looney et al., 2000) SVS13B was first detected at ∼3 mm (Grossman et al., 1987), and later confirmed with more sensitive observations (Chini et al., 1997). SVS13B is ∼3400 AU and ∼4500 AU from SVS13A and SVS13C, respectively (Tobin et al., 2016b). SVS13A is a Class 0/I protostar, while SVS13B and SVS13C are Class 0 sources. SiO emission revealed an outflow emanating from SVS13B with a position angle of 160° (Bachiller et al., 1998), agreeing well with the outflow position angle of ∼170° from CO observations (Lee et al., 2016). The 8 mm VANDAM continuum data for SVS13B was previously modeled and consistent with a protostellar disk profile (Segura-Cox et al., 2016).

Polarized emission was detected towards SVS13B at 1.3 mm with CARMA (Hull et al., 2014). The inferred magnetic field morphology from polarization orientation reflects an hourglass morphology (Girart et al., 2006), with the average orientation misaligned with both the outflows and modeled candidate disk orientation of the system.

SVS13C

The SVS13 system in NGC 1333 also hosts SVS13C, a Class 0 protostar first identified by Chini et al. (1997) and later confirmed at 2.7 mm by Looney et al. (2000). A molecular outflow in the north-south direction was first identified by Plunkett et al. (2013), and an outflow position angle of 0° was later found with more sensitive CO observations (Lee et al., 2016). Kinematics reveal the outflow to be nearly in the plane of the sky (Plunkett et al., 2013; Lee et al., 2016), indicating that the disk launching the outflow should be nearly edge-on.

4.6.3 Complicated Sources

These are extended sources which cannot be modeled by our axisymmetric disk model due to irregular structures, asymmetry, or close-separation binaries. These sources are extremely extended and have indirect evidence of disks; we consider these sources VANDAM candidate disks even without disk modeling.

IRAS 03292+3039

IRAS 03292+3039 is a Class 0 protostar first detected by *IRAS* (Bachiller et al., 1990) in the Barnard 1 region, and it is the most spatially extended protostellar system out of all protostars detected by the VANDAM survey. This system is comprised of two close components separated by ∼18 AU, resolved with the A array VANDAM data (Tobin et al., 2016b). The extended resolved structure is non-axisymmetric and includes a southern extension, hence we are unable to model this source according to our prescription in Section 4.4. Indications of rotation in IRAS 03292+3039 were seen on 1000 AU scales in $C^{18}O$ (Yen et al., 2015), which appear to be roughly perpendicular to a known bipolar outflow with an orientation of 127° (Schnee et al., 2012).

IRAS 03282+3035

The Class 0 protostar IRAS 03282+3035, first observed as a low-luminosity *IRAS* source (Bachiller et al., 1991), was identified as a binary in millimeter emission (Chen et al., 2007). IRAS 03282+3035 is an isolated protostellar system near the Barnard 1 region (Jørgensen et al., 2006). IRAS 03282+3035 is a close multiple system with ∼22 AU separation between components resolved with A array VANDAM data (Tobin et al., 2016b). While in the combined A+B array VANDAM data the system appears as a single core, the close binary introduces enough deviations from symmetry that we cannot model this candidate disk. An outflow was detected in CO with a 125° position angle (Lee et al., 2015). CARMA N_2H^+

observations (Tobin et al., 2011) revealed a velocity gradient both along the outflow, and a component perpendicular to the gradient on the southeast side of the envelope, which could be consistent with a deeply embedded rotating disk.

Per-emb-18

Per-emb-18 is a Class 0 protostar, which is a part of the larger NGC 1333 IRAS7 system detected first in the near infrared (Aspin et al., 1994). Per-emb-21 and Per-emb-49 were also previously known protostars in NGC 1333 IRAS7. Per-emb-18 and Per-emb-49 were found to have close companions (<100 AU separations), meaning NGC 1333 IRAS7 is a quintuple system (Tobin et al., 2016b). An H_2 outflow was found in the system with a position angle of 159° (Davis et al., 2008). Per-emb-18 shows lopsided dust structures in the VANDAM data extended roughly perpendicular to the outflows, with the bright western structure harboring a double source with ∼20 AU separation in A array data (Tobin et al., 2016b).

L1448 IRS3B

L1448 IRS3B is a Class 0 protostar first detected in NH_3 (Bachiller & Cernicharo, 1986) with two long-known companions, L1448 IRS3A and L1448NW (Terebey & Padgett, 1997; Looney et al., 2000), with ∼2750 AU and ∼4950 AU separations from our survey respectively (Tobin et al., 2016b). L1448 IRS3B is itself a close triple system and L1448NW is a double (Tobin et al., 2016b), making the protostars part of a sextuple system. Tobin et al. (2015a) first reported two compact sources in L1448 IRS3B with CARMA data, before the third component was resolved later with the VLA. L1448 IRS3B and L1448NW are Class 0 protostars while L1448 IRS3A is a Class I source–older and less embedded than its companions (O'Linger et al., 2006). CO observations reveal an outflow with a position angle of 122° (Lee et al., 2016), though the outflow was also detected on larger scales with CO previously (Kwon et al., 2006). The blueshifted lobe from L1448 IRS3B overlaps and may interact with the outflow from L1448NW (Hull et al., 2014). 2.7 mm continuum emission

from L1448 IRS3B revealed a protostellar envelope elongated almost perpendicular to the outflow (Looney et al., 2000). A velocity gradient along the extended envelope was found with $C^{18}O$ observations (Yen et al., 2015).

ALMA Band 6 (1.3 mm) observations of the L1448 IRS3B triple source revealed a disk with spiral arms surrounding the three protostars (Tobin et al., 2016a). The spiral arm structure and the placement of the protostars with in them demonstrate that protostellar disks can undergo gravitational instability at early times, and may form hierarchical multiples. ALMA $C^{18}O$ maps from Tobin et al. (2016a) also revealed a velocity gradient perpendicular to the outflows and centered around two of the three protostars, with the third—and brightest—protostar of the system lying closer to the edge of the disk.

Polarization towards L1448 IRS3B was detected on ∼2500 AU, ∼1000 AU, and ∼600 AU size scales with SCUPOL, BIMA, and CARMA respectively (Matthews et al., 2009; Kwon et al., 2006; Hull et al., 2014). The inferred magnetic field orientation on all scales is nearly perpendicular to the outflow and parallel to the velocity gradient in $C^{18}O$ (Yen et al., 2015; Tobin et al., 2016a).

4.7 Discussion

4.7.1 Candidate Disk Properties

The 19 VANDAM candidate disks have estimated masses of 0.01–3.2 $M_\odot$ (Table 4.2). As discussed in Section 4.3, the estimated mass of L1448 IRS3B is likely under-estimated, and NGC 1333 IRAS4A is an unusual outlier with estimated masses an order of magnitude larger than all other sources. The remaining 17 candidate disks have disk masses of 0.02–0.71 $M_\odot$. Our values for the estimated masses of the candidate are all larger than the Minimum Mass Solar Nebula, the 0.01 $M_\odot$ amount of material expected to be required to form the planets in our own Solar System (Weidenschilling, 1977), indicating that these disks will likely eventually form planets.

When scaled to our opacity, the Class 0 protostar L1527's disk mass is 0.013 $M_\odot$ (Tobin et al., 2013a) with $T_d = 30$ K. Harsono et al. (2014) revealed four Class I disks to have masses of 0.004-0.033 $M_\odot$, using $T_d = 30$ K and Ossenkopf & Henning (1994) opacities. Compared to these embedded disks, our disk masses appear to be over estimated. One possibility is that our assumption of dust opacity spectral index $\beta = 1$ is too large. L1527 was found to have a shallower $\beta \sim 0$ (Tobin et al., 2013a) from ∼mm wavelengths, which could be attributed to a population of large (∼cm) dust grains centered in the disk midplane with a smaller scale height than observed at shorter wavelengths. Our 8 mm data indeed do trace large grains settled in the midplane, indicating that values of β near 0 may be more common than previously thought for deeply embedded young disks, as suggested by Kwon et al. (2015).

Our best-fit models for 15 candidate disks give -0.58 $< \gamma <$ 1.95 (Table 4.3), with the average value of inner-disk surface density power law $\gamma = 0.38$ for our Class 0 and I sources. Negative values of γ imply increasing disk surface density with radius, incongruent with typical disk profiles. For all our candidate disks at least one value of q, the disk temperature structure parameter, produces a positive best-fit value of γ. The average value of $\gamma = 0.38$ is a shallower profile than more evolved disks. Disks around Class II protostars in Ophiuchus yield an a typical value of $\gamma = 0.9$ (Andrews et al., 2009). The steeper values of γ in Class II sources indicates that evolved disks are generally more centrally concentrated than our Class 0 and I disks.

The few Class 0 disks with Keplerian rotation have relatively large radii, though it is unclear if these are typical radii of young disks or if this is simply detection bias towards large and bright sources. At 1.3 mm, VLA 1623 has R ∼189 AU (Murillo et al., 2013), Lupus 3 MMS has R ∼100 AU (Yen et al., 2017), and L1527 has R ∼54 AU (Ohashi et al., 2014). HH212 has R >30 AU in 850 μm data (Codella et al., 2014). Our Class 0 and I VANDAM candidate disks have 9.1 AU $< R_c <$ 42.2 AU. The modeled radii (Table 4.3) give disk diameters that are a factor of 1 to 1.5 times larger than the deconvolved sizes from the image-plane Gaussian fits (Table 4.2). For most sources, the candidate Class 0 and I disks

are larger than the expected upper limit of 10 AU from strong magnetic braking models (Dapp & Basu, 2010). HH211-mms, NGC 1333 IRAS1 A, and NGC 1333 IRAS2A are the three smallest disks with R_c ∼10 AU. The remaining candidate disks have R_c consistent with the radii of Keplerian Class 0 disks L1527 and HH212.

4.7.2 The Frequency of Class 0 and I Candidate Disks

With the VANDAM survey, we have detected 19 new candidate disks (15 Class 0 and 4 Class I) in the deeply embedded, young protostellar phases. Our survey has more than doubled the number of known possible disks around Class 0 and I protostars, bringing the total count from ∼15 to ∼34. With so many young disks and candidate disks now known, we can characterize typical young embedded disk frequency and dust properties, determine the relative rarity of large embedded disks, look for evolutionary trends between the protostellar phases, and begin to study the role magnetic fields play during the early stages of disk growth.

Of the Class 0 protostars (including Class 0/I sources) in Perseus, 15/43 (35%) have candidate disks on scales of 12 AU or larger. Only 4/37 (11%) of Class I protostars in our sample have large, resolved candidate disks. Here we have included both the modeled and unmodeled complicated candidate disks in our counts. We also find that 61/80 (76%) of Class 0 and I protostars do not have signs of disks within our 12 AU resolution limit. Since disk formation in protostars is expected to be a natural consequence of conservation of angular momentum during core collapse, this implies that at 8 mm most disks in the Class 0 and I phases are small (<10 AU). The population of small, unresolved disks may undergo stronger magnetic braking or be subject to other processes limiting disk growth.

The lower proportion of Class I candidate disks compared to Class 0 candidate disks is surprising because naively, the disk is expected to grow from the Class 0 to the Class I stage as the envelope is dissipated in part by accreting onto the disk, though no correlations between disk masses or radii have yet been found between the Class 0 and I phases (Williams &

Cieza, 2011). The Class I candidate disks in Perseus may suffer from small-number statistics since only 4 Class I candidate disks were detected and may not reflect typical Class I disk frequency in other molecular clouds.

An alternative explanation for the low proportion of VANDAM Class I candidate disks lies in the size of the dust grains seen in our observations. Our data trace large dust grains ($\sim$8 mm), since thermal emission from dust roughly traces the size of the emitting grains. It is possible that the candidate disks around more evolved Class I protostars have been stable long enough for radial drift (Pérez et al., 2012) to cause the 8 mm dust grain population to be more centrally concentrated around the protostar relative to Class 0 sources (Figure 4.2 may also support this scenario; see Section 4.7.3). The detectable 8 mm radius of an embedded disk may shrink as the protostar evolves due to 8 mm grain population radially drifts inwards causing the SNR in the outer disk to decrease below instrument sensitivity thresholds. If disks detected at 8 mm do become more centrally concentrated as they evolve with a smaller detectable radius, Class I candidate disks may have had larger 8 mm disks in the past which may have been detected with 12 AU resolution, but at present the 8 mm disks may have shrunk to below resolution or sensitivity limits.

Figure 4.1 shows a histogram of all 15 modeled candidate disk radii, including 11 Class 0 and 4 Class I sources. The four non-axisymmetric sources could not be modeled to derive a disk radius and are not included in this histogram. Both the Class 0 and Class I candidate disk distributions peak at 15-30 AU radii, which are well resolved with the 12 AU resolution observations. The two largest disks, with radii 30-25 AU both belong to Class 0 sources. With so few Class I protostars sampled, any further differences between the Class 0 and I candidate disk radii are difficult to distinguish.

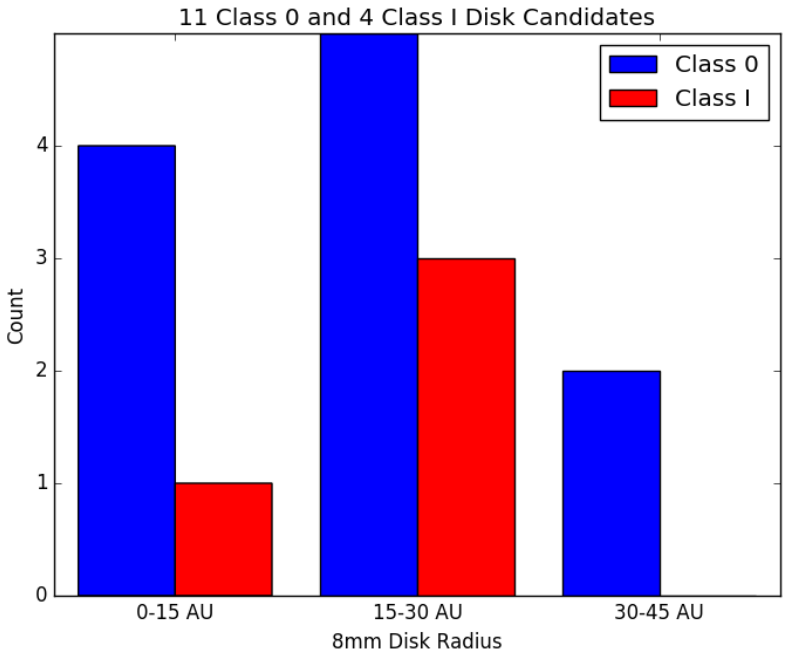

Figure 4.1: A histogram of the radii of all 15 modeled candidate disks.

4.7.3 Trends between Candidate Disk Characteristics and Protostellar Age

As seen in Figures 4.3-4.2, no tight correlations between protostellar age (using bolometric temperature, T_{bol}, as an indicator of protostellar evolution; Chen et al., 1995), measured flux, modeled candidate disk radius, and modeled inner-disk surface density power law γ are found by eye. In these plots, Class 0/I sources are counted as Class 0 and we include all 15 modeled VANDAM candidate disks. Bolometric temperatures were taken from Tobin et al. (2016b). We see no significant differences between single and multiple candidate characteristics with age, nor any significant differences between Class 0 and Class I candidate disk characteristics with age.

A mild correlation between γ, the power-law of the inner-disk surface density, and T_{bol} (Figure 4.2) may be present with a tentative trend of higher values of γ being found in older sources with higher T_{bol}. Higher values of γ indicates that flux drops off faster with

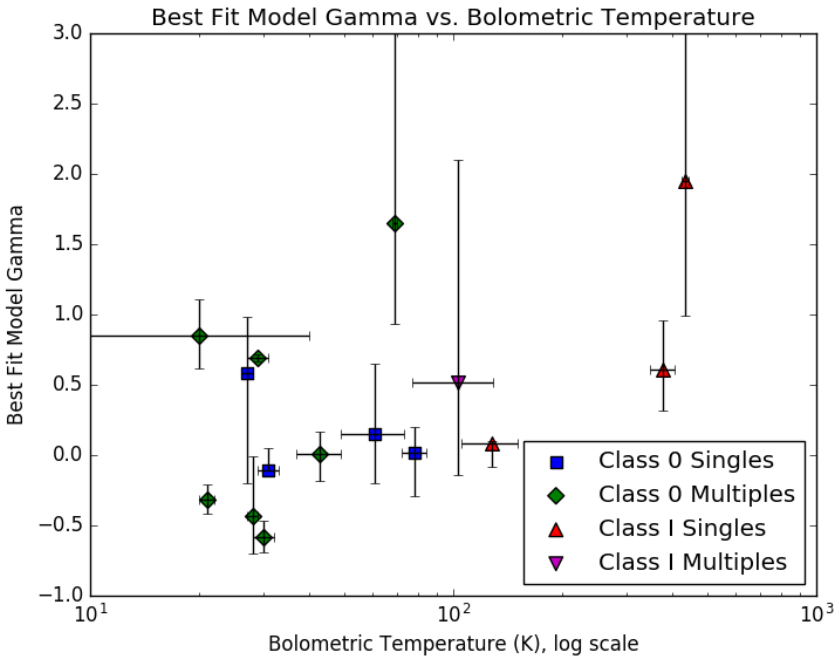

Figure 4.2: A mild correlation between T_{bol} and modeled inner-disk surface density power law γ is seen by eye, with a weak trend of more evolved sources with higher T_{bol} having higher values of γ.

increasing radius, meaning 8 mm flux is more centrally distributed for younger sources than more evolved sources with higher T_{bol}. This may be explained as dust grains in more evolved sources having more time to experience radial drift (Pérez et al., 2012) and concentrate closer to the central protostellar source. As further evidence, in Section 4.7.2 we demonstrated that the typical value of γ grows larger from the young Class 0/I stage to the more evolved Class II/III phases.

If there are truly no correlations between disk radius or flux and age, a process independent of evolution could be setting the disk radii. Possible processes independent of age that could influence the disk radii include the initial angular momentum imparted onto the disk from the natal protostellar core (e.g., Terebey et al., 1984) or magnetic braking dominating over any evolutionary effects (e.g., Dapp & Basu, 2010). Alternatively using T_{bol} as an indicator of protostellar evolution may be imprecise. Certainly it is clear that there are no major differences in typical disk fluxes or radii between the Class 0 and Class I phases.

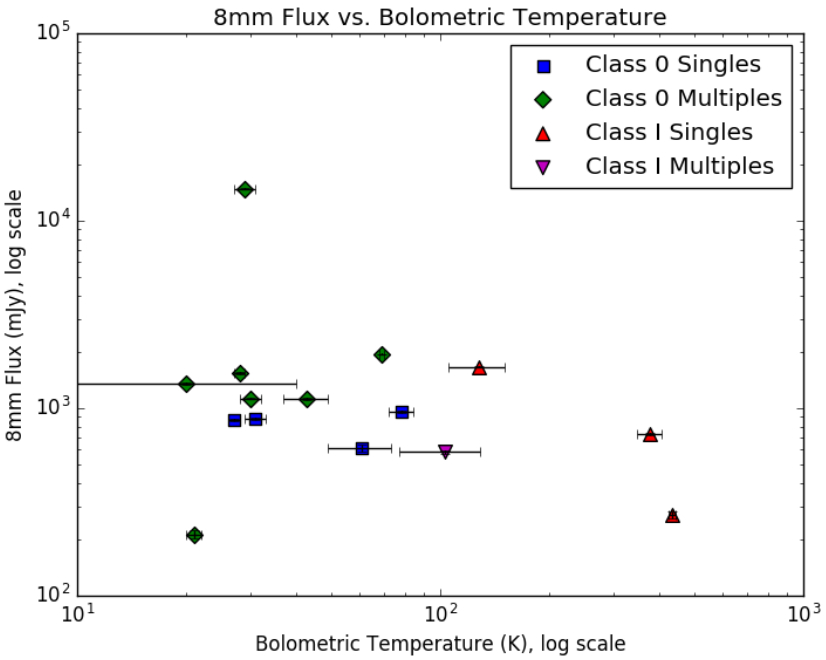

Figure 4.3: No clear correlations are seen between T_{bol} and 8 mm flux.

Additionally, in Figures 4.5-4.6, no correlations are seen between measured flux and modeled radius, or modeled radius and modeled γ. Again no clear differences are seen in the characteristics between the single and multiple populations or the Class 0 or Class I phases.

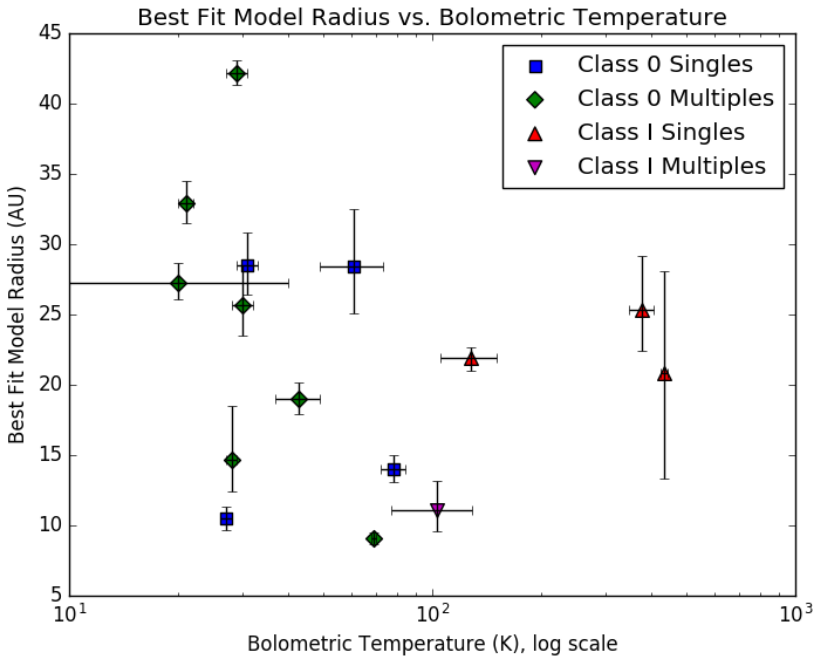

Figure 4.4: No clear correlations are seen between T_{bol} and modeled R_c.

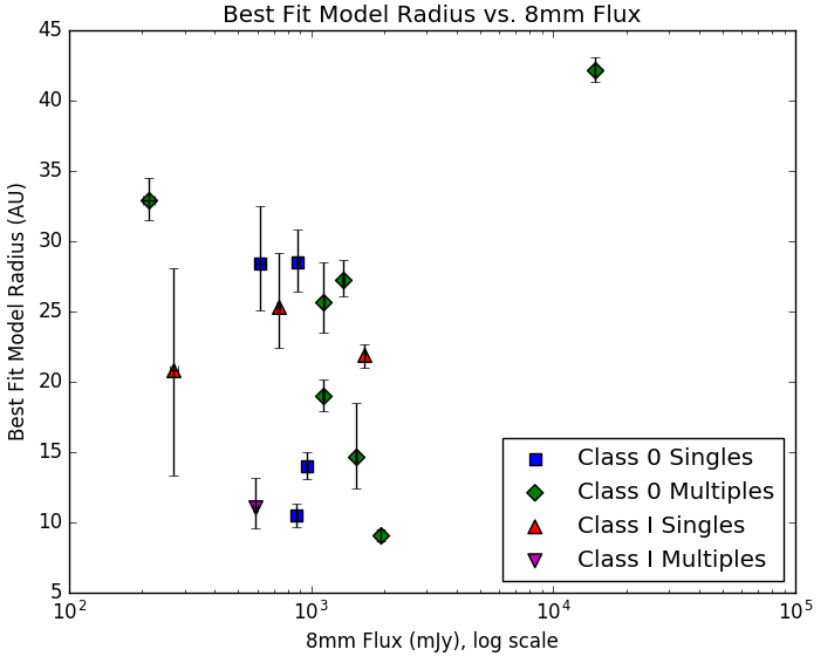

Figure 4.5: No clear correlations are seen between 8 mm flux and modeled R_c.

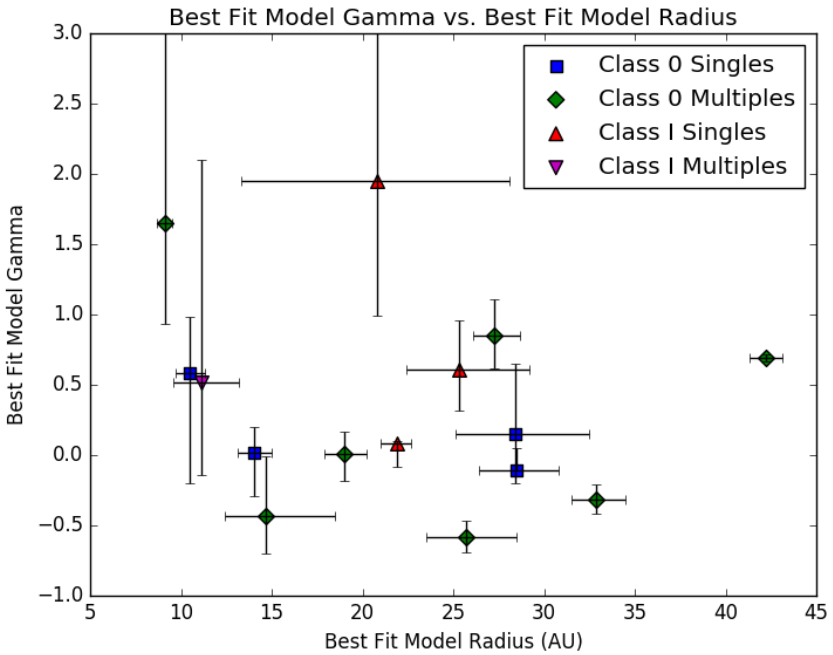

Figure 4.6: No clear correlations are seen between modeled R_c and modeled γ, the power-law of the inner-disk surface density.

4.7.4 8 mm Emission as a Lower Limit on Dust Disk Radius

As noted in Section 4.6.1, Per-emb-14 was resolved in continuum dust emission at 1.3 mm (Tobin et al., 2015a) with a dust disk a factor of ∼3 larger than our modeled 8 mm continuum radius (Segura-Cox et al., 2016). A dependance on disk size with wavelength was also found for the more evolved classical T Tauri star AS 209 (Pérez et al., 2012), with disk size decreasing with longer wavelength observations. Since the wavelength of thermal emission from dust grains roughly traces the radii of the dust grains, 8 mm emission traces a population of larger sized grains than in 1.3 mm emission. The larger 8 mm grains experience radial drift to a larger extent (Pérez et al., 2012), forming a more compact disk closer in to the central protostar than smaller grains which remain further from the protostar for longer periods of time (e.g., Birnstiel et al., 2010). At shorter wavelengths, near 1 mm, dust emissivity is higher causing the dust emission to be stronger in the outer parts of the disk and more likely to be detected. We consider our VANDAM modeled disk radii at 8 mm to be extreme lower limits on disk size. Shorter wavelength observations may be better tracers of the full extent of circumstellar dust disks due to these large-grain settling effects and surface brightness sensitivity limits at 8 mm.

4.7.5 Outflow Orientations as Indirect Evidence of Disks

Nearly all VANDAM candidate disks, except for Per-emb-63, have clearly associated outflows roughly perpendicular (60-90°) to the major axis of the candidate disks (see Section 4.6). No outflows are associated with Per-emb-63. The orientations of outflows have been used as proxies for the disk rotation axis (e.g., Hull et al., 2013), hence outflows nearly perpendicular to extended continuum emission is a strong indicator of a protostellar disk. Along with our continuum emission disk modeling, we use the perpendicular outflows as indirect evidence of rotationally supported disks in embedded sources.

HH211-mms, Per-emb-14, Per-emb-15, Per-emb-25, Per-emb-8, SVS13B have with bipo-

lar outflows perpendicular to their candidate disk elongation. Per-emb-30 and Per-emb-62 both have single monopolar outflows, possibly because of dense gas interacting with unseen components of their bipolar outflows. Their detected monopolar outflows are both perpendicular to their candidate disk directions.

IC348 mms does not appear to be the central driving source of the bipolar outflow in its binary system though the candidate disk remains perpendicular to the outflow. NGC 1333 IRAS4A has a close binary companion, each with bipolar outflows perpendicular to the estimated disk position angle of our candidate disk. The binary system NGC 1333 IRAS2A is a part of drives two bipolar outflows, one coming from each close-separation component. The NGC 1333 IRAS2A candidate disk is perpendicular to the outflow associated with its protostar. NGC 1333 IRAS1 A drives an outflow almost perpendicular to its candidate disk and has a binary companion, which may be causing the outflow to have an S-shape via gravitational interactions between the binary protostars.

SVS13C drives a bipolar outflow perpendicular to the candidate disk. We detect evidence of the outflow in our 8 mm data. As seen in Figure 4.31, right panel, the east-west emission component of SVS13C is well modeled with minimal residuals, while the north-south jet-like (likely free-free) emission, remains. Because we already accounted for a point-source component in our model, we did subtract out any small-scale free-free emission coming from the jet-launching regions of the disk (Anglada et al., 1998), leaving minimal residual at target center.

The non-axisymmetric candidate disks (Section 4.6.3) cannot be fit with our modeling procedure, and for most the orientation of the candidate disk is unclear from 8 mm continuum data alone. IRAS 03292+3039 has a bipolar outflow perpendicular to a velocity gradient across the protostar, consistent with a disk. IRAS 03282+3035 is a very close separation binary, with velocity gradients both along the outflow, and a gradient perpendicular to the outflow, which could be consistent with a deeply embedded rotating disk. The 8 mm data of Per-emb-18 is highly elongated along the direction perpendicular to the outflow. Finally,

the triple system L1448 IRS3B has a velocity gradient perpendicular to the outflows that are centered on two of the three triple components.

4.7.6 Candidate Disk Sources with Detected Polarized Emission

There are three proposed mechanisms that cause polarized emission in protostellar sources. Polarization may be caused by dust grains interacting with the magnetic field. Elongated spinning dust grains are expected to align their short axis parallel to the magnetic field, resulting in polarization orientation perpendicular to the magnetic field (e.g., Lazarian, 2007). In the midplane of the disk, MRI dominates at scales larger than 10 AU, requiring toroidal fields, which are flux-frozen into the disk material and wrapped around the protostar with disk rotation (Balbus & Hawley, 1998). Polarization may also be due to Rayleigh scattering of radiation from the disk and central protostar if grain sizes are not much smaller than the observational wavelength (Kataoka et al., 2015). A new polarization mechanism of dust continuum emission has been posited: radiative alignment of grains with radiation anisotropy (Tazaki et al., 2017). This new radiative alignment scenario causes larger grains (>mm size), which are not expected to align with the magnetic field, to be aligned by radiative torques from an anisotropic radiation source with their short axes perpendicular to the direction of the radiative flux, causing polarized emission. These polarization mechanisms will produce different patterns of polarization morphology and have different efficiencies at varying wavelengths, though determining the definitive contributing mechanisms in any given source is not straightforward and requires detailed modeling (Yang et al., 2016).

Even when a magnetic field is present, elongated dust grains may not align with the magnetic field if high gas densities cause sufficient random collisions to prevent grain alignment. If submillimeter and millimeter sized grains are settled in the midplane of the disk, gas density is so high that grain alignment with the magnetic field is difficult to achieve due to gaseous dampening even when unusually strong magnetic fields and grains with many superparamagnetic inclusions are taken into account (Tazaki et al., 2017). While ∼mm

sized grains do tend to be well settled in the midplane for Class II disks (Pinte et al., 2016; Guilloteau et al., 2016), the same is not necessarily true for less evolved Class 0 disks, where grains have grown to millimeter sizes but not yet settled to the midplane (Yang et al., 2017). The Class 0 disk HH212 has resolved, geometrically-thick vertical disk structure in ALMA 850 μm data (Lee et al., 2017). The vertical structure of L1527 is also resolved by ALMA and geometrically-thick at $\sim$0.8 mm (Sakai et al., 2017). The $\sim$mm sized grains further from the midplane in these Class 0 disks will be in a less dense gaseous environment and alignment of grains perpendicular to a toroidal disk magnetic field may still be possible. Polarized emission has been detected towards Class 0 protostars L1527 and IRAS 16293-2422 B at 1.3 mm and 878 μm wavelengths respectively (Segura-Cox et al., 2015; Rao et al., 2014), tracing grain sizes similar to the grains not yet settled in the midplanes of Class 0 disks L1527 and HH212. Indeed, if the polarization mechanism in L1527 and IRAS 16293-2422 B is assumed to be purely due to magnetic field alignment, the inferred magnetic field morphologies from polarization in these sources are well-described by disk-wrapped toroidal magnetic fields. In short, while scattering and radiative alignment likely dominate polarized emission in evolved Class II disks (with $\sim$mm sized grains settled close to the midplane), the geometrically-thick $\sim$mm grain populations in the disks of Class 0 sources mean that for the youngest protostars polarization from magnetic fields cannot be ruled out.

Seven of our 19 candidate disks also have observations of polarized emission towards them: HH211-mms, IC348 MMS, NGC 1333 IRAS 4A, NGC 1333 IRAS 4B, NGC 1333 IRAS2A, SVS13B, and L1448 IRS3B (see Section 4.6). These sources are all Class 0 or Class 0/I protostars, young sources which may have thick disks and the potential for emission from $\sim$mm sized grains to become polarized via the magnetic field. We do assume for discussion here that the polarization is purely a signature of the magnetic field in these systems, yet we note that scattering and radiative alignment may also contribute to the polarized emission.

In Segura-Cox et al. (2015), we suggested a tentative trend of misaligned inferred magnetic field from polarization and rotation axes in Class 0 systems with disks, with the mis-

aligned orientation helping to reduce the effect of magnetic braking and grow disks with R >10 AU at early times (e.g., Joos et al., 2012). The scenario with aligned inferred magnetic fields and rotation axes would not inhibit magnetic braking effects and a smaller disk would be expected to form. Six of the seven candidate disks with polarized data have inferred magnetic fields either perpendicular or misaligned with the rotation axes of the systems. One of the candidate disks has an inferred magnetic field aligned with the rotation axis.

NGC 1333 IRAS4B has inferred magnetic fields perpendicular to the outflow, consistent with a toroidal disk-wrapped morphology for both SCUPOL and CARMA data (Matthews et al., 2009; Hull et al., 2014). L1448 IRS3B also has SCUPOL, BIMA, CARMA data (Matthews et al., 2009; Kwon et al., 2006; Hull et al., 2014) which indicate inferred magnetic fields perpendicular to the outflow, again consistent with disk-wrapped morphology. The inferred magnetic field of NGC 1333 IRAS2A from CARMA data (Hull et al., 2014) is misaligned with both the outflow and the candidate disk orientation. This orientation, while not consistent with disk-wrapped fields would inhibit magnetic braking and may assist with disk growth at early times. The inferred magnetic field morphology from polarization towards SVS13B (Hull et al., 2014) resembles an hourglass morphology (Girart et al., 2006), with the average orientation also misaligned with both the outflows and modeled candidate disk.

The inferred magnetic field morophology of HH211-mms from the SMA data near disk size scales (Lee et al., 2014) resembles with a disk-wrapped toroidal field in the northwest with poloidal field lines expected in envelopes and outflows in the southwest and southeast. The true magnetic field morphology of the SMA data on inner envelope and disk size scales is poorly determined due to lack of polarization detected across the entire protostar. The SCUPOL (Matthews et al., 2009) and CARMA (Hull et al., 2014) inferred magnetic fields are misaligned with both the HH211-mms candidate disk orientation and outflow orientation. The complicated polarization morphology in this source in particular may be partially explained by contributions from either scattering or radiative alignment, though magnetic field contributions cannot be ruled out.

NGC 1333 IRAS4A's polarization morphology was long attributed to magnetic fields, which are misaligned with the outflow of the protostar. The large-scale polarization (Girart et al., 2006), with an hourglass-shaped inferred magnetic field is unlikely to be dominated by scattering due to the column densities and small grain sizes in the envelope (Yang et al., 2016). The small-scale polarized emission from NGC 1333 IRAS4A (Cox et al., 2015) was found to be consistent with a mix of scattering and a toroidal magnetic field wrapped by the disk (Yang et al., 2016). Nevertheless, a magnetic field causing the polarized emission cannot be ruled out even on small scales. If we do interpret the polarization as caused magnetic fields, the fields are consistent with large scale vertical-poloidal hourglass fields misaligned with the rotation axis of the disk, transitioning to small scale frozen-in disk-wrapped toroidal fields in the magnetized disk (Hennebelle & Ciardi, 2009; Kataoka et al., 2012). As material infalls from the envelope to an embedded disk, frozen-in magnetic field lines will be drawn inwards as well, changing the magnetic field morphology between the envelope and disk (Li et al., 2014). In the case of NGC 1333 IRAS 4A, the inferred magnetic field from polarization on small scales is congruent with the idea that misaligned magnetic fields and rotation axes do not inhibit disk growth by magnetic braking in the same way as the aligned scenario.

Conversely to this idea, IC348 MMS is the only candidate disk in our sample with an aligned magnetic field and disk rotation axis, emphasizing that while misaligned systems in Class 0 protostars may act as indicators of disks on small scales, misalignment is not a requirement for disk formation. The inferred magnetic field orientation of IC348 MMS from VANDAM 8 mm continuum polarization (Cox et al. in preparation) is parallel to the outflows and perpendicular to the orientation of the modeled 8 mm candidate disk (R$\sim$25 AU). This is contrary to the idea that disks with aligned magnetic fields and rotation axes (as traced by outflows) will be limited to sizes <10 AU as predicted by magnetic braking models (Joos et al., 2012; Dapp & Basu, 2010), since we have an aligned orientation with a rather large disk for this scenario. However, we note that the inclination angle of IC348 MMS is 44°, similar to the moderately inclined NGC 1333 IRAS4A. Like NGC 1333 IRAS4A,

the inferred magnetic field morphology of a moderately inclined disk like IC348 MMS may transition from a poloidal hourglass morphology at large scales (Girart et al., 2006) to a disk-wrapped toroidal morphology at smaller scales (Cox et al., 2015). The VANDAM 8 mm continuum polarization of IC348 MMS (∼65 AU resolution; Cox et al. in preparation) may not trace size scales small enough to detect a disk-wrapped component of the magnetic field, since the L1527 inferred toroidal disk-wrapped magnetic field was detected on ∼50 AU scales (Segura-Cox et al., 2015). With the current observations it is also unclear what role scattering and radiative alignment play in the polarization observations, with multiple processes possibly playing a role in IC348 MMS, as was the case in NGC 1333 IRAS4A (Yang et al., 2016).

Nonetheless, the inferred magnetic field morphologies from polarization for six of the seven polarized VANDAM candidate disks are consistent with the scenario of perpendicular or misaligned inferred magnetic field orientations compared to the rotation axes of the systems, inhibiting magnetic braking and allowing the disks to grow larger than 10 AU at early times (Hennebelle & Ciardi, 2009; Joos et al., 2012; Li et al., 2013; Krumholz et al., 2013). This tentative trend of misalignment between inferred magnetic fields and outflows in Class 0 sources with disks can be strengthened with previous observations of sources outside the Perseus molecular cloud. In Table 2.2 in Chapter 2, the Class 0 sources L1527, IRAS 16293-2422 B, and VLA 1623 also have perpendicular inferred magnetic fields from polarization and outflows with strong evidence of embedded disks (Segura-Cox et al., 2015). Combined this brings the total of known and candidate Class 0 disks with misaligned outflow and inferred magnetic field orientations to nine sources, double the number of to-date Keplerian-confirmed Class 0 disks. Misalignment between inferred magnetic fields on envelope scales and outflows may indeed be a signpost of disks on smaller scales in Class 0 sources with geometrically-thick disks. IC348 MMS, the candidate disk with the aligned scenario, indicates that misalignment may assist with disk growth at early times but is certainly not a requirement to form disks.

4.8 Summary of VANDAM Disk Candidate Results

With the 12 AU resolution VANDAM survey, we find a total of 19 Class 0 and I candidate disks the Perseus molecular cloud, more than doubling the number of known Class 0 and I disks to-date, bringing the total count from ∼15 to ∼34. We were able to model 15 of the 19 candidate disks because four are highly asymmetrical and not fit well by our disk model. Because we do not have small-scale kinematic data to confirm that these are rotationally supported disks, we refer to the VANDAM sources as disk candidates.

We fit the deprojected, azimuthally averaged, and radially binned VLA 8 mm continuum data in u,v-space to a disk-shaped profile to determine disk candidacy of the extended sources and to begin to model disk properties. We fix the inclination and position angles of the disks using estimates from the image-plane. We take into account a point-source component to account for free-free emission from the jet-launching regions of the disks. NGC 1333 IRAS 4A and NGC 133 IRAS 4B have obvious envelope contamination in both the image and u,v-planes. We apply a taper to the data to account for this in the image plane and do not fit the corresponding removed inner baselines to the disk profile in u,v-space. Other sources have minimal envelope contamination. Except for sources with envelope contamination or small asymmetric features, the residuals from subtracting the model from the data are empty. For all but one candidate disk, the major axis of the disk is roughly perpendicular to the outflow axis (a proxy for the rotation axis), as expected for rotating protostellar disks.

35% of Class 0 (and Class 0/I) protostars and just 11% of Class I protostars have candidate disks larger than the 8 mm VLA 12 AU resolution data in Perseus. There is a mild trend that more evolved sources, as gauged by T_{bol}, have higher values of γ for the 8 mm data; older sources appear to have more centrally concentrated 8 mm dust grain populations. This may be due to the 8 mm grains in older sources having more time to undergo radial drift towards the central protostar than younger sources, resulting in a steeper inner-disk surface density power law (γ) for more evolved sources. Additionally, the two largest candi-

date disks belong to Class 0 protostars. 76% of Class 0 and I protostars do not have signs of disks within our 12 AU resolution limit; at 8 mm most disks in the Class 0 and I phases are small (<10 AU).

Our estimated masses of the candidate disks are large compared to masses of known Class 0 and Class I disks, indicating that our assumed value of dust opacity spectral index $\beta = 1$ is too large. Most disks have best-fit models with q <0.5, typical for embedded disks. Values of γ are lower and more shallow for Class 0 and I candidate disks than in Class II disks, indicating that evolved disks are generally more centrally concentrated than our Class 0 and I disks. Modeled radii of the candidate disks are somewhat large at 8 mm and comparable to known Class 0 disk radii known from kinematics at ∼mm wavelengths. Per-emb-14 has a ∼3× larger disk at 1.3 mm with a smaller grain population, evidence that our 8 mm data is a lower limit on true disk radius. Since our 8 mm data trace a population of larger dust grains which radially drift towards the protostar and are lower limits on true disk size, large disks at early times do not seem to be particularly rare.

Seven of the 19 candidate disk sources also have polarization detections. In the extreme case of ignoring scattering and radiative alignment, which may contribute to polarized emission but do not preclude magnetic fields contributing to the polarization signal in geometrically-thick Class 0 disks, six of the seven candidate disks with polarized emission have inferred magnetic field morphologies misaligned with the outflows/rotation axes of the systems. The only candidate disk that fully breaks this trend is IC348 MMS, which only has aligned inferred magnetic fields and outflows, yet has a relatively large disk for this scenario. The polarization of IC348 MMS indicates that while misalignment may assist with disk growth at early times, it is certainly not a requirement to form disks; it is possible that the polarized emission from IC348 MMS is not tracing magnetic field lines. Three additional Class 0 disks from other molecular clouds have misaligned inferred magnetic field and outflow directions, bringing the total number to nine. Misalignment between inferred magnetic fields on envelope scales and outflows may be used in the future as indirect evidence of possible

geometrically-thick disks on smaller scales in Class 0 protostars.

This research made use of APLpy, an open-source plotting package for Python hosted at http://aplpy.github.com.

The National Radio Astronomy Observatory is a facility of the National Science Foundation operated under cooperative agreement by Associated Universities, Inc.

4.9 Best-Fit Candidate Disk Modeling Results in Image and u,v-Spaces

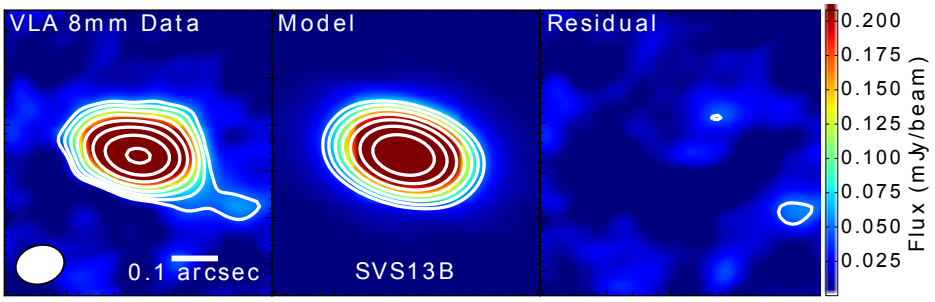

Figure 4.7: VLA A+B array data (left), $q = 1.0$ model from u,v-plane best-fit (center), and residual (right) of SVS13B. Images were produced with robust = 0.25 weighting. Contours start at 3σ ($\sigma \sim 15\mu$Jy) with a factor of $\sqrt{2}$ spacing. The synthesized beam is in the lower left.

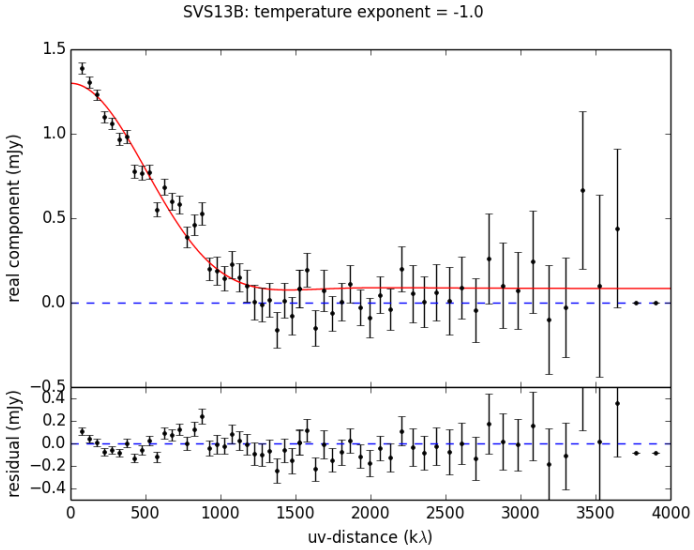

Figure 4.8: Real vs u,v-distance plot of 8 mm data for SVS13B. Top: real component of data. The blue dashed line indicates real component of zero. The red solid line is the best-fit model. Bottom: residual of real component minus model.

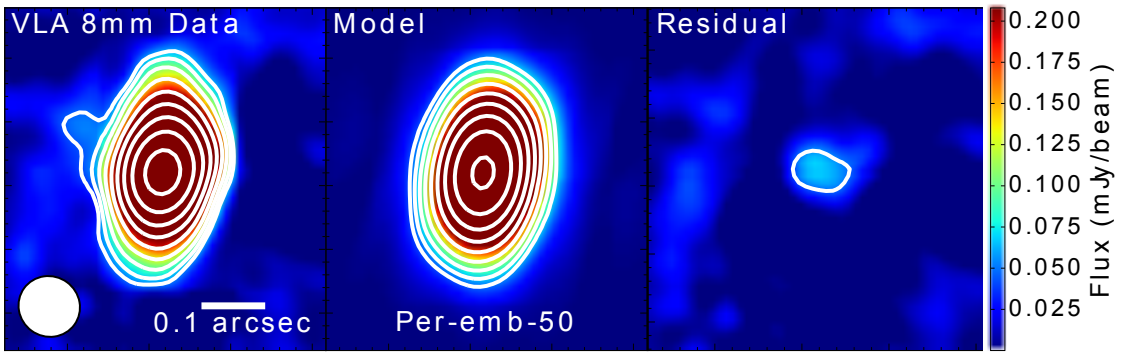

Figure 4.9: Same as Figure 4.7, for Per-emb-50, with $q = 0.25$.

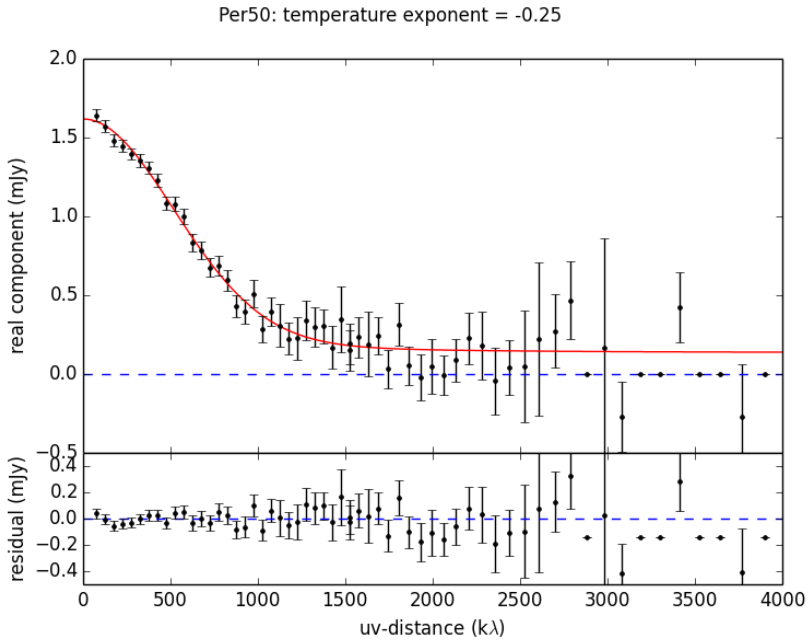

Figure 4.10: Same as Figure 4.8, for Per-emb-50.

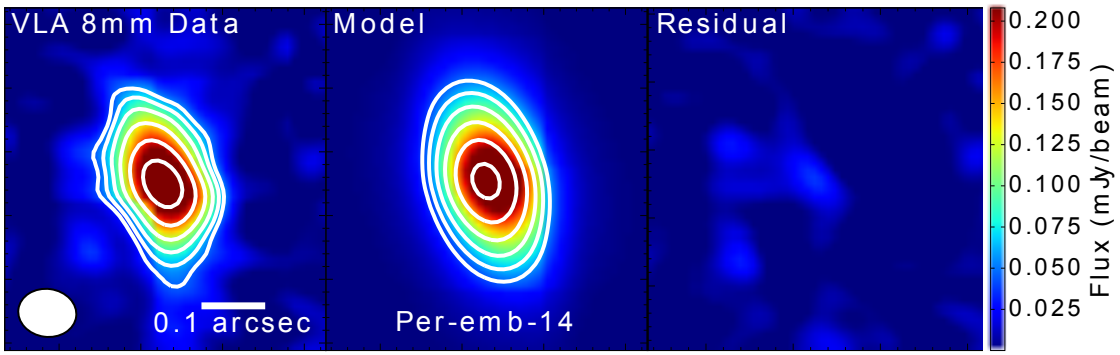

Figure 4.11: Same as Figure 4.7, for Per-emb-14, with $q = 0.25$.

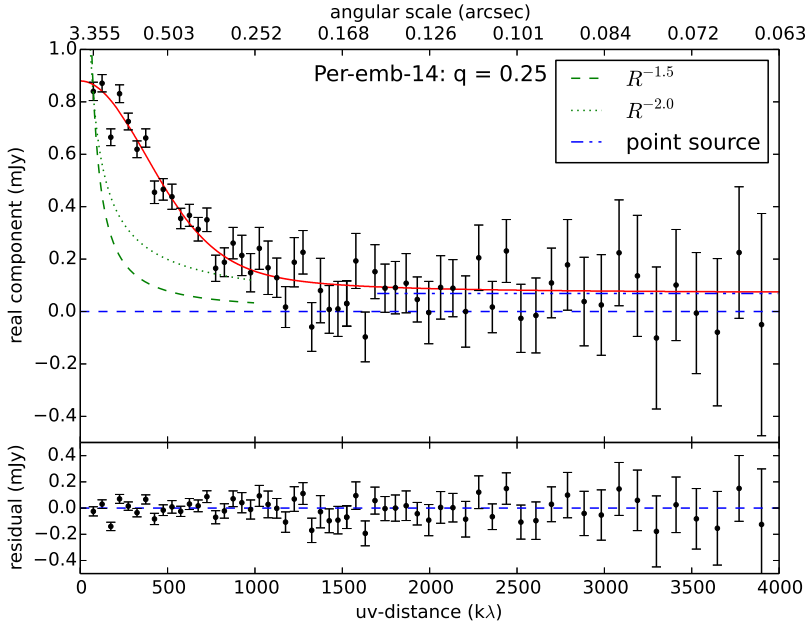

Figure 4.12: Same as Figure 4.8, for Per-emb-14.

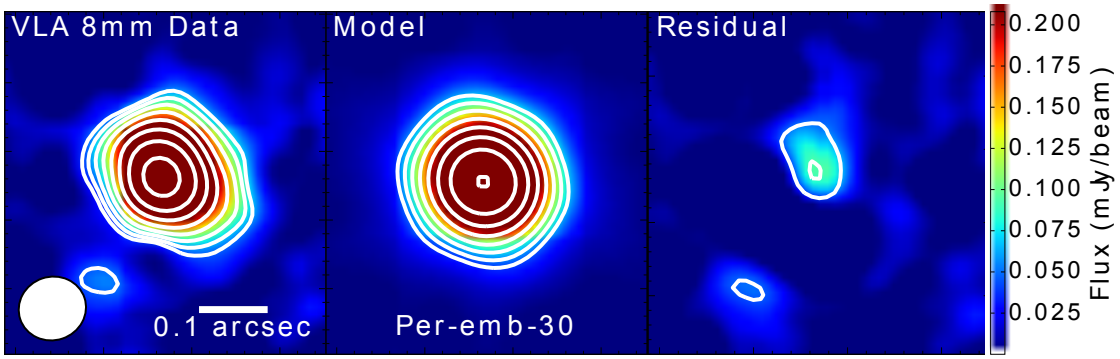

Figure 4.13: Same as Figure 4.7, for Per-emb-30, with $q = 0.25$.

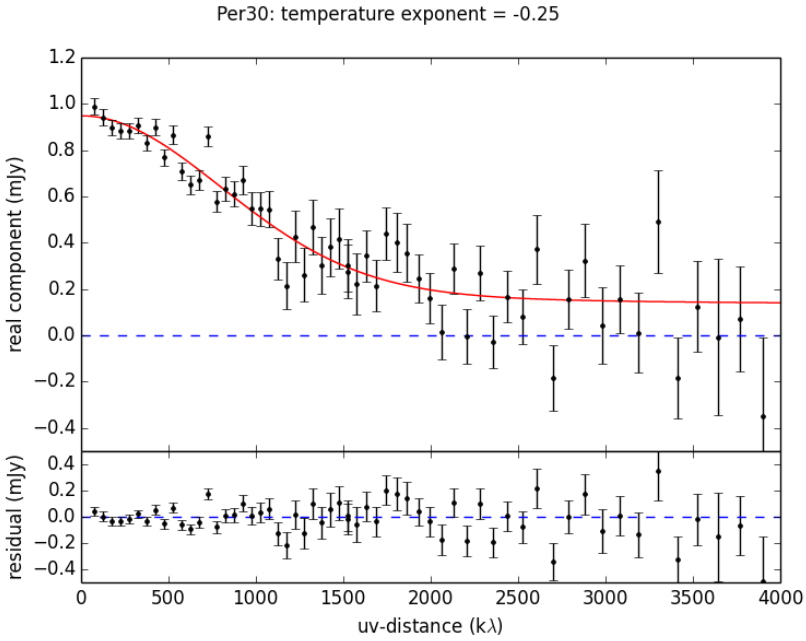

Figure 4.14: Same as Figure 4.8, for Per-emb-30.

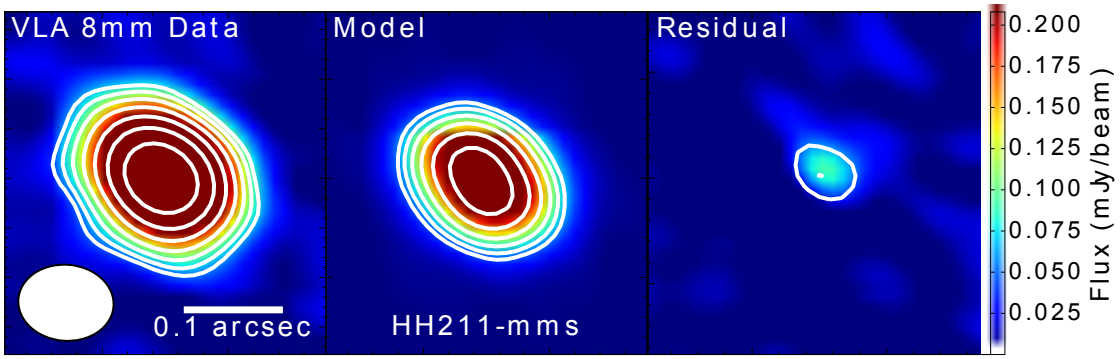

Figure 4.15: Same as Figure 4.7, for HH211-mms, with $q = 0.25$.

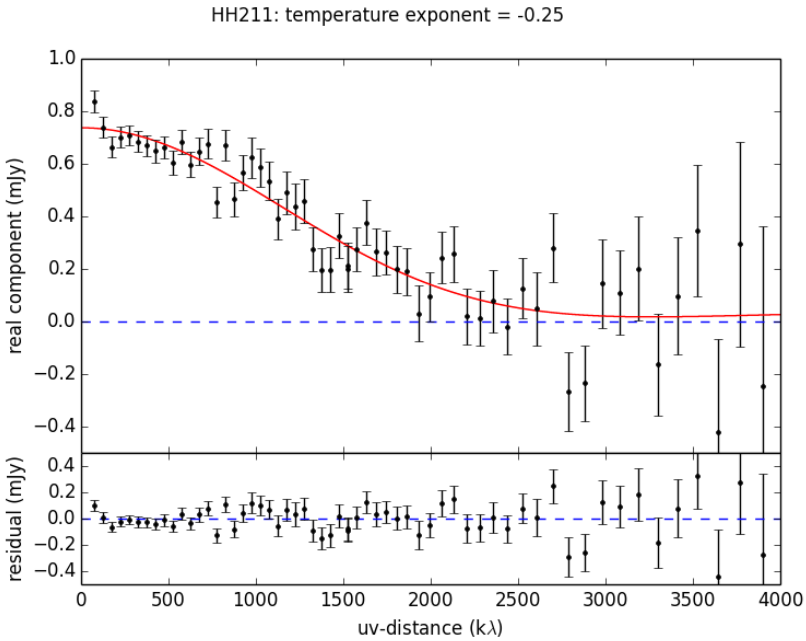

Figure 4.16: Same as Figure 4.8, for HH211-mms.

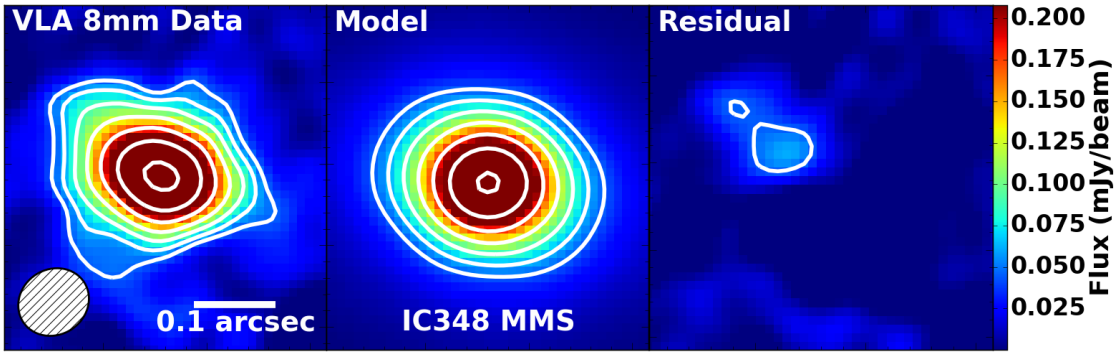

Figure 4.17: Same as Figure 4.7, for IC348 MMS, with $q = 0.25$.

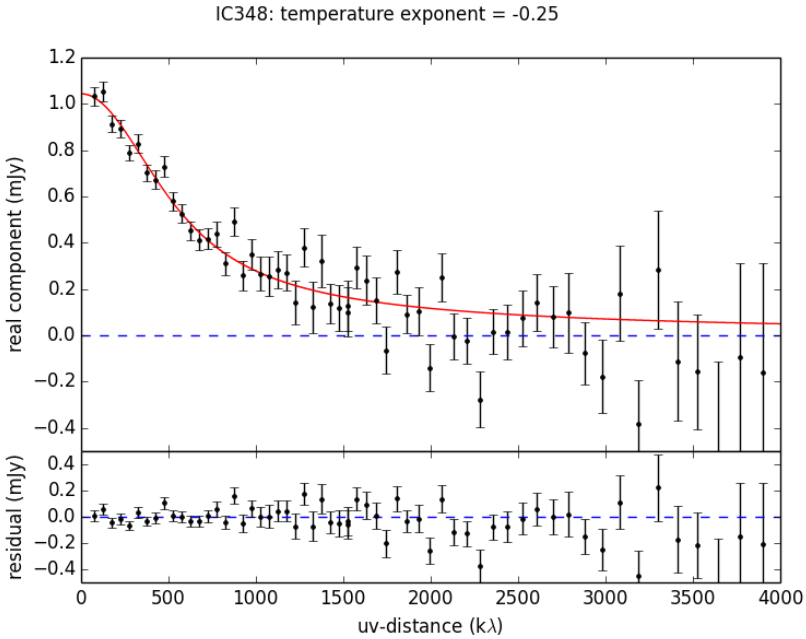

Figure 4.18: Same as Figure 4.8, for IC348 MMS.

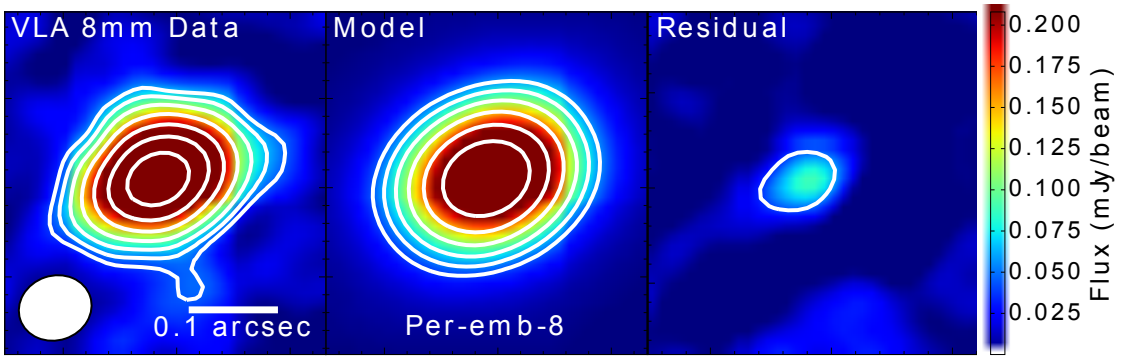

Figure 4.19: Same as Figure 4.7, for Per-emb-8, with $q = 0.25$.

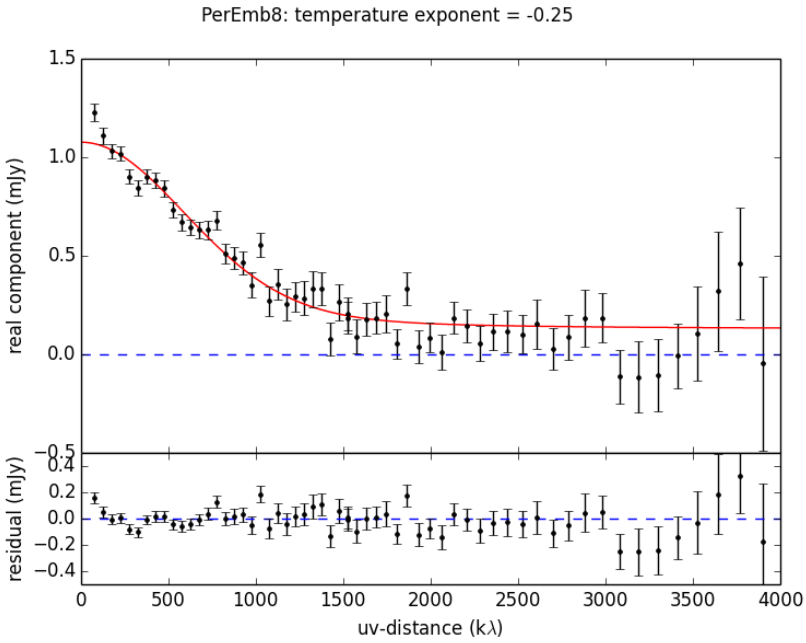

Figure 4.20: Same as Figure 4.8, for Per-emb-8.

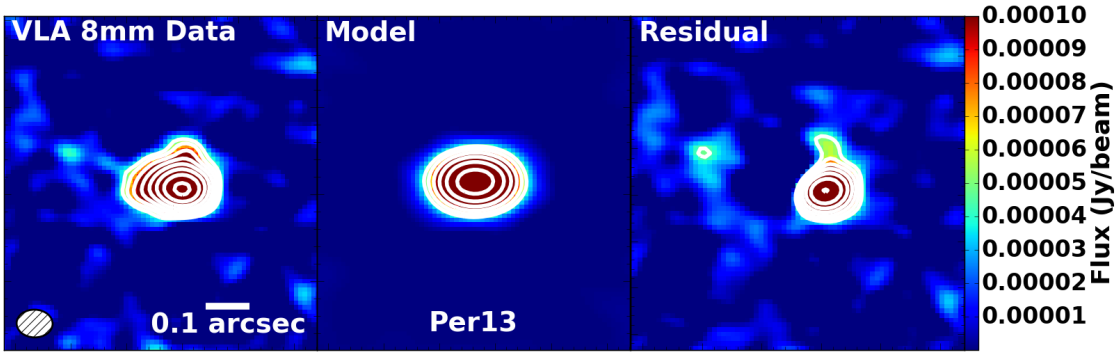

Figure 4.21: Same as Figure 4.7, for NGC 1333 IRAS4B, with $q = 0.25$ and baselines <350 kλ removed.

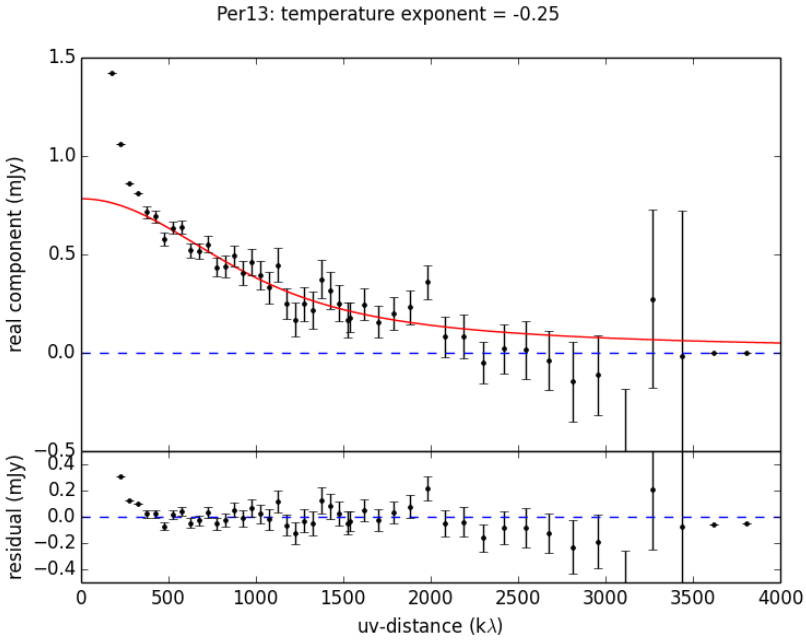

Figure 4.22: Same as Figure 4.8, for NGC 1333 IRAS4B. The baselines <350 kλ are not fit to the disk component.

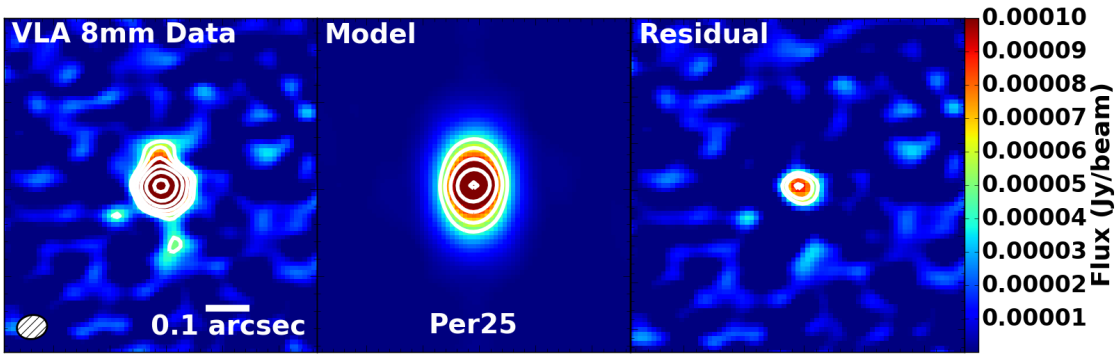

Figure 4.23: Same as Figure 4.7, for Per-emb-25, with $q = 0.25$.

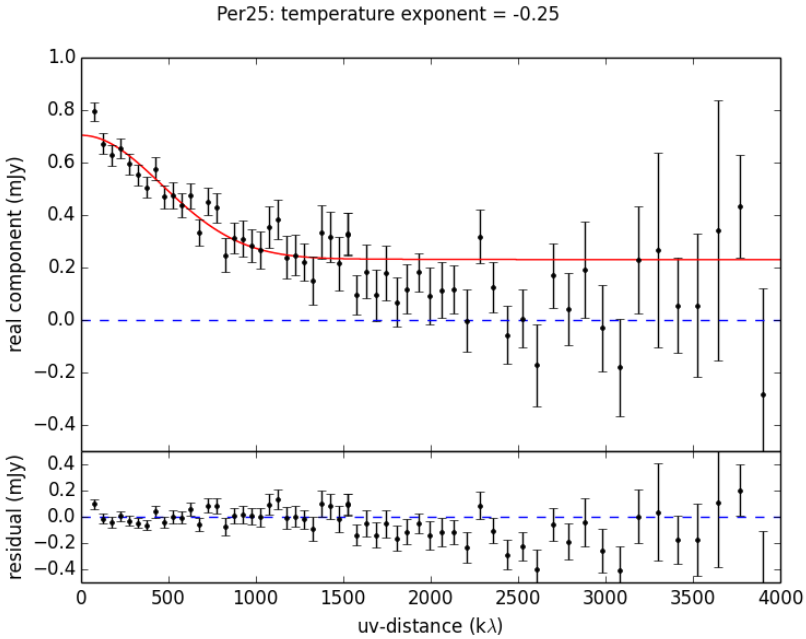

Figure 4.24: Same as Figure 4.8, for Per-emb-25.

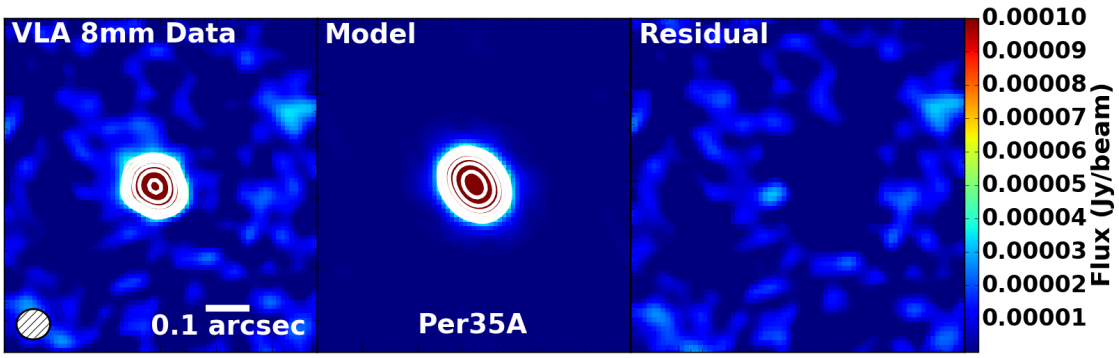

Figure 4.25: Same as Figure 4.7, for NGC 1333 IRAS1 A, with $q = 0.25$.

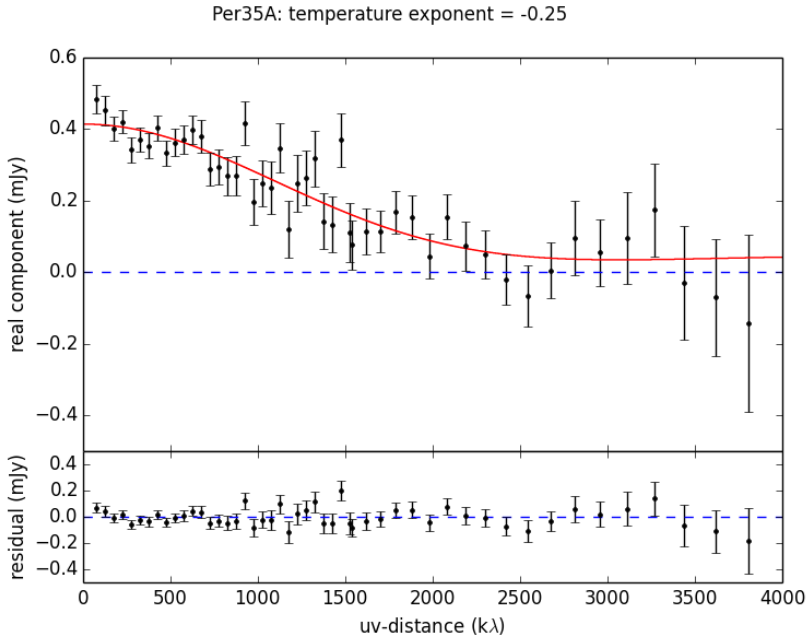

Figure 4.26: Same as Figure 4.8, for NGC 1333 IRAS1 A.

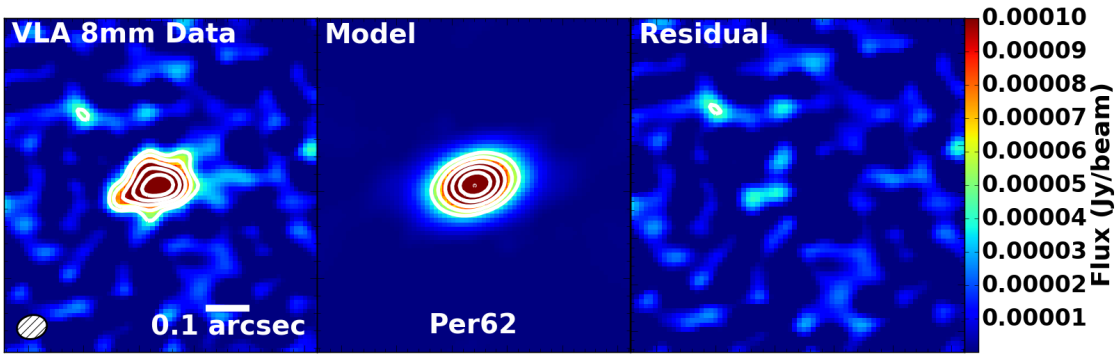

Figure 4.27: Same as Figure 4.7, for Per-emb-62, with $q = 1.0$.

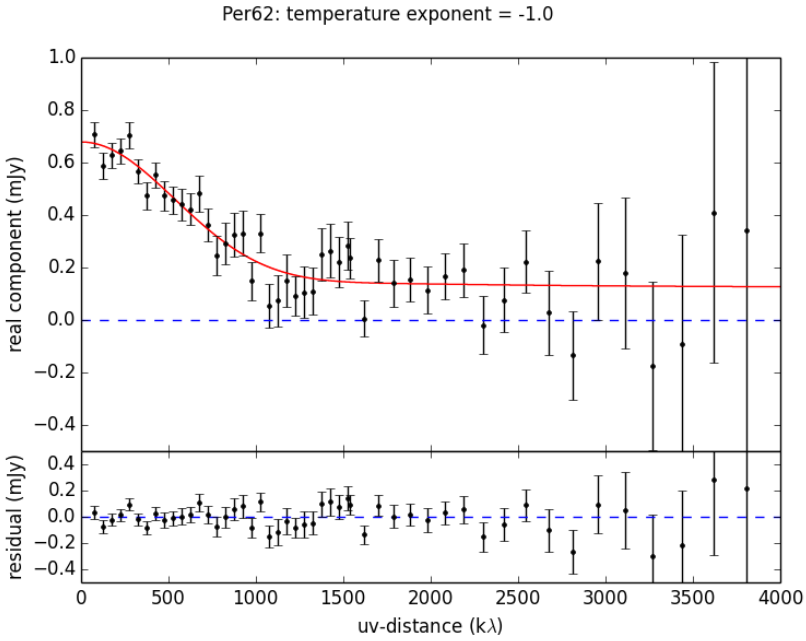

Figure 4.28: Same as Figure 4.8, for Per-emb-62.

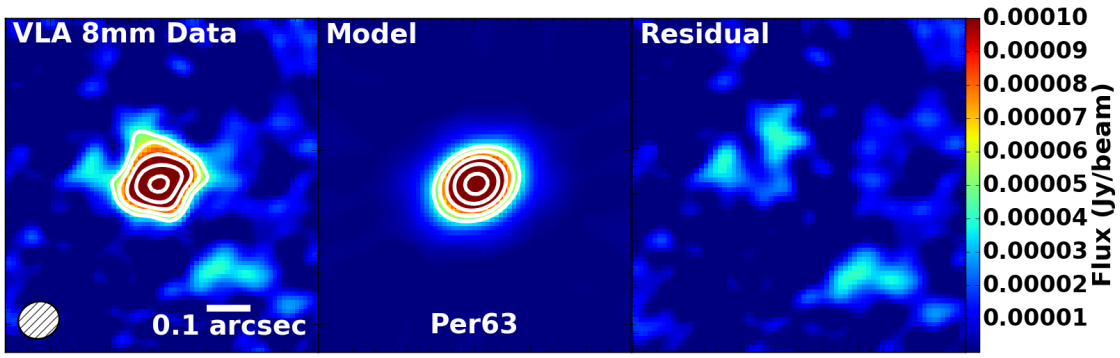

Figure 4.29: Same as Figure 4.7, for Per-emb-63, with $q = 0.25$.

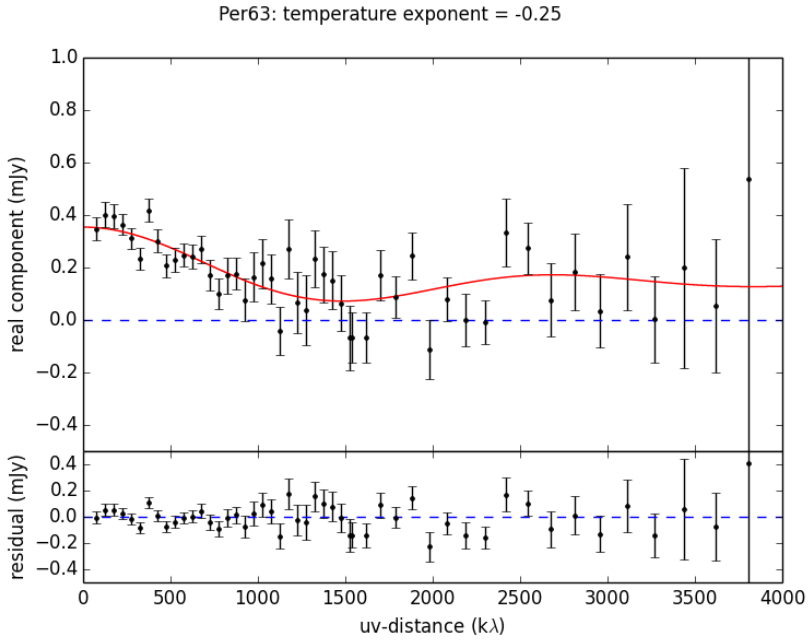

Figure 4.30: Same as Figure 4.8, for Per-emb-63.

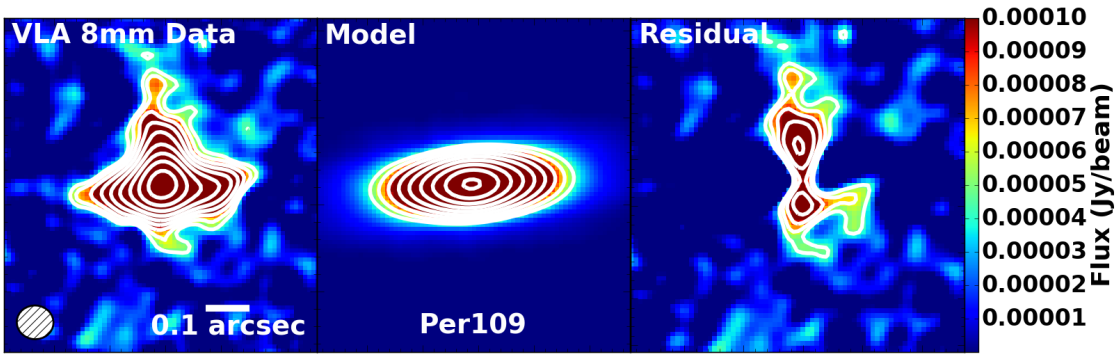

Figure 4.31: Same as Figure 4.7, for SVS13C, with $q = 0.25$.

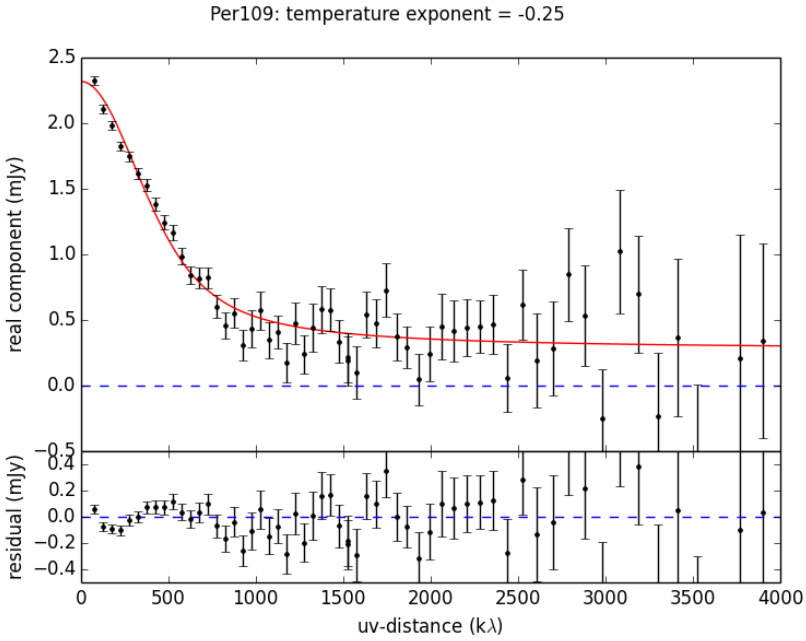

Figure 4.32: Same as Figure 4.8, for SVS13C.

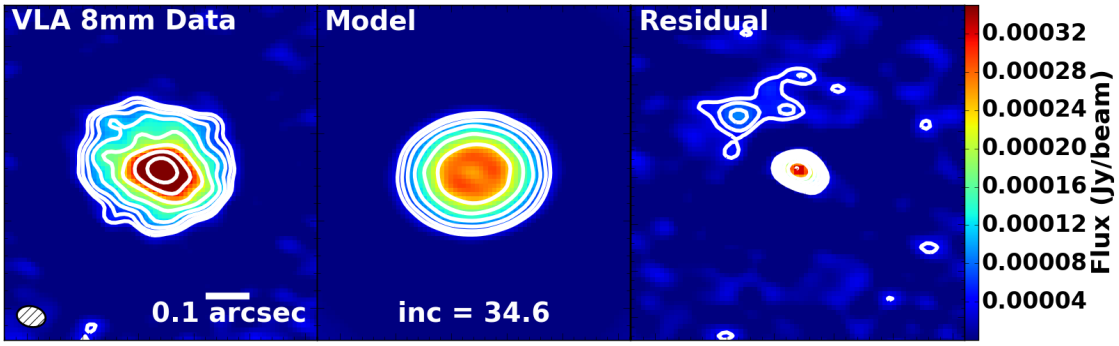

Figure 4.33: Same as Figure 4.7, for NGC 1333 IRAS4A, with $q = 0.25$ and baselines <350 kλ removed.

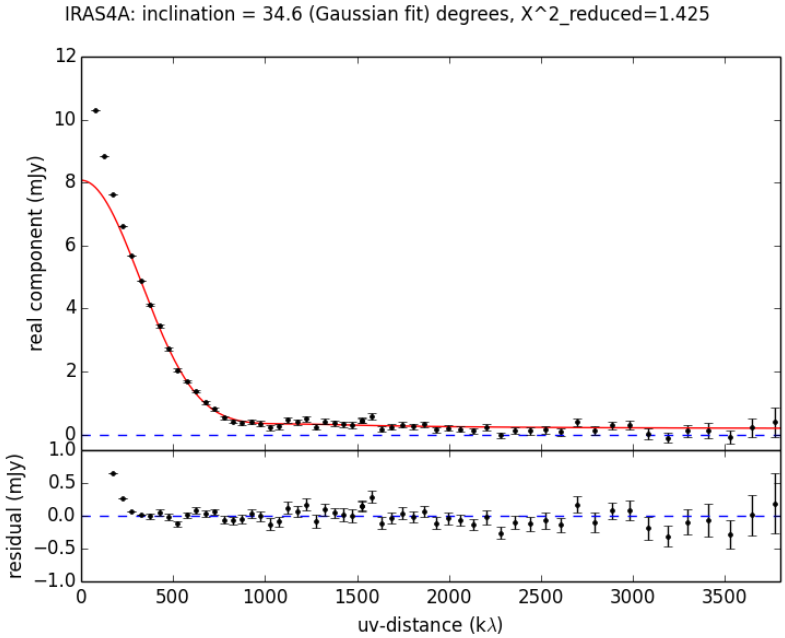

Figure 4.34: Same as Figure 4.8, for NGC 1333 IRAS4A. The baselines <350 kλ are not fit to the disk component.

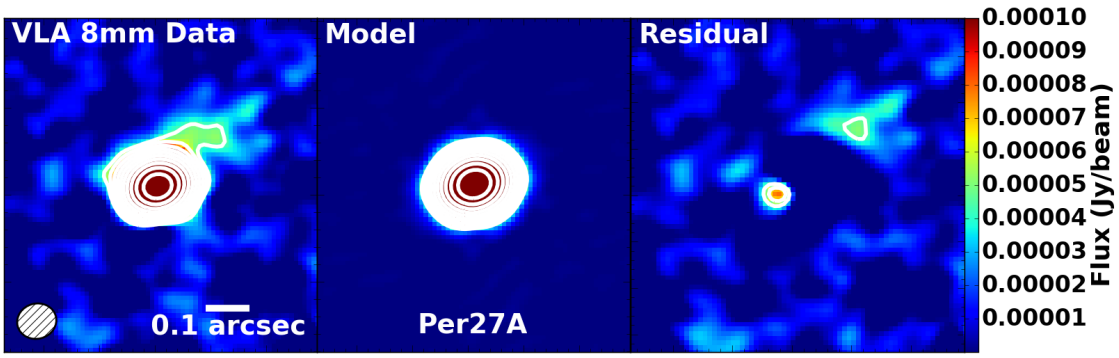

Figure 4.35: Same as Figure 4.7, for NGC 1333 IRAS2A, with $q = 0.25$.

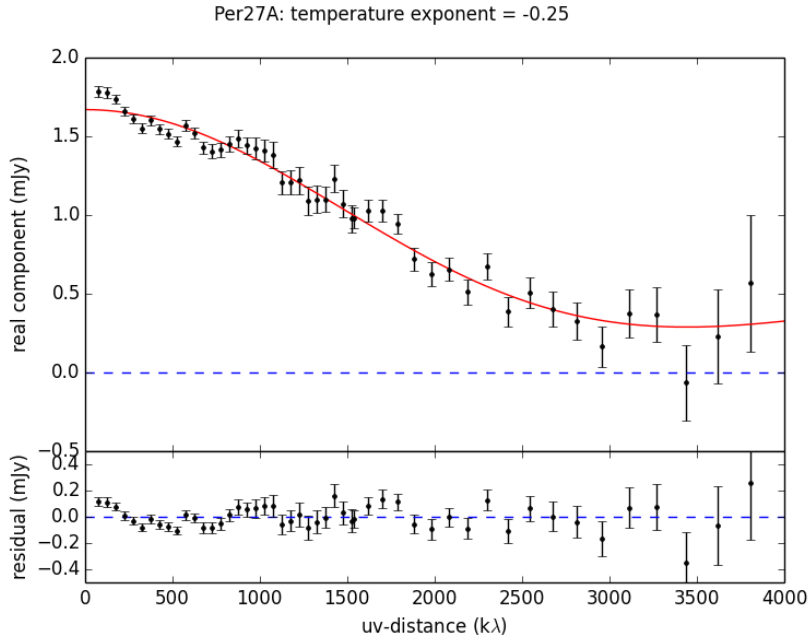

Figure 4.36: Same as Figure 4.8, for NGC 1333 IRAS2A.

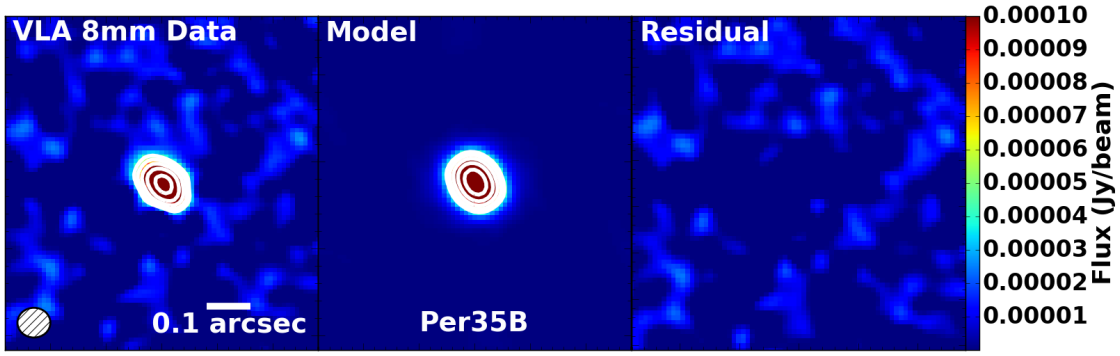

Figure 4.37: Same as Figure 4.7, for NGC 1333 IRAS1 B, with $q = 0.5$. We do not consider this source a candidate disk.

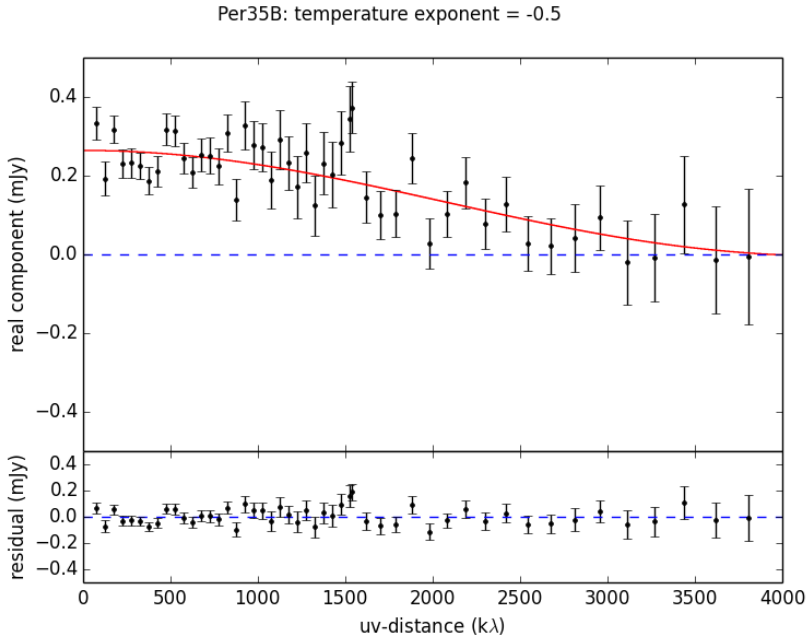

Figure 4.38: Same as Figure 4.8, for NGC 1333 IRAS1 B. We do not consider this source a candidate disk.

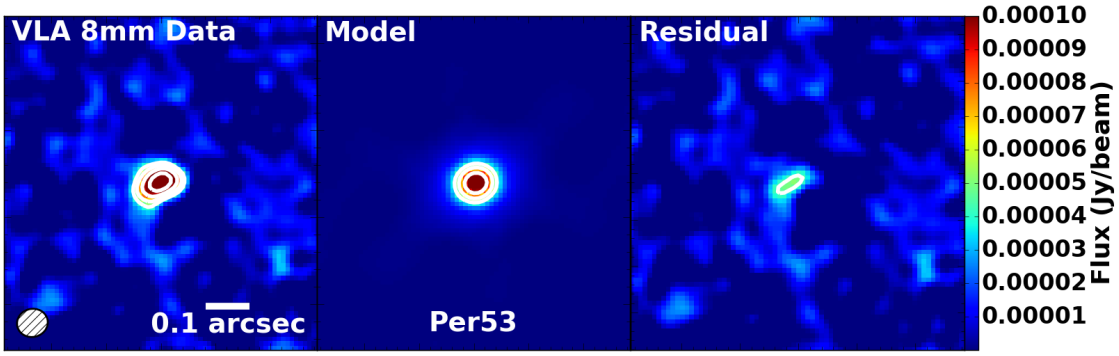

Figure 4.39: Same as Figure 4.7, for B5-IRS1, with $q = 1.0$. We do not consider this source a candidate disk.

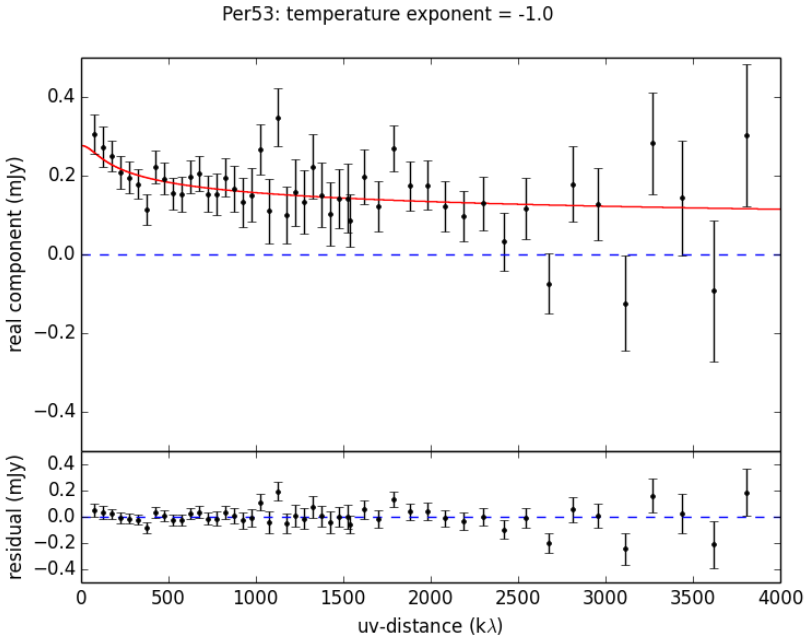

Figure 4.40: Same as Figure 4.8, for B5-IRS1. We do not consider this source a candidate disk.

4.10 Using Gaussian IMFIT Results from the Image Plane for Inclination Estimates

Table 4.4: Results of Varying Inclination for Modeling NGC 1333 IRAS4A

inclination	q	R_c (AU)	γ	$\chi^2_{\rm reduced}$
0° (face on)	1.0	$38.48^{+0.78}_{-0.71}$	$0.68^{+0.02}_{-0.02}$	2.132
5°	1.0	$38.55^{+0.76}_{-0.74}$	$0.68^{+0.02}_{-0.03}$	2.074
10°	1.0	$38.64^{+0.83}_{-0.70}$	$0.69^{+0.03}_{-0.02}$	2.025
15°	1.0	$39.22^{+0.81}_{-0.77}$	$0.68^{+0.02}_{-0.03}$	1.816
20°	1.0	$39.54^{+0.80}_{-0.72}$	$0.69^{+0.02}_{-0.03}$	1.897
25°	1.0	$40.46^{+0.86}_{-0.80}$	$0.69^{+0.03}_{-0.02}$	1.765
30°	1.0	$41.31^{+0.95}_{-0.86}$	$0.69^{+0.03}_{-0.02}$	1.507
34.6° (Gaussian fit)	1.0	$42.23^{+0.99}_{-0.89}$	$0.69^{+0.03}_{-0.02}$	1.535
35°	1.0	$42.25^{+0.97}_{-0.92}$	$0.69^{+0.03}_{-0.02}$	1.700
40°	1.0	$42.67^{+1.08}_{-0.97}$	$0.69^{+0.03}_{-0.03}$	1.771
45°	1.0	$44.48^{+1.22}_{-1.04}$	$0.68^{+0.03}_{-0.02}$	1.652
50°	1.0	$45.06^{+1.37}_{-1.27}$	$0.66^{+0.02}_{-0.03}$	1.382
55°	1.0	$45.01^{+1.70}_{-1.40}$	$0.64^{+0.03}_{-0.04}$	1.635
60°	1.0	$43.77^{+2.00}_{-1.62}$	$0.64^{+0.04}_{-0.03}$	1.450
65°	1.0	$40.48^{+2.13}_{-1.57}$	$0.67^{+0.05}_{-0.05}$	1.541
70°	1.0	$37.70^{+1.77}_{-1.36}$	$0.72^{+0.05}_{-0.06}$	1.319
75°	1.0	$38.46^{+1.64}_{-1.50}$	$0.74^{+0.06}_{-0.05}$	1.412
80°	1.0	$38.23^{+1.67}_{-1.49}$	$0.74^{+0.06}_{-0.06}$	1.495
85°	1.0	$38.80^{+1.61}_{-1.45}$	$0.74^{+0.05}_{-0.06}$	1.411

Values of q are fixed. Values of γ and R_c are determined from best-fit models. Uncertainties reflect 90% confidence intervals.

To measure inclination angles of the candidate disks, which are fixed in our models, we fit a 2D Gaussian to our data in the image plane with the CASA task IMFIT. IMFIT is

best suited for surface brightness distributions which are Gaussian; any protostellar disks present in our sample will have a non-Gaussian profile. Here we show that using IMFIT's 2D Gaussian estimate for the major and minor axis of the disk is a valid way to estimate the inclination angle of the disk candidates.

To demonstrate the usefulness of IMFIT in estimating inclination angles for these non-gaussian disk candidates, we have modeled a disk component for NGC 1333 IRAS4A in steps of 5° inclination angles in the u,v-plane. NGC 1333 IRAS4A is by far the brightest source, with the highest signal-to-noise level. For imaging, we remove the shortest (<350 kλ) baselines, corresponding to large-scale emission, to remove the envelope contamination from the source and reveal the disk component. This does not completely eliminate the envelope emission, but it removes enough to allow us to model a disk-only component.

From the table, the $\chi^2_{reduced}$ values have a local minimum near 35°, but there are more minima later, at >50°. Here we note that it is important to examine the image plane in addition to the u,v-plane modeling to determine if the inclination angle has been adequately estimated. At 50°, there is a small area of residual emission to the south of the central peak where at <50° inclinations, this was not present. By 55°, the residual emission to the south is more obvious and the residuals continue to grow from there with increasing inclination. Based on this modeling, we estimate the maximum inclination angle for the disk is around 45°. This is within the 10° uncertainty on the 2D Gaussian inclination estimate, indicating that we may continue to fix the inclination angle in our models to reduce computation time and avoid over-fitting marginally resolved sources.

The value $q = 1$ is steeper than the analytic models for accretion disks which typically have $q = 0.5$ and embedded disks are likely to have a flatter q than the protoplanetary disks. There appears to be a compact residual for inclinations around 35°. The residual here is larger than the beam, which an unresolved point source would not explain. A point source component was also included in the model to compensate for any free-free emission from the central protostar as described in Section 4.4.1. An envelope component was not included in

this modeling exercise. The residual is either remaining envelope, indicates that the simple 1D disk model may not be entirely appropriate for NGC 1333 IRAS4A, or a combination of both. Residual envelope signal near the line-of-sight center of the disk may explain the steeper value of q in this source.

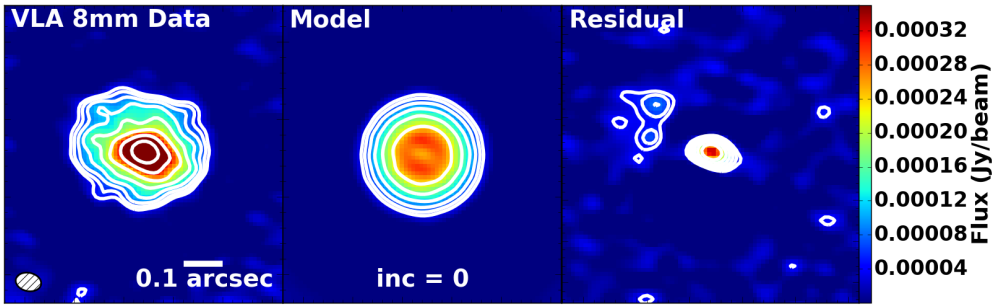

Figure 4.41: VLA A+B array data (left), $q = 0.25$ model from u,v-plane best-fit with 0° inclination (center), and residual (right), all with baselines <350 kλ removed. Images were produced with robust = 0.25 weighting. Contours start at 3σ ($\sigma \sim 15\mu$Jy) with a factor of $\sqrt{2}$ spacing. The synthesized beam is in the lower left.

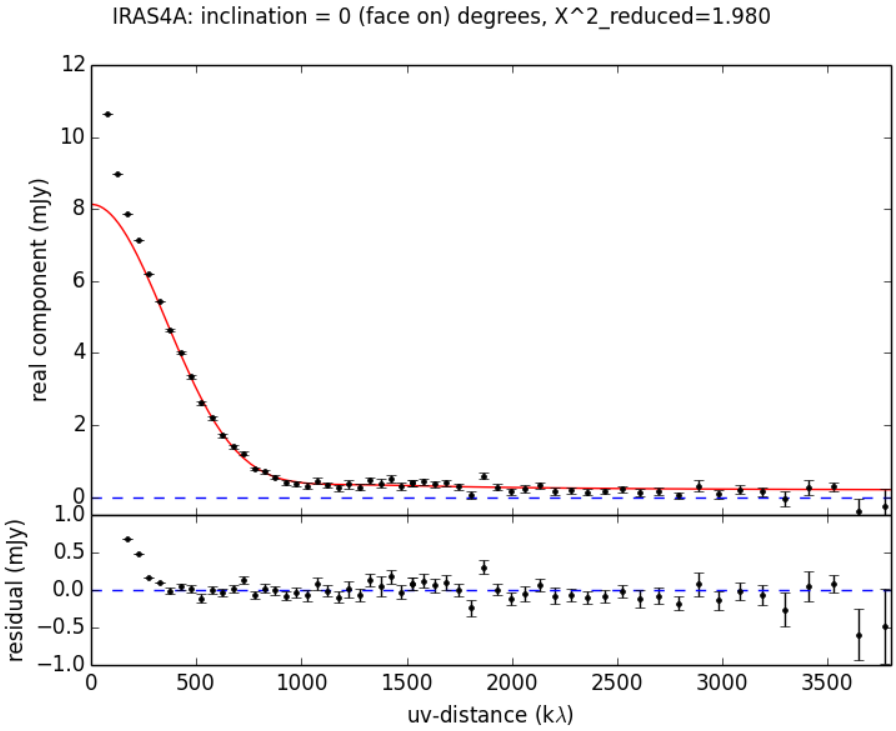

Figure 4.42: Real vs u,v-distance plot of 8 mm data. Top: real component of data. The blue dashed line indicates real component of zero. The red solid line is the best-fit model with 0° inclination. Bottom: residual of real component minus model. The baselines <350 kλ are not fit to the disk component.

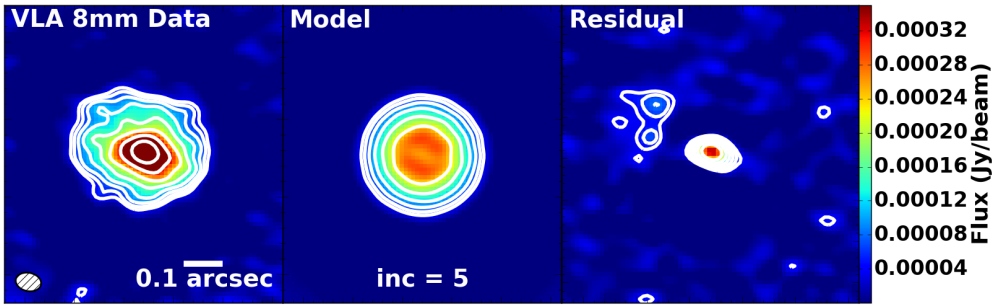

Figure 4.43: Same as Figure 4.41, for 5° inclination.

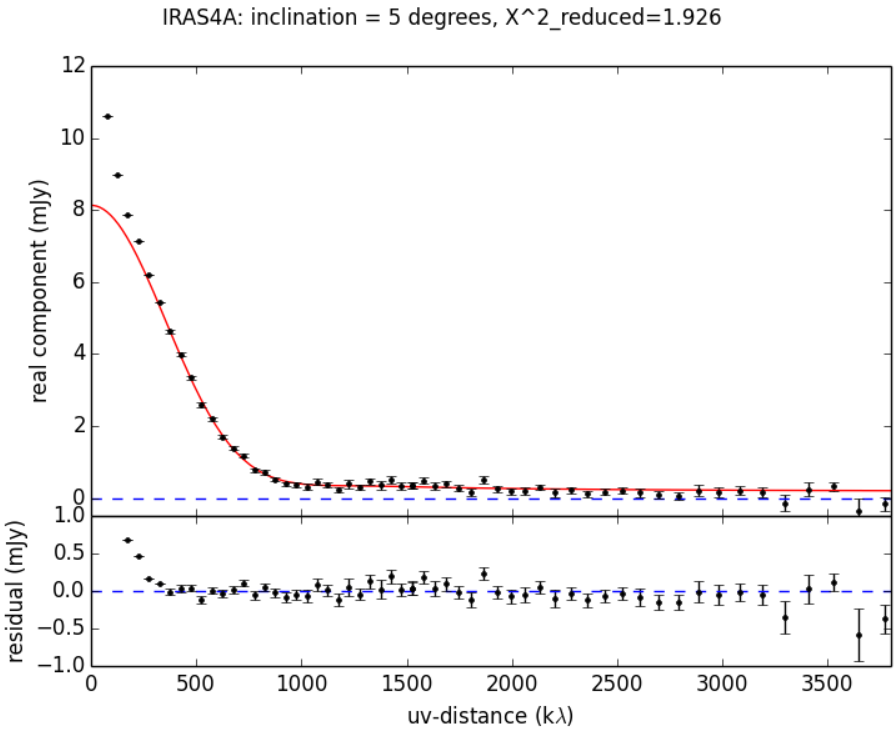

Figure 4.44: Same as Figure 4.42, for 5° inclination.

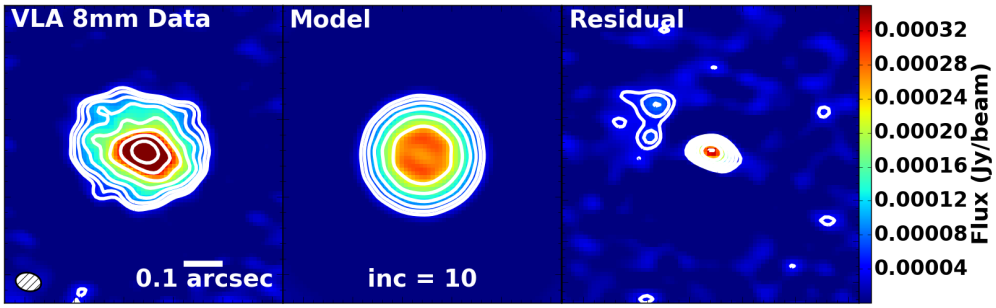

Figure 4.45: Same as Figure 4.41, for 10° inclination.

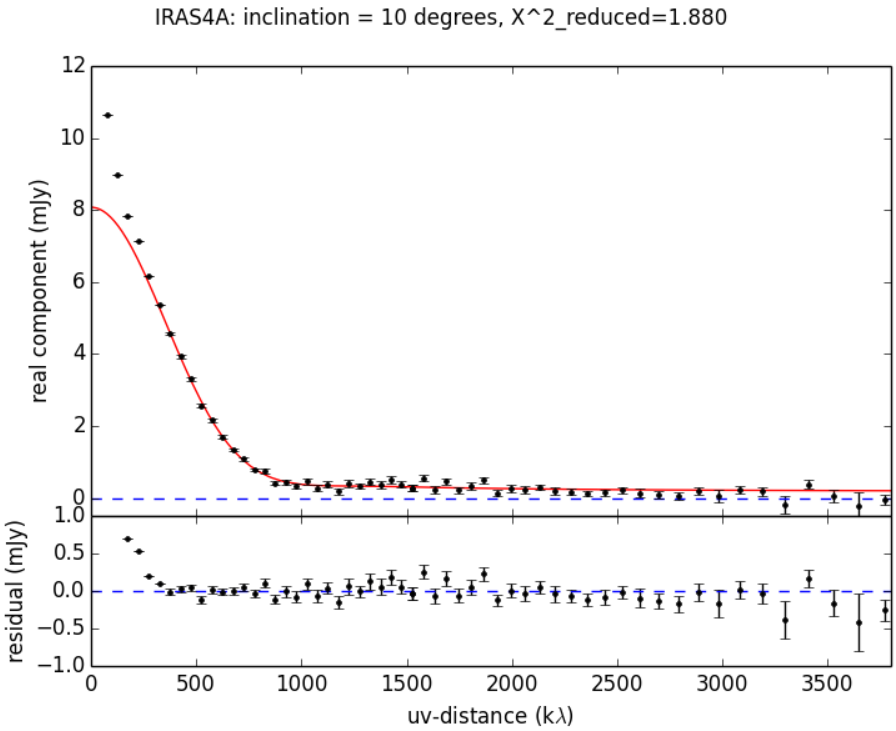

Figure 4.46: Same as Figure 4.42, for 10° inclination.

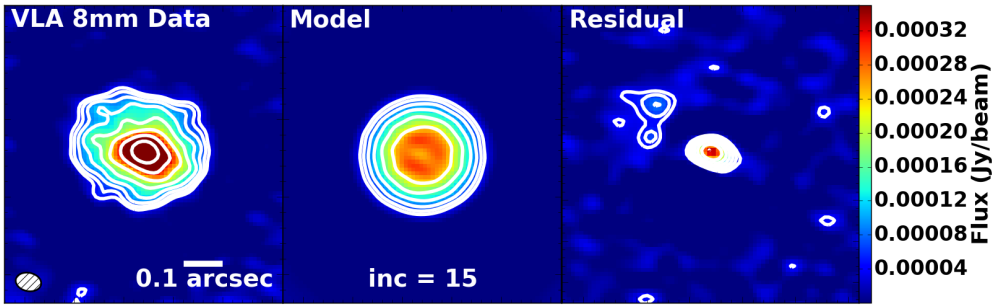

Figure 4.47: Same as Figure 4.41, for 15° inclination.

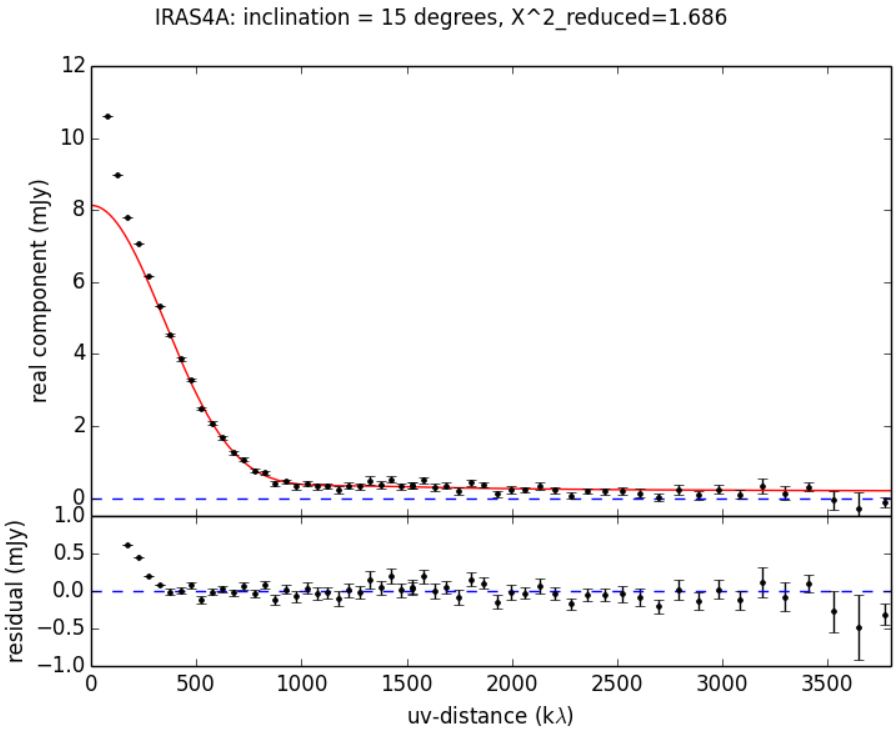

Figure 4.48: Same as Figure 4.42, for 15° inclination.

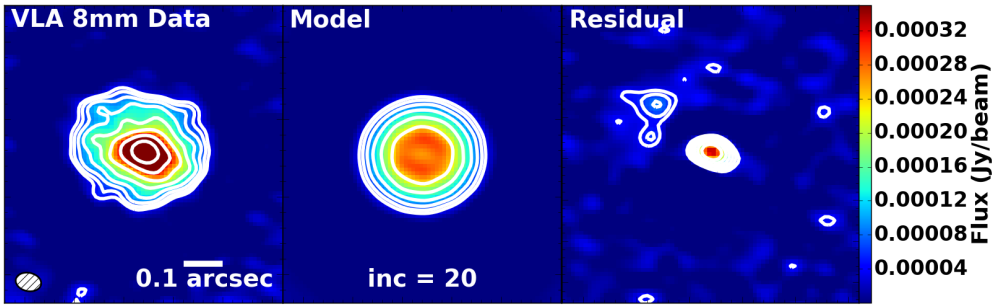

Figure 4.49: Same as Figure 4.41, for 20° inclination.

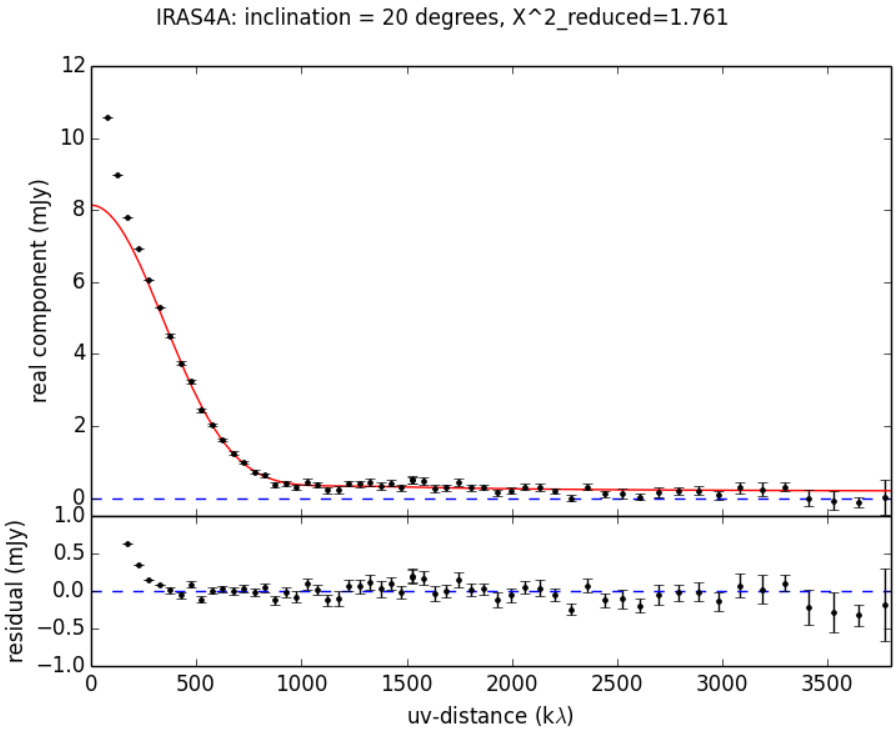

Figure 4.50: Same as Figure 4.42, for 20° inclination.

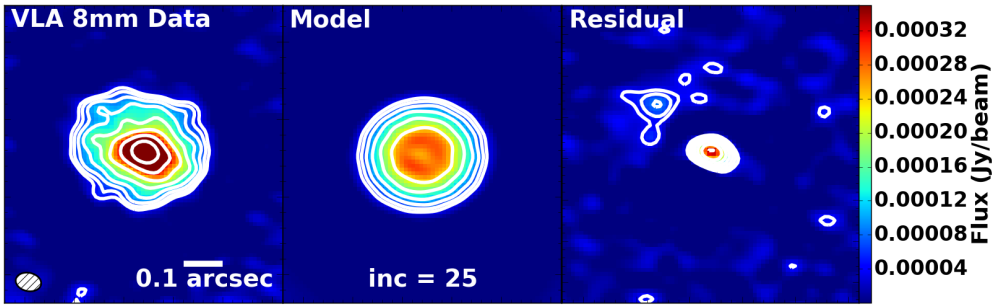

Figure 4.51: Same as Figure 4.41, for 25° inclination.

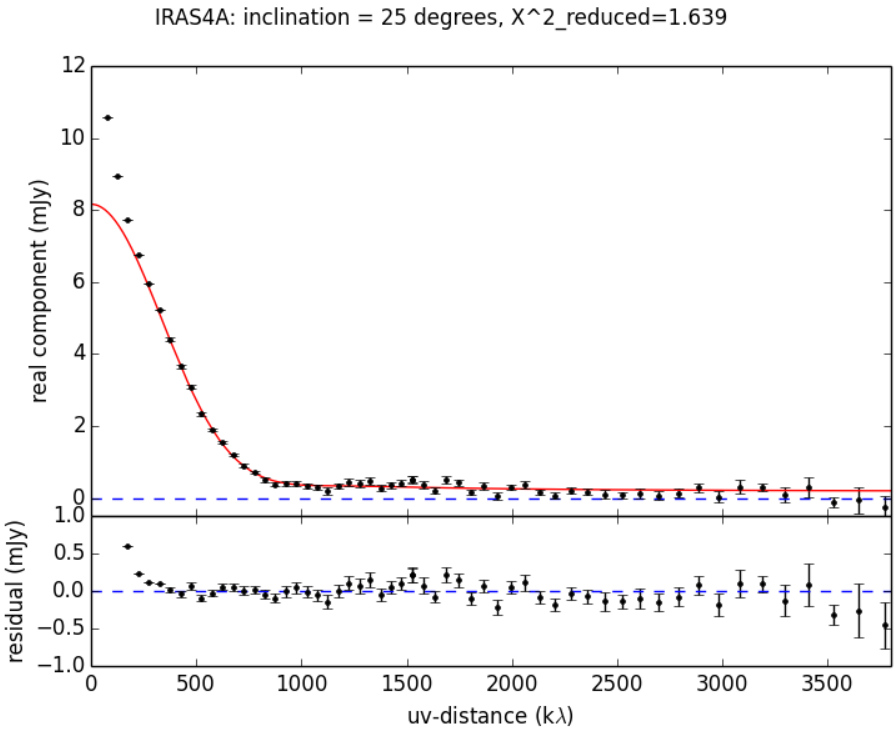

Figure 4.52: Same as Figure 4.42, for 25° inclination.

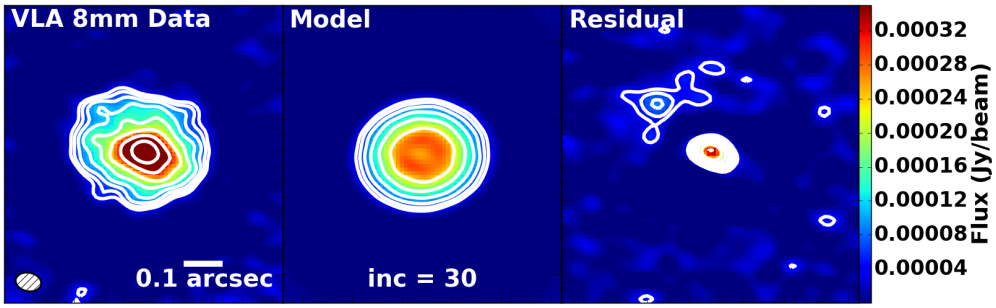

Figure 4.53: Same as Figure 4.41, for 30° inclination.

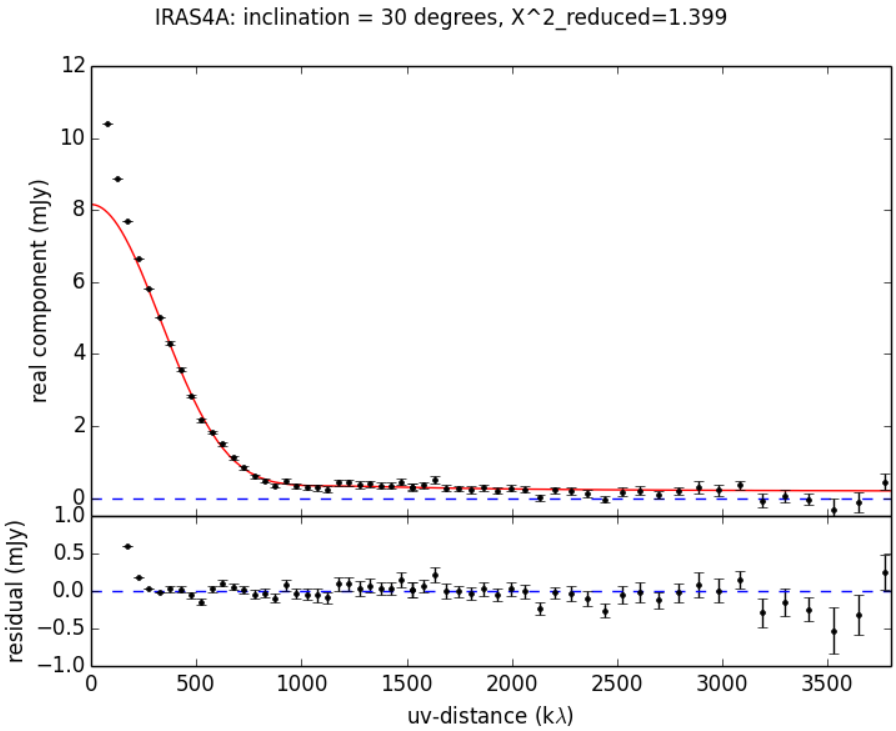

Figure 4.54: Same as Figure 4.42, for 30° inclination.

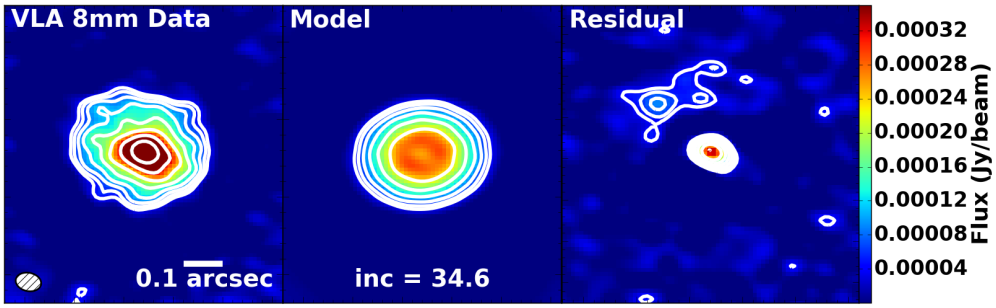

Figure 4.55: Same as Figure 4.41, for 34.6° inclination, derived from an image-plane Gaussian fit.

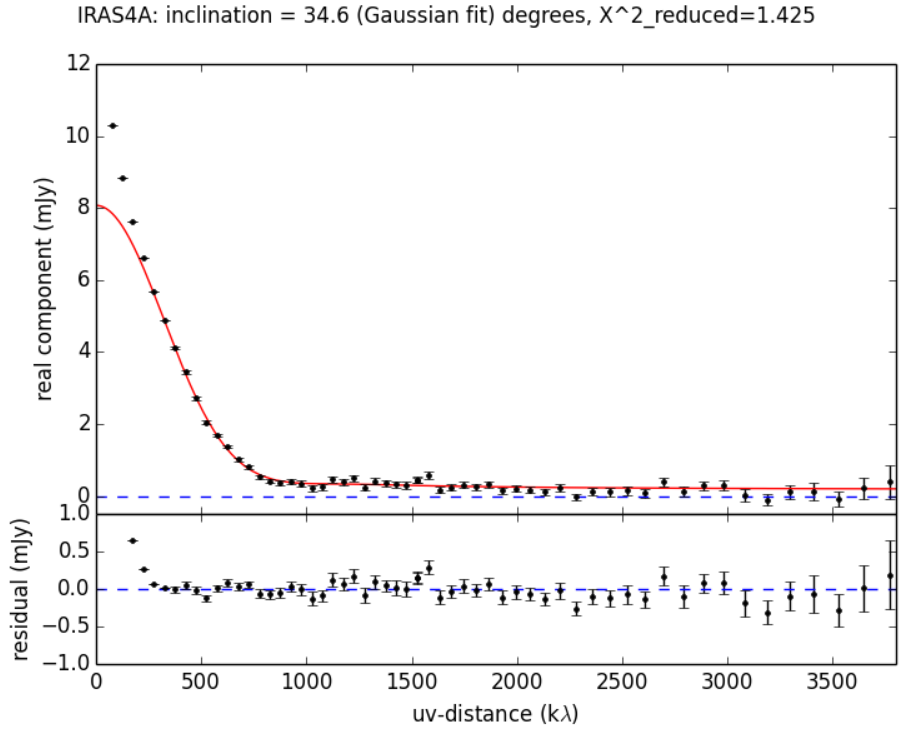

Figure 4.56: Same as Figure 4.42, for 34.6° inclination, derived from an image-plane Gaussian fit.

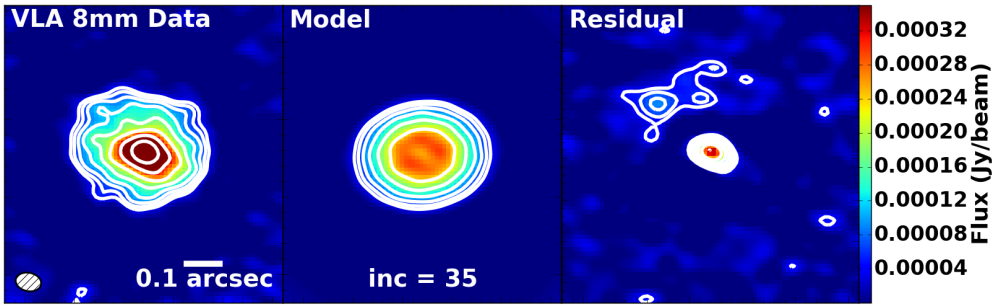

Figure 4.57: Same as Figure 4.41, for 35° inclination.

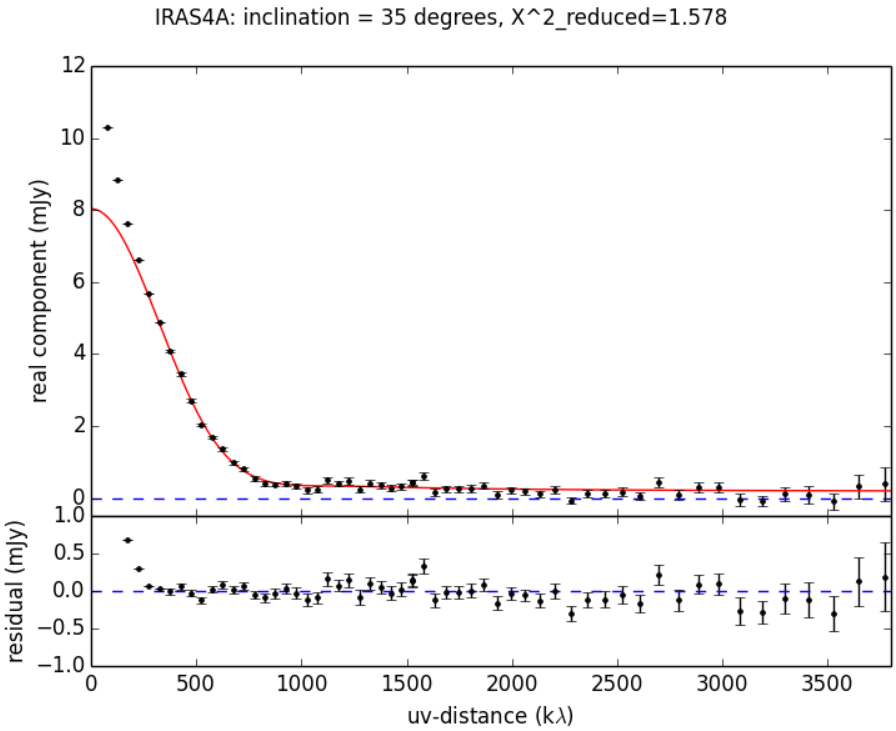

Figure 4.58: Same as Figure 4.42, for 35° inclination.

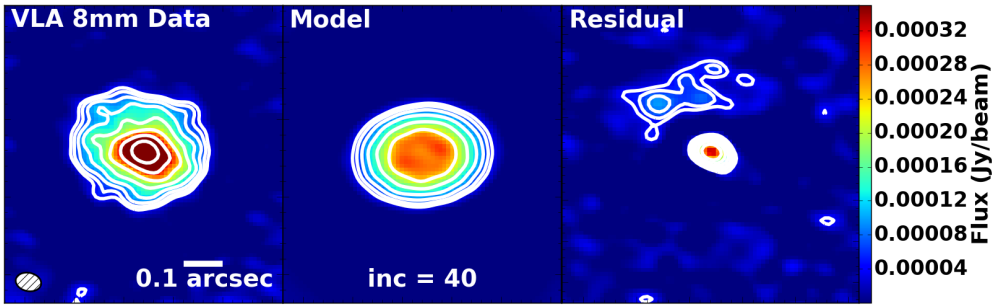

Figure 4.59: Same as Figure 4.41, for 40° inclination.

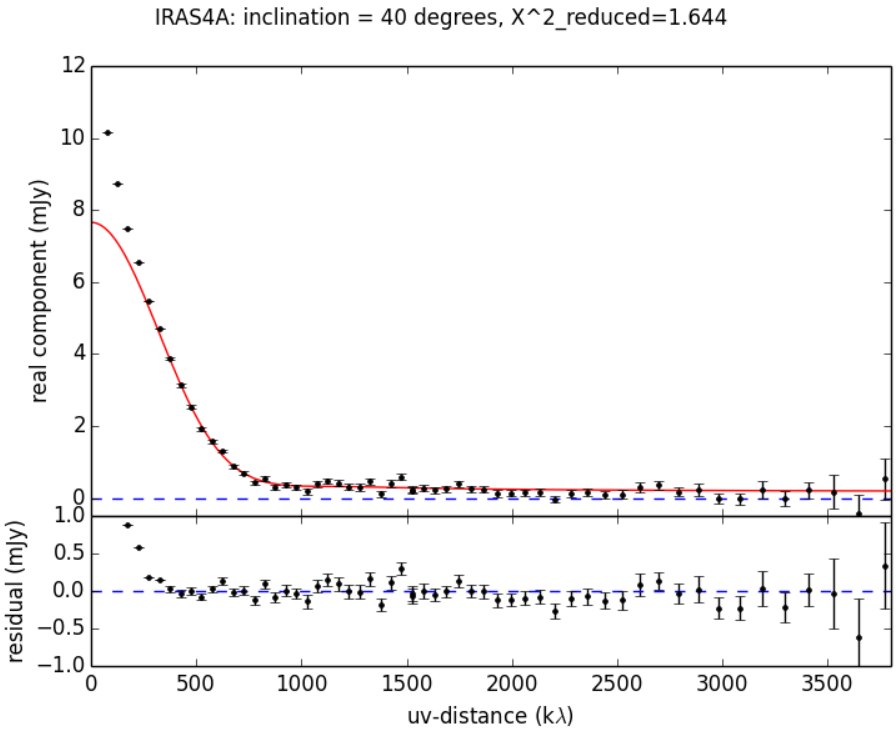

Figure 4.60: Same as Figure 4.42, for 40° inclination.

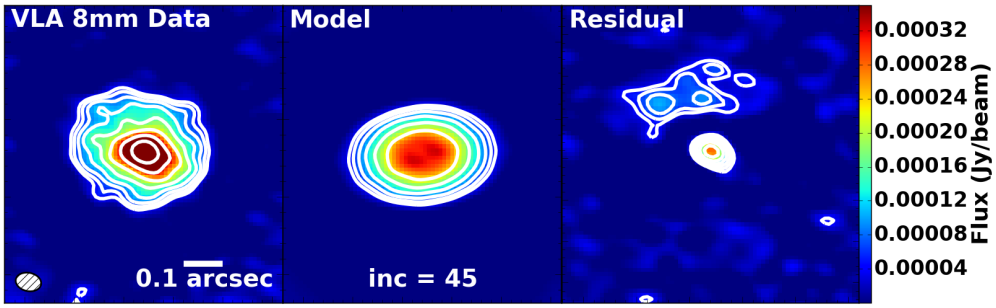

Figure 4.61: Same as Figure 4.41, for 45° inclination.

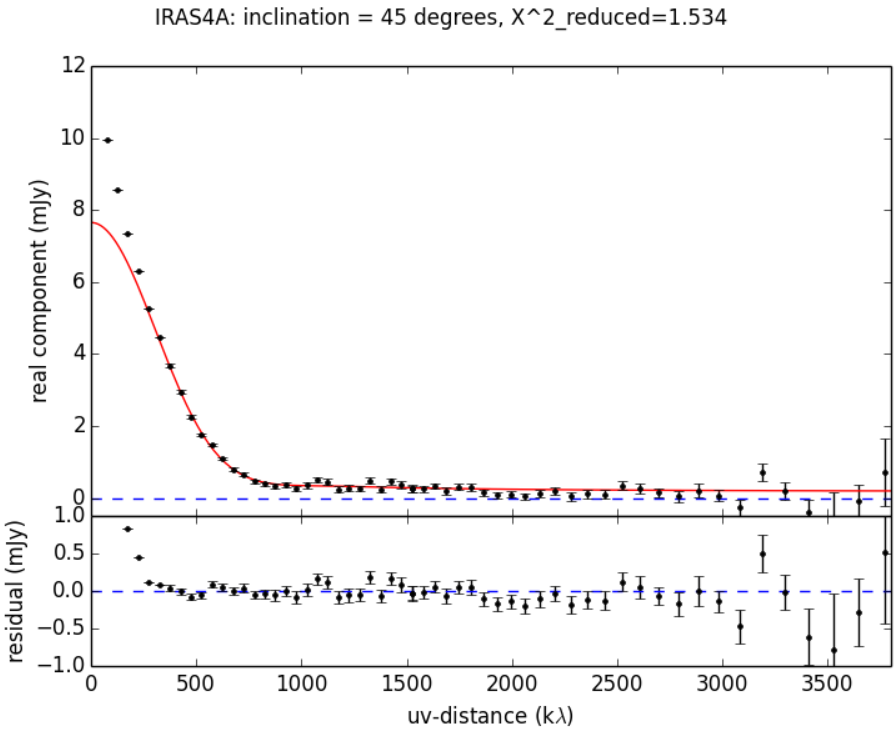

Figure 4.62: Same as Figure 4.42, for 45° inclination.

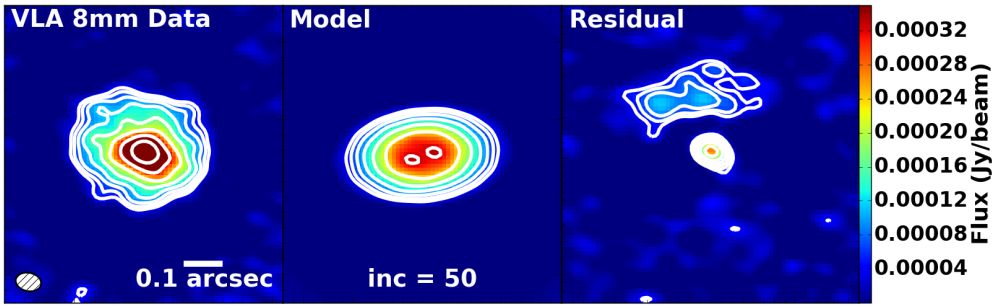

Figure 4.63: Same as Figure 4.41, for 50° inclination.

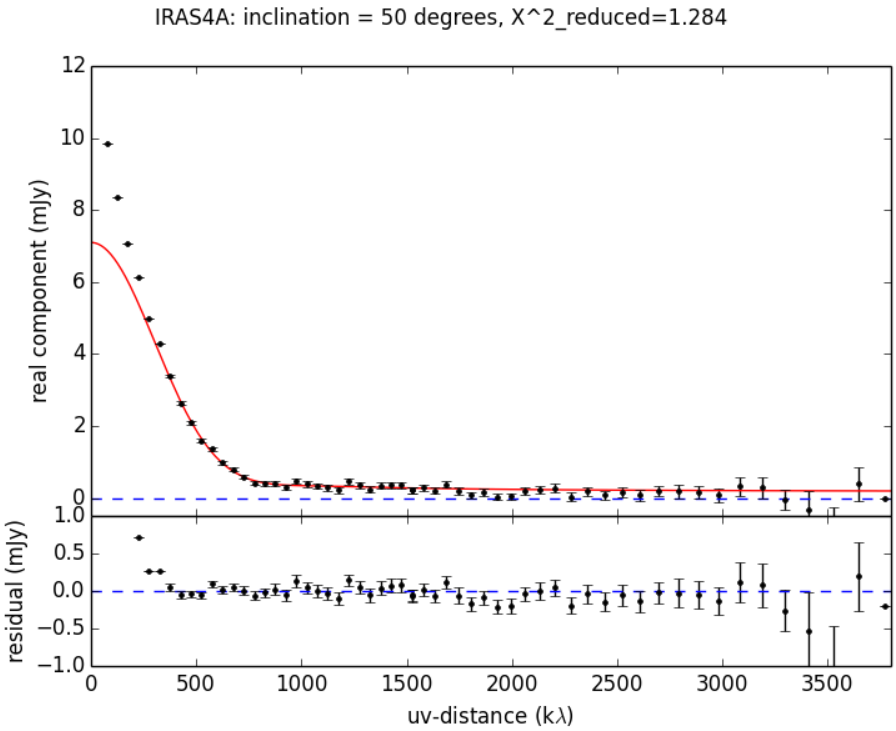

Figure 4.64: Same as Figure 4.42, for 50° inclination.

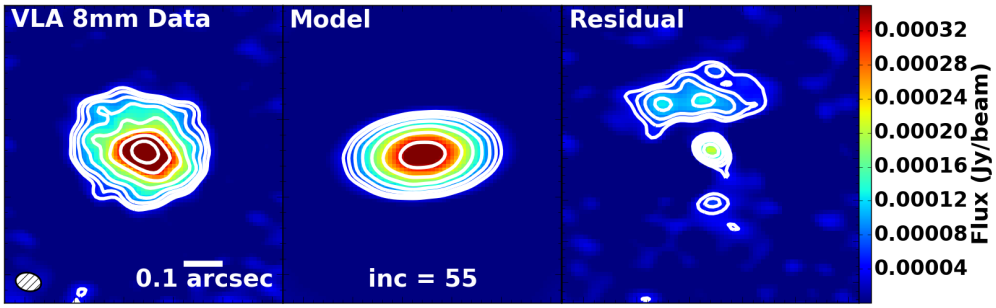

Figure 4.65: Same as Figure 4.41, for 55° inclination.

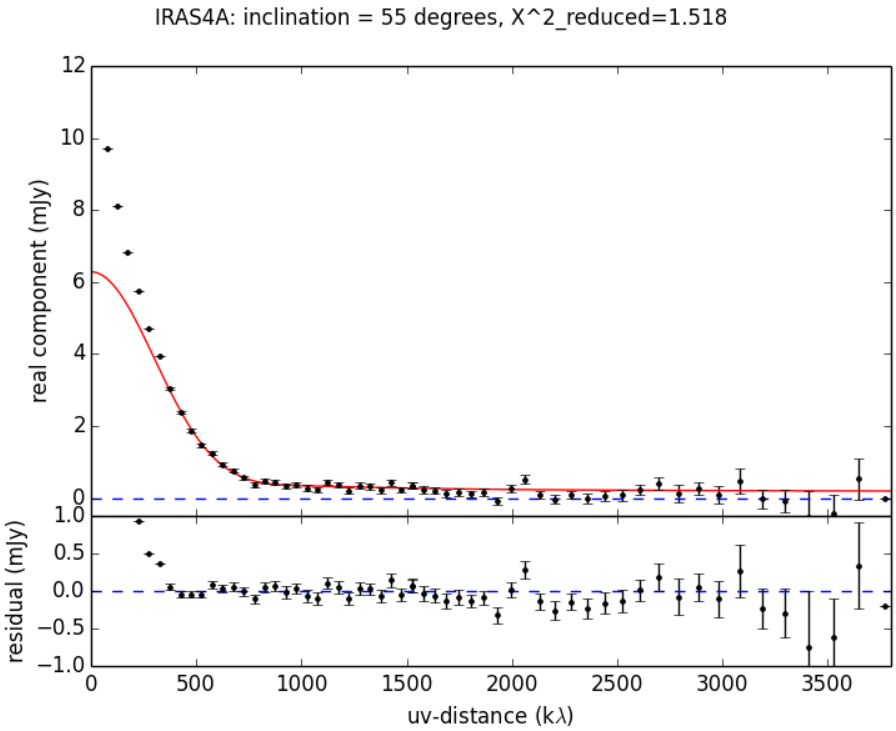

Figure 4.66: Same as Figure 4.42, for 55° inclination.

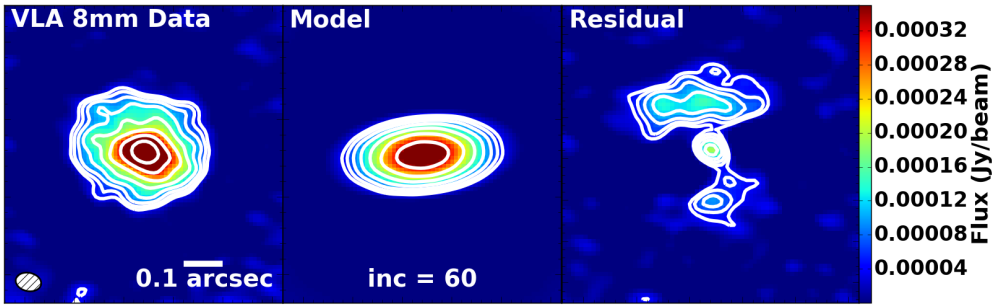

Figure 4.67: Same as Figure 4.41, for 60° inclination.

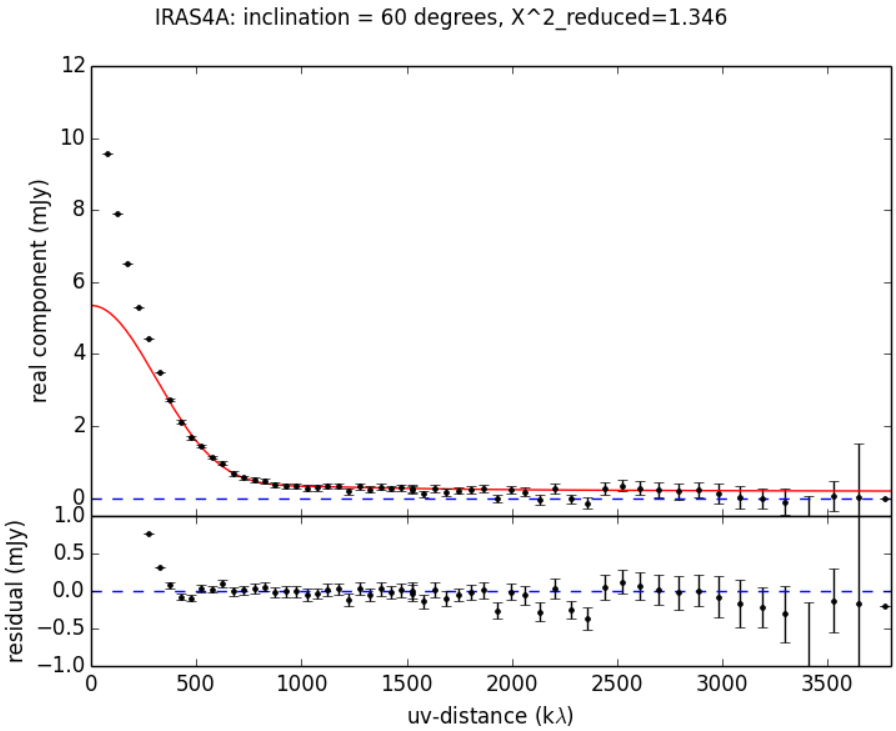

Figure 4.68: Same as Figure 4.42, for 60° inclination.

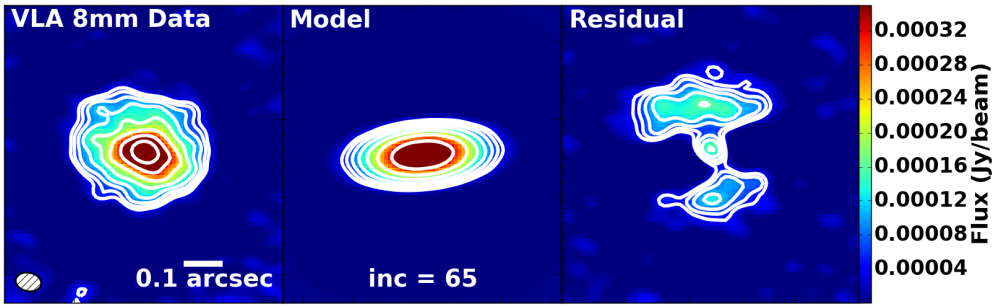

Figure 4.69: Same as Figure 4.41, for 65° inclination.

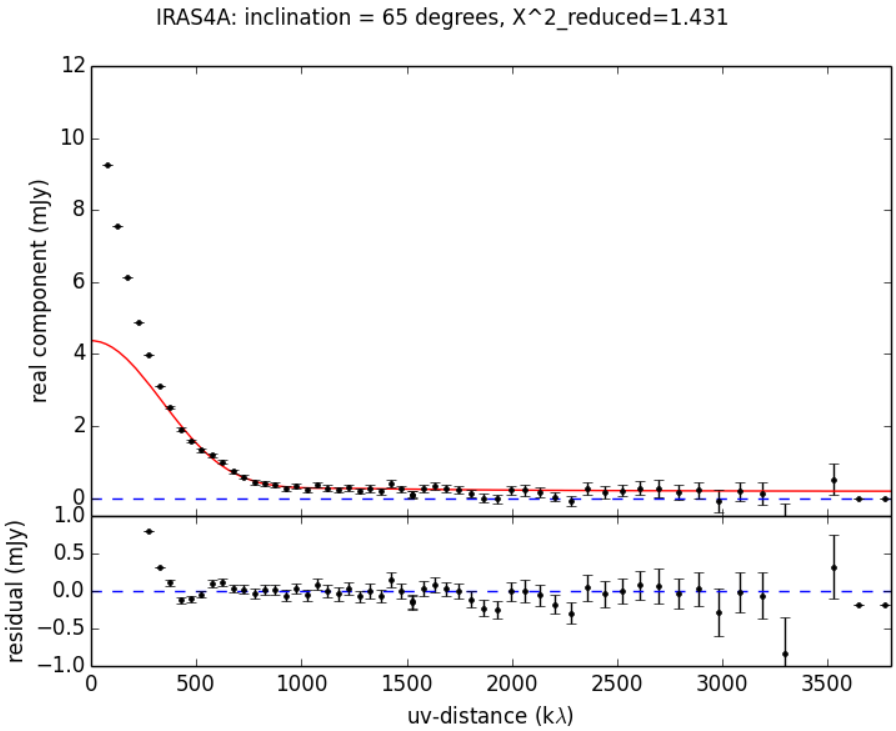

Figure 4.70: Same as Figure 4.42, for 65° inclination.

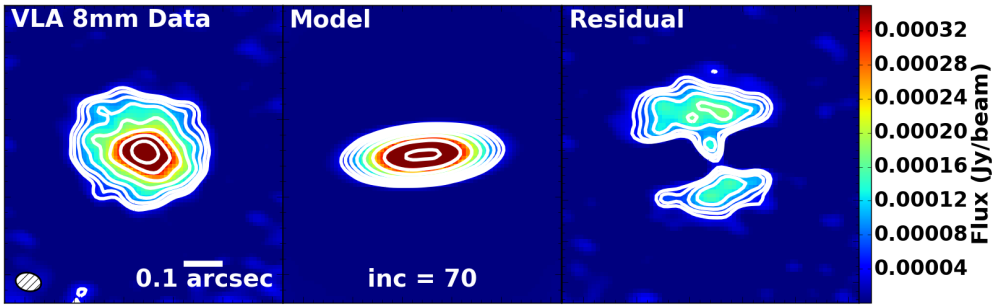

Figure 4.71: Same as Figure 4.41, for 70° inclination.

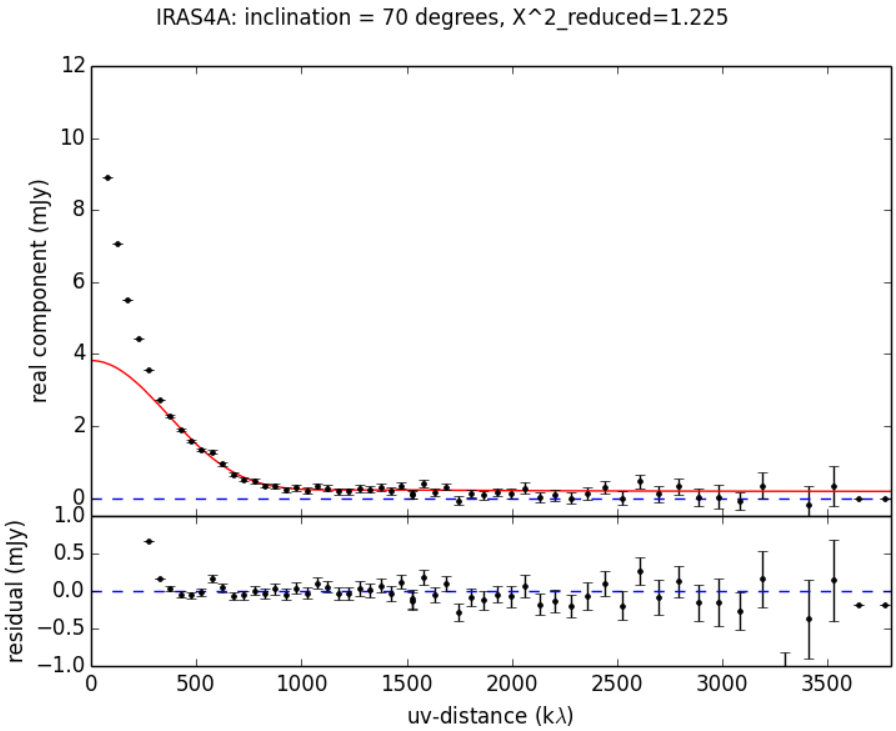

Figure 4.72: Same as Figure 4.42, for 70° inclination.

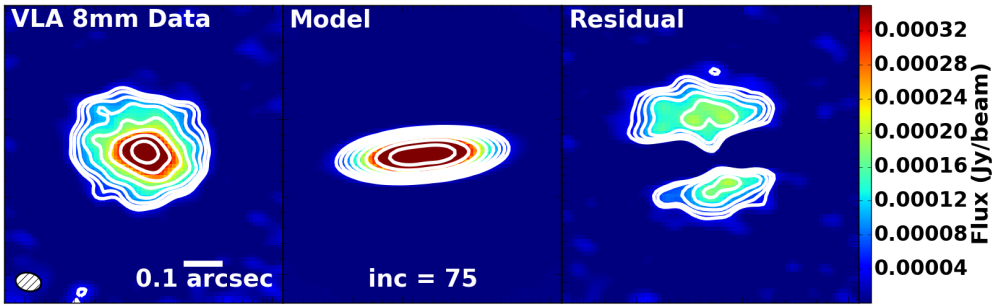

Figure 4.73: Same as Figure 4.41, for 75° inclination.

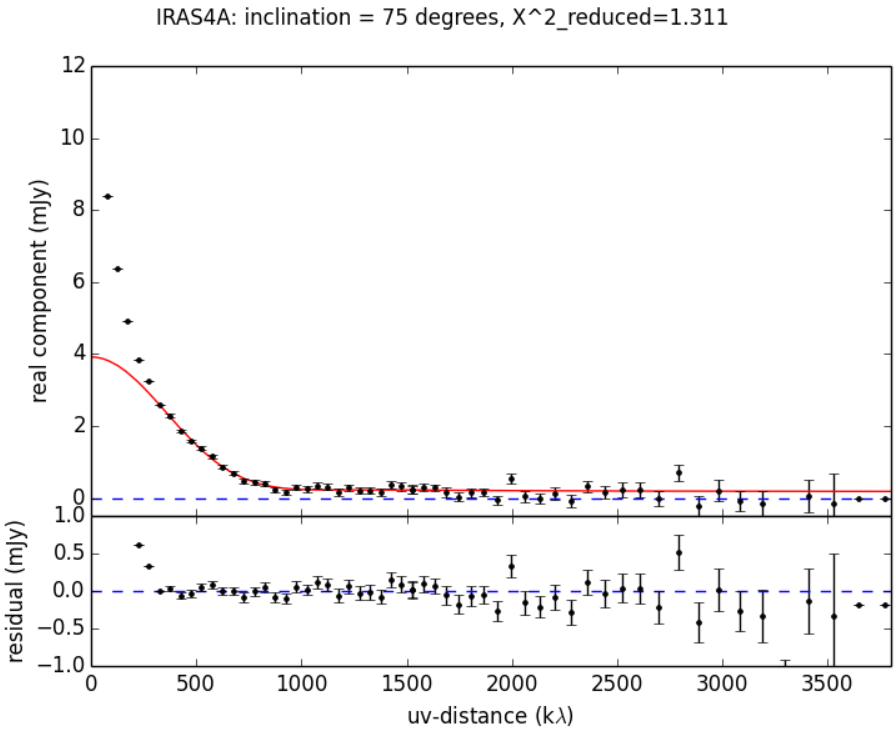

Figure 4.74: Same as Figure 4.42, for 75° inclination.

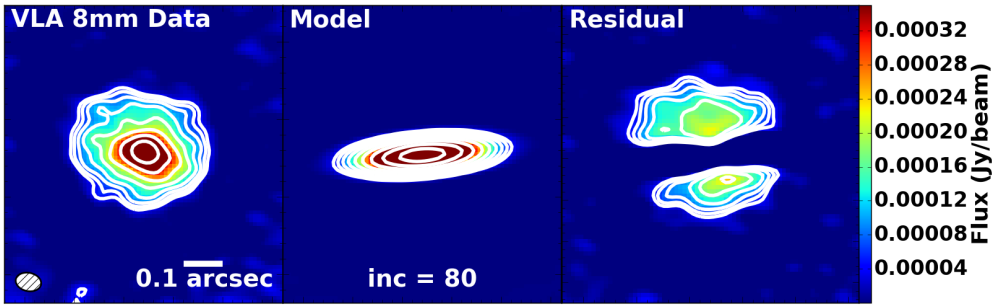

Figure 4.75: Same as Figure 4.41, for 80° inclination.

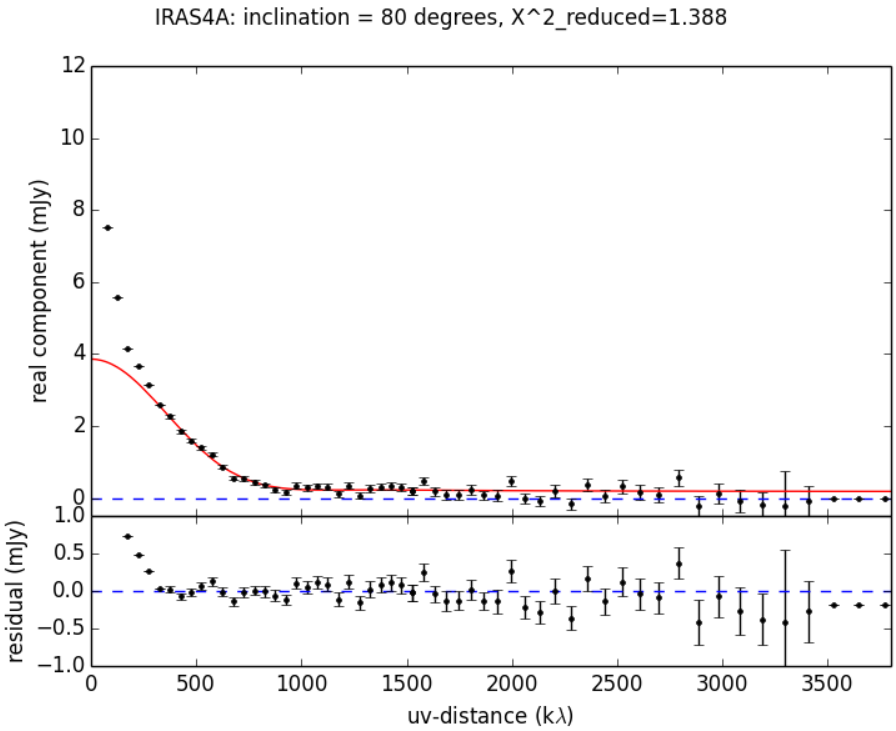

Figure 4.76: Same as Figure 4.42, for 80° inclination.

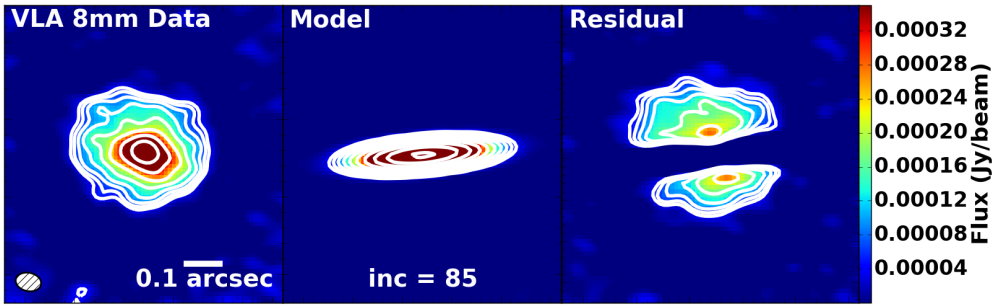

Figure 4.77: Same as Figure 4.41, for 85° inclination.

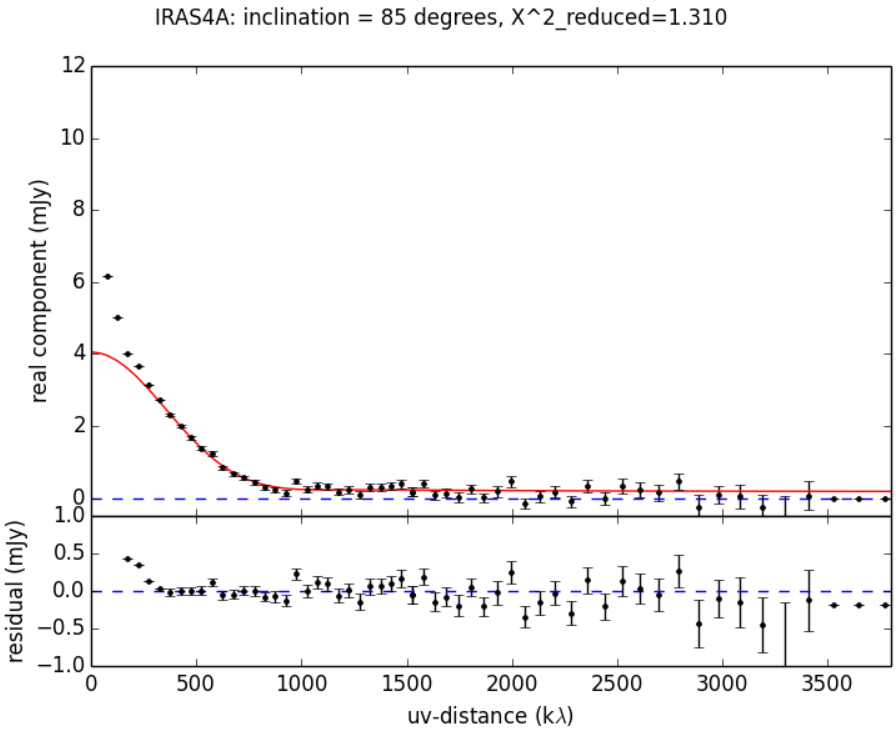

Figure 4.78: Same as Figure 4.42, for 85° inclination.

Chapter 5

Substructure in the Protostellar Disk around the Class I Protostar IRS 63

We examined the circumstellar disk around the Class I protostar IRS 63 with ALMA dust continuum observations to search for disk substructure and determine whether or not planet formation or other mechanisms for disk sculpting have already begun in the Class I phase. Since we have shown that relatively large Class 0 and I disks are somewhat common (Chapters 3 and 4), the next natural step to studying embedded disks at the earliest times is to search for substructures such as rings, gaps, and spiral arms. We find that in our ALMA observations the disk around IRS 63 does have substructure, a series of concentric rings and gaps, indicating that processes contributing to disk substructures are underway during the Class I phase.

5.1 Introduction

Protostellar disks are undeniably and intimately linked to the earliest stages of planet formation. Understanding when disk substructures commence formation and how they develop with protostellar evolutionary stage would shed light on exactly when and how planets begin to form within protostellar disks. While disks around Class I objects have begun to be characterized systematically (e.g., Andrews & Williams, 2005; Eisner, 2012), their more evolved Class II and III counterparts, which have dissipated most of the envelopes in which they are embedded, have been studied in much more detail. Recently the first definitive gaps in a protostellar disk—possible signs of fledgling planets clearing the disk—were discovered

The work in chapter is preliminary.

in a Class II system, and the Class I phase may indeed be a crucial stage for early planet formation.

The ALMA long-baseline Science Verification Data of HL Tau have revealed rings and gaps in the HL Tau disk (ALMA Partnership et al., 2015); HL Tau is widely considered to be a transition object between the Class I and Class II phase because of its large extinction (a possible residual envelope; Welch et al., 2000) and strong bipolar outflow (Movsessian et al., 2012), both atypical of traditional Class II sources. However, the lack of significant envelope structure found at millimeter wavelengths (Kwon et al., 2011) indicates that HL Tau has definitely evolved to a later stage than typical Class I disks. These data (observed in Band 6 at 1.3 mm) show for the first time the remarkable morphology of a protoplanetary disk at these resolutions ($\sim$0.035″) with a complex pattern of alternating bright and dark rings. The width of the individual rings was found to be 5 to 8 AU, where the beam was slightly less than 5 AU (ALMA Partnership et al., 2015).

Gaps, holes, and asymmetries have also been long-known in older (mostly transition) disks around pre-main sequence stars (e.g., Calvet et al., 2005; Piétu et al., 2006; Espaillat et al., 2007, 2008; Hughes et al., 2009; Casassus et al., 2013; van der Marel et al., 2013; Pérez et al., 2014). To-date, ringed substructures from ALMA observations have only been observed in disks more evolved than HL Tau, such as Herbig Ae star HD 163296 (Isella et al., 2016), TW Hydrae (Andrews et al., 2016), and AA Tau (Loomis et al., 2017). Disk clearing process governing substructure in these older disks may have already begun in the less evolved HL Tau disk. Predicted condensation radii of water ice, frozen ammonia hydrates, and clathrate hydrates (including CO_2, CO, methane, and nitrogen gas) line up well with the radii of the observed HL Tau disk gaps (Blake & Bergin, 2015). Moreover, these radii also correspond to positions where swift pebble growth is expected to occur (Ros & Johansen, 2013). Taken together, these pieces of evidence provide tantalizing hints that molecules familiar from our own solar system may be deposited onto nascent, growing planets already during the late Class I or early Class II phase. Has the process of planet formation and the associated disk

sculpting observed in HL Tau already begun during the even earlier, main Class I phase? High-resolution dust observations of a disks around Class I protostars are required to address this question directly.

If HL Tau-like rings and gaps are observed in a less-evolved disk, then planetesimal formation, or other disk sculpting processes, must have started early in the Class I phase or before (perhaps in the deeply embedded Class 0 phase). If such features are absent, then planets must have begun to form during the (late) Class I phase, rather than during the deeply embedded Class 0 phase. Spiral structures are also possible in disks around protostars, with recent ALMA observations indicating spirals from disk fragmentation in a Class 0 protostellar disk (Tobin et al., 2016a) and spiral density waves in a Class II disk (Pérez et al., 2016). Alternativley to planet-disk interactions, other phenomena that produce disk substructures (both axisymmetric gaps or non-symmetric features like spirals) including volatile snowlines, magnetized disks, and gravitational instabilities (e.g., Zhang et al., 2015; Flock et al., 2015; Takahashi & Inutsuka, 2014) may be at work. Either way detection of any type of substructure in a Class I disk will be far-reaching, providing information on initial conditions for planetesimal growth, chemical freeze-out in the disk, and presence of instabilities in disks around protostars at early times.

5.2 ALMA Observations

We targeted the rotationally-supported, Keplerian disk around the Class I protostar IRS 63 in the Ophiuchus Molecular Cloud for ALMA Band 6 (1.3 mm) dust continuum observations to search for disk gaps and hence even earlier evidence for disk evolution and planet formation than found in HL Tau. IRS 63 is massive and unusually bright in the (sub)millimeter for a Class I protostar (Brinch & Jørgensen, 2013). SMA 1.1 mm continuum data with $\sim$1.1$''$ resolution reveals a flattened structure (Brinch & Jørgensen, 2013) with major axis perpendicular to the known outflow axis orientation of the system (van der Marel et al.,

2013). The disk of IRS 63 was first confirmed when a rotation curve was fit to HCO^+ ($J = 3 \rightarrow 2$), and the fit was consistent with a disk of 0.099 $M_\odot$ having Keplerian rotation with $R = 165$ AU (Brinch & Jørgensen, 2013). This is 20% larger than the size of HL Tau's disk. IRS 63 has an inclination angle of 30° (0° is face-on), smaller than the 47° inclination of HL Tau (ALMA Partnership et al., 2015). The more face-on view means it may be easier to detect disk substructures in IRS 63 than in HL Tau because of lessened inclination effects. The Class I source IRS 63 is also considered significantly younger than HL Tau due to IRS 63's obvious envelope detected at (sub)millimeter wavelengths (Lommen et al., 2008).

We obtained ∼35 minutes of on-source Band 6 long-baseline observations with 0.06″ resolution and achieved a sensitivity of 28 μJy/beam. We proposed for 12 μJy/beam sensitivity (A-ranked Cycle 3 Program 2015.1.01512.S; PI: Segura-Cox), but we received a fraction of on-source time requested. We also made a short observation with 0.4″ (∼50 AU) resolution to recover the large-scale disk structure and adequately sample the short u,v-spacings plotted in Figure 5.2, which also clearly shows the long-baseline spacings are sensitivity-limited with our incomplete observations. Observations were taken from late 2015 to mid 2016, and used standard calibrators. We used CASA to reduce and analyze the data. The data has high signal-to-noise near the emission peak, so we applied phase and amplitude self calibration to increase the dynamic range. Interactive multiscale cleaning was used to simultaneously recover the small and large-scale disk structures in the image plane, and we weighted the image with a robust=1 Briggs parameter to optimize the trade off between sensitivity and resolution.

5.3 High-Resolution ALMA Results towards IRS 63

The ALMA Band 6 dust continuum observations are shown in Figure 5.1. No obvious substructures are detected, however faint radial breaks in the intensity distribution can be seen. The faint radial breaks may indicate that some mechanism is causing dust to

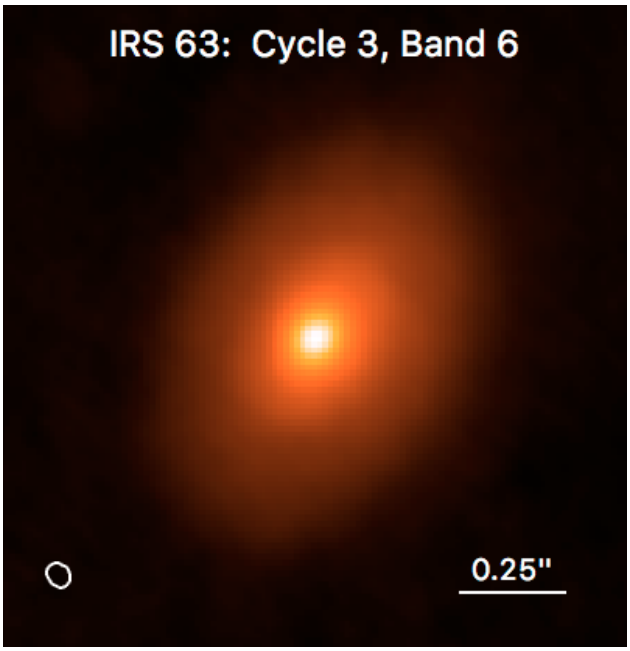

Figure 5.1: Our 35 minute on-source IRS 63 data after processing with phase and amplitude self calibration, multiscale clean, and weighting the image with a Briggs parameter of robust=1, and plotted with arcsinh stretch. The sensitivity is 28 μJy/beam with a resolution of 0.06″ ($\sim$7 AU). The beam and scale bar is shown in the lower left and lower right, respectively. While no obvious substructures are detected, faint radial breaks in the intensity distribution can be seen.

concentrate in some parts of the disk but not others, and we may be observing the very beginnings of substructure formation. There is no sharp edge at the outer part of the disk.

Because the disk is extremely well-resolved and non-Gaussian in shape, we are unable to apply the typical method of using CASA's IMFIT package to measure the position angle and sizes of the major and minor axes. A Gaussian fit to the disk only fits the central bright peak near the protostar. Instead, we determined these parameters by drawing a 10σ contour and measuring the axes where they pass through the peak of the emission. Source properties are reported in Table 5.1, with α and δ reflecting the location of the peak dust emission.

We also examine the data in the u,v-plane. We deproject the disk of IRS 63 assuming circular orbits, azimuthally average the data, and finally bin the data radially to produce an averaged visibility profile (Figure 5.2, left). The averaged visibility profile of IRS 63 reveal gentle ripples, especially when plotting the amplitude on a log scale. The smooth ripples

Table 5.1: Measured Properties of IRS 63

α (J2000):	16:31:35.658
δ (J2000):	-24:01:29.901
Major axis length:	1.14″ (143 AU)
Minor axis length:	0.83″ (104 AU)
Inclination angle:	43 degrees
Position angle:	150 degrees
Flux at 1.3 mm:	0.307 Jy
RMS noise level:	1.2×10^{-5} Jy/beam

The position angle is measured counterclockwise from north. 0° inclination indicates a face-on disk.

in the IRS 63 averaged visibility profile are similar to the profile seen in the disk of older the Herbig Ae star HD 163296 (Figure 5.2, right). HD 163296 was recently found to have three dark rings at 60, 100, and 160 AU (Isella et al., 2016). HD 163296's disk has a much larger radius than IRS 63, with gaps much further from the central peak than than the disk of IRS 63; this accounts for the different *u,v*-coverages required to detect the respective substructures. Even though IRS 63 has a lower total flux than HD 163296, the dynamic range requires that our data be plotted with a log scale for the amplitude to see the ripples in the averaged visibility profile. The similarities in the visibility profiles between the older disk with known gaps and our young disk are enticing indications that gaps and rings may also be present in the disk of IRS 63 which are not obvious in the image plane.

5.3.1 Image Filtering Clearly Reveals Gaps

While substructures in the disk of IRS 63 are not clear in the original image due to dynamic range limitations, they become apparent after applying image filters. To increase the contrast of the observations, we remove the large-scale disk emission from the original image with unsharp mask filtering, as was done in Pérez et al. (2016) to emphasize spiral arm structures in a protoplanetary disk. To apply the unsharp mask filtering technique, we smoothed the original, raw image with a 2D Gaussian 1.5× the beam size, scaled it by a factor of 0.32, and

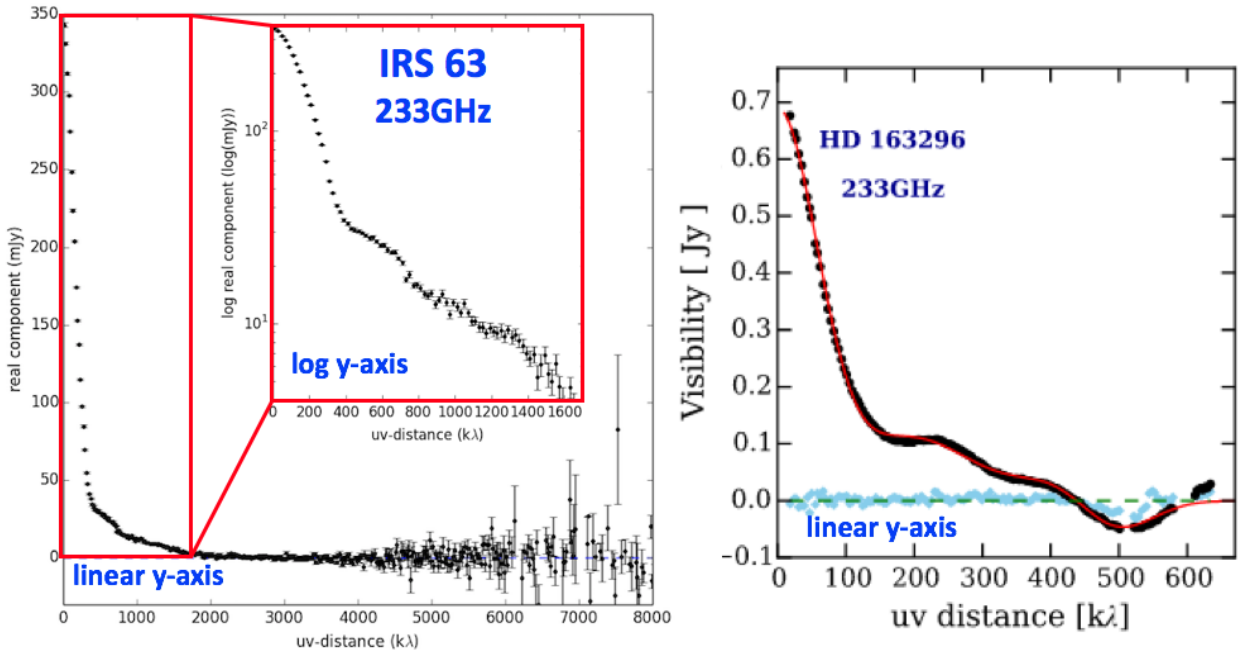

Figure 5.2: Amplitude vs u,v-distance plots for Band 6 ALMA data of the disk around the Class I protostar IRS 63 (Left; our data) and the disk around the ringed older Herbig Ae star HD 163296 (Right; Figure taken from Zhang et al., 2016, reproduced by permission of the AAS).

subtracted it from the raw image. The scale factor of 0.32 is a trade off between maximizing the image contrast and ensuring that after subtraction all intensity values in the disk remain positive. The unsharp masking filtered image (Figure 5.3, left) has an RMS of 1.2×10^{-5} Jy/beam, similar to the raw image, indicating that this filtering method preserves much of the noise information. The resulting filtered image with increased contrast reveals the gaps and rings in the disk of IRS 63. HL Tau has much less material in the gap; hence why the gaps are obvious without the use of imaging filters. There are possible spiral arm structures at radii larger than the central bright ring, though it is unclear whether the spirals are real or simply a noise artifact due to limited sensitivity near the edge of the dust disk.

We also applied an alternative normalized filter to the raw data (Figure 5.3, right). We smoothed the raw image with a 2D Gaussian 1.5× the beam size and divided the raw image by the smoothed image, normalizing the high-resolution data to the smoothed larger-scale component. The noise information of the data using the normalized filter is not preserved

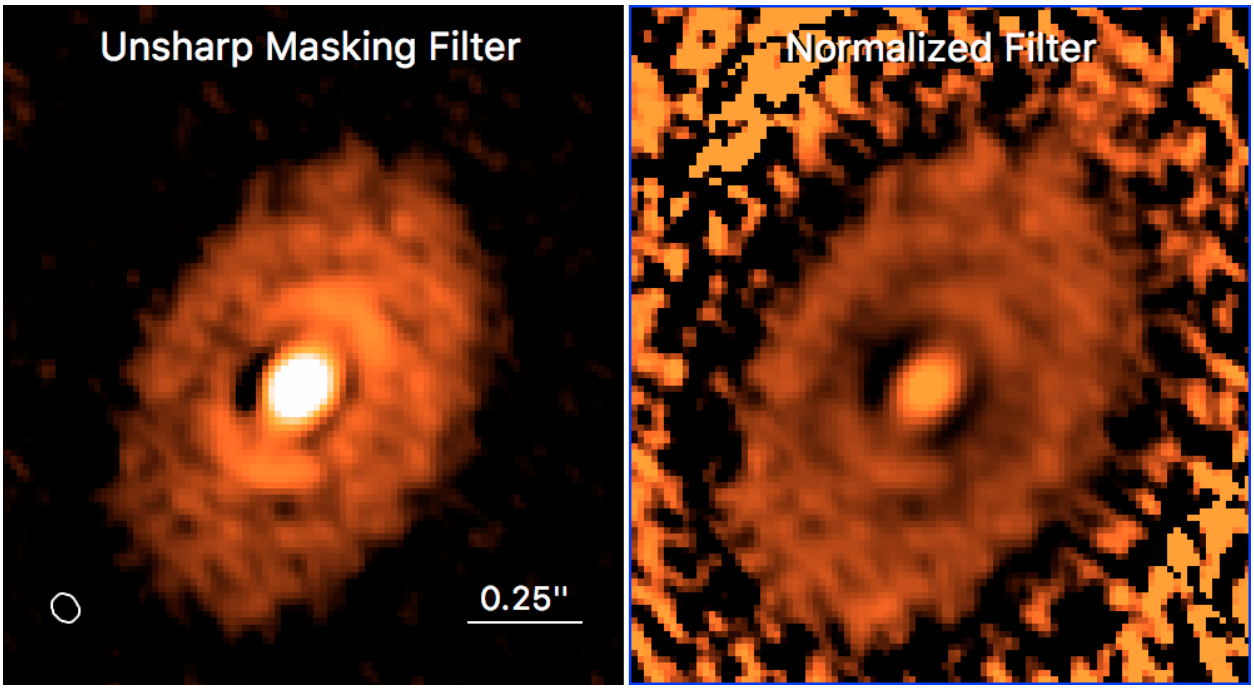

Figure 5.3: Left: unsharp masking filter applied to the raw image of IRS63. Right: normalized filtered image. The images are plotted on the same physical size scale, with arcsinh stretch, and different color scales for each figure. The beam and scale bar is shown in the left panel. By increasing the contrast of the images with the use of filtering, we have revealed rings and gaps in the disk of IRS 63.

as well as in the unsharp masking filtered image, made obvious by examining the areas of the filtered images outside the disk (Figure 5.3). The normalized filter does not preserve noise information as well because the final normalized filtered image depends on the SNR of each pixel, resulting in high-amplitude noise peaks and holes outside of the disk with low SNR; however, in the disk where SNR is higher, the noise level is better preserved. The benefit of using the normalized filter is that the profile of the outer part of the disk is flatter, which will allow for a better estimate of the gap depth with higher signal-to-noise ratio after azimuthally averaging the data (Section 5.4).

5.3.2 Position-Intensity Cuts

Three dark gaps and three bright rings are revealed by taking a position-intensity cut 1″ in length, positioned along the major axis, and centered on the peak emission in both the

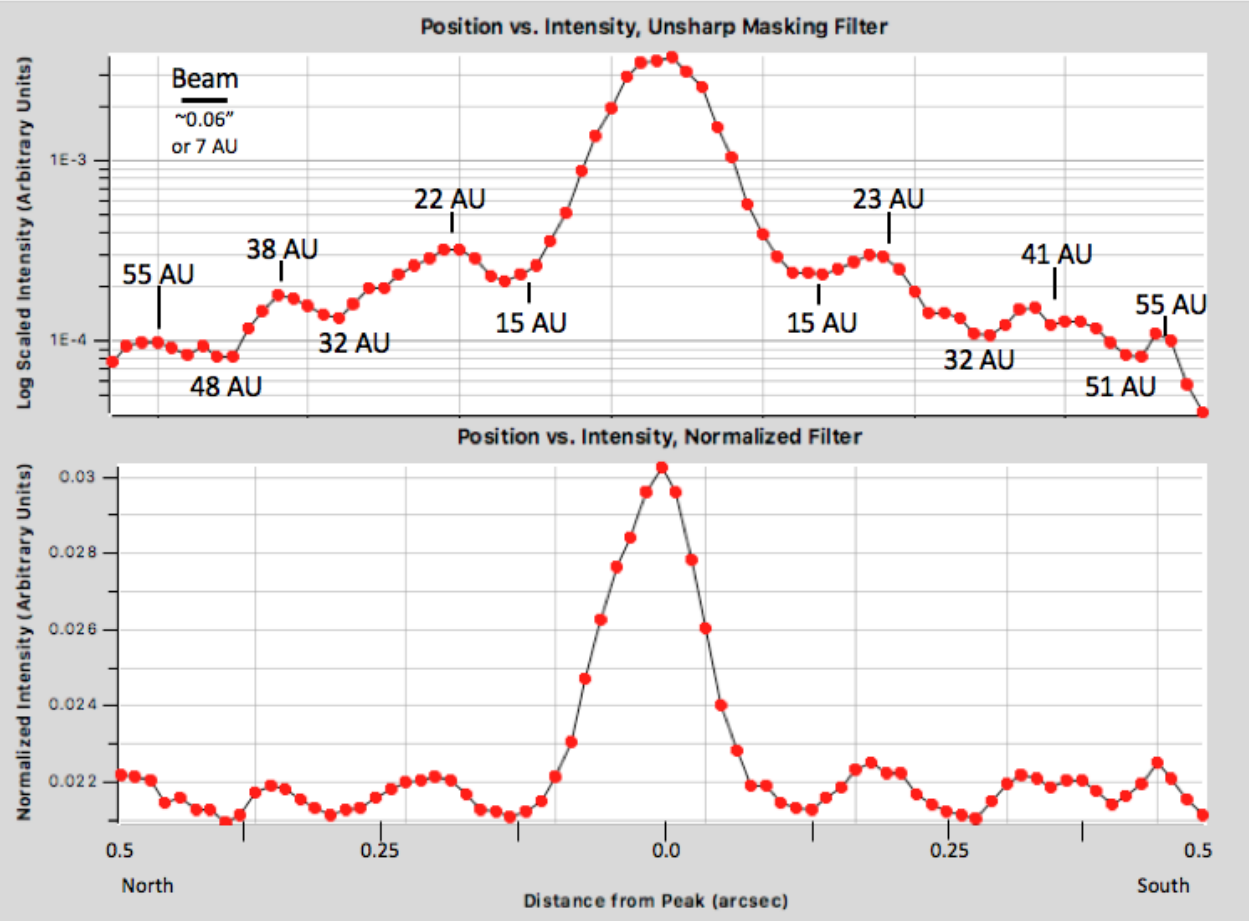

Figure 5.4: A position-intensity cut 1″ in length, positioned along the major axis and centered on the peak emission, of both the unsharp masking filtered image (top panel) and the normalized filter image (bottom panel). The width of the beam is shown in the upper left. Estimated physical distances between the peak emission and the rings and gaps in AU are marked.

unsharp masking filtered image and the normalized filter image (Figure 5.4). Emission along the major axis is not subject to inclination effects, giving us a relatively accurate estimate of gap radii by eye. Because of the dynamic range of the images, the scaled intensity from the unsharp masking filtered image must be plotted on log scale, but the normalized intensity from the normalized filtered image needs only a linear scale. In both filtered images, three dark rings and three bright gaps are recovered at similar radii. The three gaps are at roughly 15, 32, and 50 AU from the central peak. The gap widths appear by eye to be approximately the size of the beam (∼7 AU).

The significance detection level of the gaps is defined by the contrast between gap minimum and the neighboring ring maximum because the data are limited by both noise and the dynamic range. Now that we have an estimate of gap radii from the filtered images, we return to the raw data with completely unaltered noise levels to determine the significance of gap detections. While the gaps were not immediately obvious in the raw data, on close inspection, three shallow rings and gaps can be recovered with short position-intensity cuts ($\sim$0.1″ in length) across each ring-gap pair. Due to the dynamic range of the data, a full-length position intensity cut across the source, even when plotted on log scale, flattens the appearance of the gaps too much to be noticeable by eye. While most of the disk has a greater than 20σ detection within a 60 AU radius (with 425σ on the central peak), the inner two gaps have a 7.2σ and 3.2σ detections, while the outermost gap has a paltry 1.5σ detection (Table 5.2).

Table 5.2: Significance of Gap Detecions

Gap	Detection Significance	Radius (AU)
Inner	7.2σ	$\sim$15
Middle	3.2σ	$\sim$32
Outer	1.5σ	$\sim$50

Significance of gap detections were measured from the unfiltered raw image. R is determined by eye.

5.4 Modeling the Gaps

To quantitatively determine gap radii and widths, rather than relying on qualitative estimates by eye (Section 5.3.2), we apply a simple model to the data in image-space. We take into account the orientation and inclination of the disk, deproject the data assuming circular orbits for the circumstellar dust, and azimuthally average and bin the data to increase

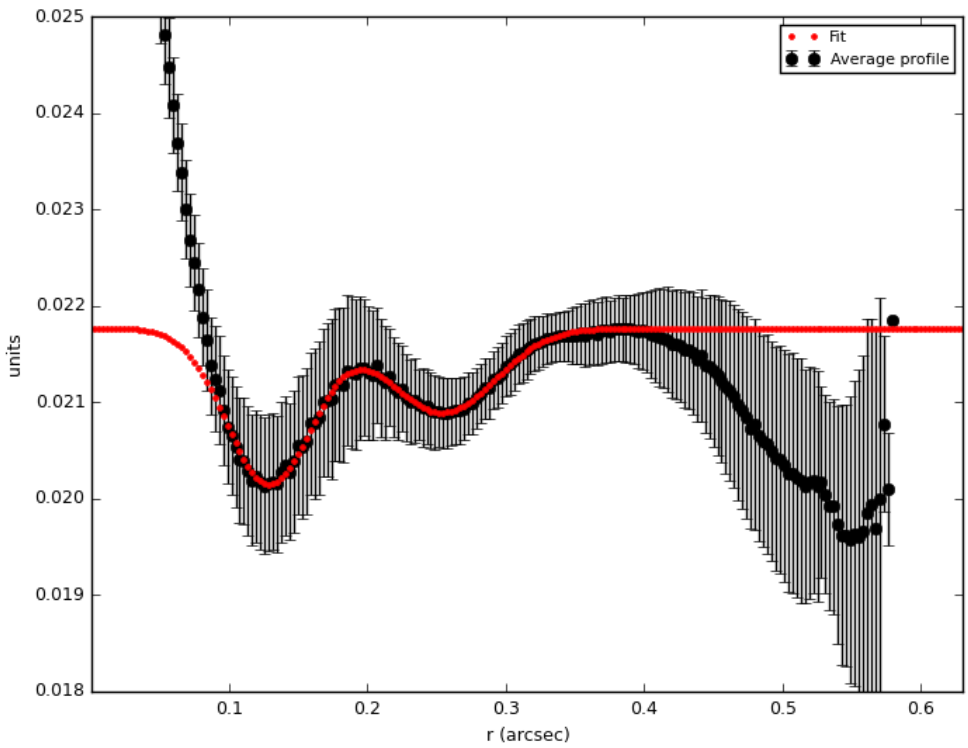

Figure 5.5: Fit from deprojected and azimuthally averaged normalized filtered image. Black points: average intensity profile. Red points: fit to the average profile. The intensity units are arbitrary. The outer part of the disk is flatter than the unsharp masking filter (Figure 5.6), allowing for a better estimate of the gap depth with higher SNR after azimuthally averaging. The gap properties in Table 5.3 are derived from this model.

the SNR of the data, especially in the outer part of the disk. We perform this for both the normalized filtered and unsharp masking filtered images, with the resulting average intensity profiles shown in Figures 5.5 and 5.6, respectively. After azimuthally averaging, the outer $\sim$50 AU gap is lost in both the unsharp masking and normalized filtered image intensity profiles. It is unclear if the outer gap, with a detection of only 1.5σ, is simply a noise artifact due to limited sensitivity near the edge of the dust disk, is a part of possible spiral arm structures at radii larger than the central bright ring, or is elliptical in shape and lost during azimuthal averaging. Thus, we are unable to estimate the radii or width of the possible outer gap with our simple model.

To model the gap radii and widths, we use Python's MPFIT to fit two subtracted 1D

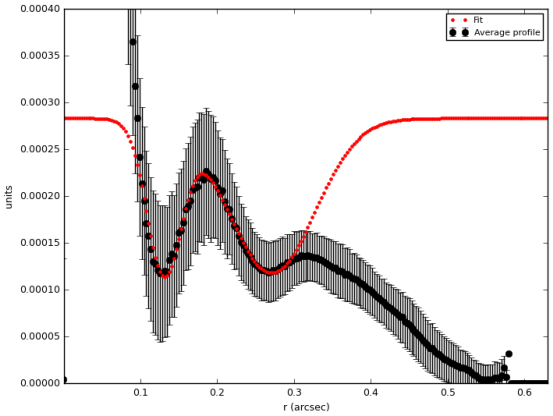

Figure 5.6: Same as Figure 5.5, for the unsharp masking filtered image. Here it is clear that estimating gap width, especially for the second gap, is necessarily more uncertain with our simple modeling due to the sloped profile of the outer part of the disk.

Gaussian profiles (one for each of the two gaps preserved in the azimuthally averaged intensity profiles) from a flat base-intensity threshold chosen based on the highest peak of the bright rings in the disk (Figures 5.5 and 5.6). While this method does not recover the shape of the entire disk, it allows for reasonable quantitative estimates of gap locations and widths. We performed this fit method with the azimuthally averaged intensity profiles of both the normalized filtered and unsharp masking filtered images. The intensity profile from the normalized filtered image is flatter and more suitable for our method of Gaussian subtraction fitting. In the intensity profile from the unsharp masking filtered image, the profile is sloped and a flat base-intensity threshold does not well approximate the intensity of the data. In particular, the Gaussian fit for the second gap in this case is especially uncertain. Therefore, we report the model gap radii and width fit results from the intensity profile from the normalized filtered image only (Table 5.3). The gap widths reflect the 1D Gaussian best-fit FWHM for each gap.

Table 5.3: Modeled Gap Parameters

Gap	Radius (″)	Radius (AU)	Width (″)	Width (AU)
Inner	0.129 ± 0.006	16.1 ± 0.8	0.07 ± 0.01	8.8 ± 1.3
Middle	0.254 ± 0.007	31.8 ± 0.9	0.09 ± 0.02	11.3 ± 2.5

The parameters were derived from the normalized filtered image.

5.5 Discussion of IRS 63 Substructure

Our long-baseline ALMA Band 6 data of IRS 63 have revealed two clear gaps at 16.1 and 31.8 AU. A third gap was detected with only a 1.5σ detection level and is not found when azimuthally averaging the filtered image intensity profiles. It is unclear if the outer gap, with a detection of only 1.5σ, is simply a noise artifact due to limited sensitivity near the edge of the dust disk or is part of not an axisymmetric gap, but rather a series of spiral-like features in the outer part of the disk. The spiral disk structure found in the Class 0 system L1448 IRS3B (Tobin et al., 2016a) shows that disk fragmentation may cause substructure in disks at early times. The inner two gaps in the disk of IRS 63 are however are axisymmetric in the older Class I stage, indicating that disk fragmentation is likely not the dominating factor influencing the substructure morphology in our data.

Numerical studies of observed rings and gaps in protoplanetary disks have suggested that gaps may be opened by planets (e.g., Wolf & D'Angelo, 2005; Pinilla et al., 2015; Dong & Dawson, 2016). Jin et al. (2016) modeled the dust ring and gaps in the HL Tau disk, finding that the observed features can be mostly reproduced via planet-disk interactions, with three planets of ∼0.35, 0.17, and 0.26 $M_{Jupiter}$ located at 13.1, 33.0, and 68.6 AU. If planet-disk interactions cause the substructure we see in the Class I IRS 63 disk, our ALMA observations of the rings and gaps are evidence of even earlier footholds of planet formation than the rings and gaps around the Class II protostar HL Tau (ALMA Partnership et al., 2015). The Class I phase would be a crucial stage for planet formation, with planetesimals beginning to form

already in the Class I stage or earlier. The rings and gaps of IRS 63 are reminiscent of those seen in the Class II HL Tau disk (ALMA Partnership et al., 2015). HL Tau's disk has a pattern of alternating bright and dark rings, attributed to gravitational torques from planetesimals carving gaps in the disk (Kanagawa et al., 2015). HL Tau's lack of significant envelope structure found at millimeter wavelengths (Kwon et al., 2011; Pinte et al., 2016) indicates HL Tau has definitely evolved to a later stage than Class I disks like IRS 63. The similarities between the rings and gaps between the Class I and II stages is striking on first inspection; yet the differences between the properties of the substructures will give the most insight into disk and planet evolution at early times. Remarkably, HL Tau also has gaps at 15 and 32 AU (ALMA Partnership et al., 2015). Assuming Keplerian orbits, the gaps in IRS 63 are in nearly a 1:3:6 resonance, consistent within the uncertainty of the $\sim$7 AU beam. HL Tau has a resonance chain of 1:4:6:8 for its inner four dark gaps (ALMA Partnership et al., 2015). Multiple resonances are a tantalizing hint that the gaps may indeed caused by early planetesimal formation (see Baruteau & Papaloizou, 2013).

Snowlines in disks are another possible way to form rings in the dust of protostellar disks. A snowline marks the radius of a protoplanetary disk at which a volatile—chemical compounds with low melting points such as water or CO—reaches its condensation temperature. Snowlines play a role in disk evolution by promoting expedient growth of dust grains covered in ices (e.g., Cieza et al., 2016), which shortens the amount of time needed to form planetesimals in core-accretion models (Pollack et al., 1996). Simulations have shown that in a disk around an older Herbig star, a clear gap of dust emission can be formed between the water and CO ice snowlines, creating concentric rings in the disk (Pinilla et al., 2017). Zhang et al. (2015) showed that for HL Tau, the gaps could be due to rapid pebble growth around the condensation fronts of water ice, ammonia, and CO. In these studies, no planets are required to open gaps in the disk.

Magnetized disks are also capable of forming gaps without the need for planets via MRI if the gas ionization varies with disk radius (e.g., Isella et al., 2016). MRI will generate tur-

bulent motions transporting angular momentum outward, allowing disk material to accrete onto the central star (Balbus & Hawley, 1998). If the gas ionization is not constant with radius, then the flow of disk material towards the protostar varies across the disk and dust can pile up radially into rings. Dead zones, regions of low gas ionization where MRI effects are suppressed, are thus expected to have lower gas surface densities compared to the rest of the disk. Pinilla et al. (2016) used an MHD model to produce dust gaps in a protoplanetary disk with corresponding depleted in-gap gas densities in the disk dead zone. Non-ideal 3D MHD simulations have revealed that the formation of a gap near a bump in radial surface density near the outer edge of the dead zone is possible (Flock et al., 2015).

Gravitational instabilities may also produce ringed structures in protoplanetary disks. Prior to the ALMA observations of HL Tau, secular gravitational instability—where the effect of dust grains on gas motion is ignored—was proposed as formation mechanism of multiple ring structures (Takahashi & Inutsuka, 2014). Takahashi & Inutsuka (2016) found that secular gravitational instability was able to reproduce all ring structures in HL Tau without the need for large planetesimals in the disk.

While it is tempting to immediately attribute rings and gaps to nascent planet-disk interactions, it is important to keep in mind that other phenomena such as volatile snowlines, dead zones, and gravitational instabilities can produce ring and gap structures in protostellar disks. In any case, the detection of substructures already formed in the disk around the Class I protostar IRS 63 is momentous, indicating that substructures are likely ubiquitous across many stages of protostellar evolution. The properties of the rings in gaps of IRS 63 will provide information regarding the initial conditions for planetesimal growth, chemical freeze-out in the disk, and presence of instabilities in disks around protostars at early times.

This chapter makes use of the following ALMA data: ADS/JAO.ALMA#2015.1.01512.S. ALMA is a partnership of ESO (representing its member states), NSF (USA) and NINS

(Japan), together with NRC (Canada), MOST and ASIAA (Taiwan), and KASI (Republic of Korea), in cooperation with the Republic of Chile. The Joint ALMA Observatory is operated by ESO, AUI/NRAO and NAOJ.

Chapter 6

Conclusions and Work in Progress

6.1 Conclusions

Even though disks around Class 0 and I protostars govern accretion of material onto the central protostar and likely host the early stages of planetesimal growth, before this work few Class 0 and I protostellar disks had been studied in detail. It was unclear if the ∼15 previously known Class 0 and I disks, which have comparable radii to Class II disks, were typical for the young embedded phases or if they were unusually large and hence rare objects. Evidence of disk scale magnetic fields and substructures in Class 0 and I disks had not been observed. We used the CARMA, VLA, and ALMA telescope arrays to examine ∼mm and ∼cm dust continuum towards Class 0 and I protostars to characterize disk properties in the youngest stages of star formation. We have examined many characteristics of Class 0 and I protostars including disk frequency, disk radii, dust populations, disk evolution, disk structure, the influence of magnetic fields, and the possible presence of planetesimals in the youngest disks.

6.1.1 The Frequency of Class 0 and I Protostellar Disks

We have more than doubled the number of probable Class 0 and I disks to-date with the dust continuum VANDAM survey. We find a total of 19 Class 0 and I candidate disks the Perseus molecular cloud with VLA data, raising the number of known disks from ∼15 to ∼34. Of our 19 candidate disks, 15 are in Class 0 protostars and 4 in Class I. The two largest candidate disks belong to Class 0 protostars. A larger proportion of Class 0 protostars have

candidate disks (35%) compared to Class I protostars (11%). There is a mild trend that more evolved sources, as gauged by bolometric temperature, have higher values of γ, the power-law of the inner-disk surface density; this means older sources appear to have more centrally concentrated 8 mm dust grain populations. This may be due to the 8 mm grains in older sources having more time to undergo radial drift towards the central protostar than younger sources, resulting in a steeper γ for more evolved sources.

Per-emb-14 has a $\sim$3$\times$ larger disk at 1.3 mm with a smaller grain population, evidence that our 8 mm data is a lower limit on true disk radius. Since our 8 mm data trace a population of larger dust grains which radially drift towards the protostar and are lower limits on true disk size, large disks at early times do not seem to be exceptionally rare. On the other hand, 76% of the Class 0 and I protostars do not have signs of disks within our 12 AU resolution limit. Since disk formation in protostars is expected to be a natural consequence of conservation of angular momentum during core collapse, this implies that at 8 mm most disks in the Class 0 and I phases are small (<10 AU). The population of small, unresolved disks may undergo stronger magnetic braking or be subject to other processes limiting disk growth. Clearly since we do find candidate disks in 19 Perseus sources, some phenomena is at play to allow disk growth at early times.

6.1.2 Dust Properties of Embedded Disks

By fitting the deprojected, azimuthally averaged, and radially binned VANDAM continuum data in u,v-space to a disk-shaped profile, we can begin to model dust disk properties in the Class 0 and I phases. Except for sources with envelope contamination or small asymmetric features, the residuals of the model are near zero. For most sources, the major axis of the candidate disk is roughly perpendicular to the outflow axis (a proxy for the rotation axis), as expected for rotating protostellar disks. Most disks have best-fit models with q <0.5, typical for embedded disks, and values of γ are lower for Class 0 and I candidate disks than in Class II disks. Modeled radii of the candidate disks are somewhat large at 8 mm and comparable

to known Class 0 disk radii known from kinematics at ∼mm wavelengths. Our estimated masses of the candidate disks are large compared to masses of known Class 0 and Class I disks, indicating that our assumed value of dust opacity spectral index $\beta = 1$ is too large. Even with our simple modeling, we have revealed a great number of typical disk properties during the Class 0 and I stages.

We also conducted a search for dust substructures in a Class I disk to study disk sculpting mechanisms at work during the earliest possible phases of the star formation process. Modeling of long-baseline ALMA dust continuum observations of the Class I protostar IRS 63 has revealed two clear gaps at 16.1 and 31.8 AU, the first rings and gaps detected in a disk younger than the Class II phase. A third gap was detected with only a 1.5σ detection level and is not found when azimuthally averaging the filtered image intensity profiles. It is unclear if the outer gap, with a detection of only 1.5σ, is simply a noise artifact due to limited sensitivity near the edge of the dust disk or is a real detection. While it is tempting to immediately attribute rings and gaps to nascent planet-disk interactions, it is important to keep in mind that other phenomena such as volatile snowlines, dead zones, and gravitational instabilities can produce ring and gap structures in protostellar disks. In any case, the detection of substructures already formed in the disk around the Class I protostar IRS 63 are far-reaching, indicating that substructures are likely ubiquitous across many stages of protostellar evolution. The properties of the rings in gaps of IRS 63 will provide information regarding the initial conditions for planetesimal growth, chemical freeze-out in the disk, and presence of instabilities in disks around protostars at early times.

6.1.3 Magnetic Fields in Disks at Early Times

With CARMA observations of L1527, we have made the first resolved observations of dust polarization in a Class 0 protostellar disk. In addition to grain alignment with the magnetic field, scattering and radiative alignment of dust grains have been proposed as mechanisms to produce dust polarization in disks. Because Class 0 disks appear to be geometrically thick,

their (sub)millimeter sized dust populations may not be fully settled into the midplane of the disk. The midplane of the disk has high gas density, and magnetically aligned grains in the midplane can become quickly unaligned due to gaseous dampening; however, dust further from the midplane, where gas is less dense, may be able to align with magnetic fields in the Class 0 phase and produce a polarization signal. While scattering and radiative alignment may still play a role in producing polarization in the disks of Class 0 protostars, alignment with the magnetic field cannot be ruled out in the Class 0 stage.

For the Class 0 disk of L1527, if we assume the extreme case of polarization signal due only to alignment with the magnetic field, the inferred magnetic field is consistent with a dominantly toroidal morphology; there is no significantly detected vertical poloidal component to which observations of an edge-on disk are most sensitive. This suggests that angular momentum transport in Class 0 protostars (when large amounts of material are fed down to the disk from the envelope and accreted onto the protostar) is driven mainly by magnetorotational instability rather than magnetocentrifugal winds at 50 AU scales. In addition, with the data to-date there is an early, tentative trend that R >30 AU disks have so far been found in Class 0 systems with average magnetic fields on the 1000 AU scale strongly misaligned with the rotation axis. If this is the case, this implies that candidate Class 0 disk systems could be identified by the average magnetic field direction at $\sim$1000 AU spatial scales.

In the VANDAM survey, seven of the 19 candidate disk sources also have polarization detections. Six of the seven candidate disks with polarized emission also have inferred magnetic field morphologies misaligned with the rotation axes of the systems. NGC 1333 IRAS 4A has both aligned and unaligned scenarios, depending on the resolution of the polarized data, yet the data is consistent on small scales with a rotating disk. The only candidate disk that fully breaks this trend is IC348 MMS, which only has aligned inferred magnetic fields and outflows, yet has a relatively large disk for this scenario. It is possible that the polarized emission from IC348 MMS is not tracing magnetic field lines at all but is

instead due to scattering or radiative alignment. Together with the CARMA observations of L1527's magnetic field, the trend of disks being found in systems with misaligned orientations is strengthened. Inferred magnetic field orientation in the envelope misaligned with outflows of Class 0 protostars may truly be an observational signpost for large embedded disks on smaller scales.

6.2 Work in Progress

6.2.1 VANDAM Survey

8 mm Continuum Disk + Envelope Model

In addition to the disk only model, we will fit another model to the data that includes both disk and envelope components. We expect the high-resolution observations to spatially filter out most of the contaminating envelope emission from the source, with our VANDAM observations dominated by emission from the disk. Fitting a model with both disk and envelope components will allow us to determine the maximum contribution the envelope emission has relative to the contribution from the disk in each source. For a few sources, such as NGC 1333 IRAS4A and NGC 1333 IRAS4B, we detect a significant envelope component in the dust emission and a combined model will better fit candidate disk parameters. We will also subtracted a lower-limit free-free point source component in the same manner as the disk only model.

For each source we will include the same disk model component as given by Equation 4.2 in addition to a spherically symmetric envelope component. The model envelope surface brightness profile will be given by

$$I(r)_{env} \propto (r)^{-p}, \tag{6.1}$$

where $I(r)_{env}$ is the radial surface brightness distribution of the envelope, and p incorporates

contributions from the envelope density and the envelope temperature structure. The sum of $I(r)_{disk}$ and $I(r)_{env}$ will be constrained to be equal to the zero-baseline flux of each modeled source. Because the disk + envelope model will mainly be used to estimate the relative level of envelope vs. disk emission, to save on computational time and avoid over-fitting marginally resolved sources, we will fix the disk parameter $q = 0.50$ and set $p = [1.5, 2.0]$. Based on the disk-only modeling (Table 4.3), varying q should not substantially change the corresponding R_c, and $q = 0.50$ is typical for protoplanetary disks from analytic models for accretion disks. Values of $p = [1.5, 2.0]$ correspond, respectively, to envelope density profiles of free-fall collapse and a singular isothermal sphere (Shu, 1977).

Quantifying the Smallest Recoverable Disk Radius

To quantify the minimum detectable disk radius we are able to recover with our model, we will make synthetic observations of disks with R <12 AU. We will convolve the synthetic observation with a beam and add a noise component that matches our data. We will fit the synthetic observations with our standard modeling procedure in the u,v-plane (Section 4.4) and determine if we can recover the radius we originally used to generate the synthetic disk. A family of synthetic disks will be required with varying radii and flux, as brighter sources with smaller radii could potentially be recovered while dimmer sources with larger radii may not. In this manner we will determine the smallest recoverable disk radius our modeling can achieve, given the resolution and sensitivity limitations of our data.

Minor Refinements to Image-Plane Initial Estimates of Candidate Disk Parameters

Minor changes to the initial estimates of our candidate disk parameters from the image plane may, in a few instances, improve our modeling results. Per-emb-63 is one of the least bright candidate disk sources and the point source component estimate is likely grossly overestimated from long baselines due to the ringing in the visibility profile. A better-fit disk

model for Per-emb-63 may be found by simply setting the point source component to zero. In NGC 1333 IRAS4B, we see a slight offset between the center of the 8 mm candidate disk and the center of the model. The off-center fit causes an over-subtraction of the east side of the candidate disk and an under-subtraction on the west side of the candidate disk. We can refine this model by recentering the 8 mm data to align with phase center in the u,v-data.

6.2.2 IRS 63 Gap Modeling

With Class I protostar IRS 63, we will be able to definitively study initial conditions for planetesimal growth, chemical freeze-out in the disk, and presence of instabilities in disks around protostars at earlier times than ever examined observationally before. We have only just begun to model the rings and gaps in the disk of IRS 63 with the most simple estimates of disk parameters, with more detailed modeling to follow. By modeling the rings and gaps, we hope to definitively determine if the substructure is from symmetric gaps carved by planets or if it is caused by some other mechanism involving grain growth at early times. Since clear gaps are seen in the observations, with more precise modeling we will be able to quantitatively compare gap parameters to the HL Tau observations. Modeling in both the image and u,v-planes will allow for stronger understanding of gap properties such as gap width, in-gap flux, and azimuthal asymmetries. Gap properties will allow us to address planetesimal orbital resonances, planetesimal masses, and instabilities (see Kwon et al., 2011). We will use MCMC dust emission modeling of the disk to look for any substructure (e.g., Kwon et al., 2011, 2015; Chiang et al., 2012), and also for fitting disk properties that will allow us to compare our observations to other protostellar disks.

References

Adams, F. C., Lada, C. J., & Shu, F. H. 1987, ApJ, 312, 788

Allen, A., Shu, F., Li, Z.-Y., Choi, M., & Chuang, H.-W. 2003, in IAU Symposium, Vol. 221, IAU Symposium

ALMA Partnership, Brogan, C. L., Pérez, L. M., et al. 2015, ApJ, 808, L3

Andre, P., Ward-Thompson, D., & Barsony, M. 1993, ApJ, 406, 122

—. 2000, Protostars and Planets IV, 59

Andrews, S. M., & Williams, J. P. 2005, ApJ, 631, 1134

Andrews, S. M., Wilner, D. J., Hughes, A. M., Qi, C., & Dullemond, C. P. 2009, ApJ, 700, 1502

—. 2010, ApJ, 723, 1241

Andrews, S. M., Wilner, D. J., Zhu, Z., et al. 2016, ApJ, 820, L40

Anglada, G., Villuendas, E., Estalella, R., et al. 1998, AJ, 116, 2953

Arce, H. G., & Sargent, A. I. 2006, ApJ, 646, 1070

Armitage, P. J. 2011, ARA&A, 49, 195

Aspin, C., Sandell, G., & Russell, A. P. G. 1994, A&AS, 106

Bachiller, R., & Cernicharo, J. 1986, A&A, 168, 262

Bachiller, R., Guilloteau, S., Gueth, F., et al. 1998, A&A, 339, L49

Bachiller, R., Martin-Pintado, J., & Planesas, P. 1991, A&A, 251, 639

Bachiller, R., Menten, K. M., & del Rio Alvarez, S. 1990, A&A, 236, 461

Balbus, S. A., & Hawley, J. F. 1998, Reviews of Modern Physics, 70, 1

Baruteau, C., & Papaloizou, J. C. B. 2013, ApJ, 778, 7

Birnstiel, T., Ricci, L., Trotta, F., et al. 2010, A&A, 516, L14

Blake, G. A., & Bergin, E. A. 2015, Nature, 520, 161

Blandford, R. D., & Payne, D. G. 1982, MNRAS, 199, 883

Brinch, C., & Jørgensen, J. K. 2013, A&A, 559, A82

Bromley, B. C., & Kenyon, S. J. 2011, ApJ, 731, 101

Calvet, N., D'Alessio, P., Watson, D. M., et al. 2005, ApJ, 630, L185

Casassus, S., Hales, A., de Gregorio, I., et al. 2013, A&A, 553, A64

Cassen, P., & Moosman, A. 1981, Icarus, 48, 353

Chen, H., Myers, P. C., Ladd, E. F., & Wood, D. O. S. 1995, ApJ, 445, 377

Chen, X., Launhardt, R., & Henning, T. 2007, ApJ, 669, 1058

Chen, X., Arce, H. G., Zhang, Q., et al. 2013, ApJ, 768, 110

Chiang, E. I., & Goldreich, P. 1997, ApJ, 490, 368

Chiang, H.-F., Looney, L. W., Tassis, K., Mundy, L. G., & Mouschovias, T. C. 2008, ApJ, 680, 474

Chiang, H.-F., Looney, L. W., & Tobin, J. J. 2012, ApJ, 756, 168

Chini, R., Reipurth, B., Sievers, A., et al. 1997, A&A, 325, 542

Cho, J., & Lazarian, A. 2007, ApJ, 669, 1085

Cieza, L. A., Casassus, S., Tobin, J., et al. 2016, Nature, 535, 258

Codella, C., Cabrit, S., Gueth, F., et al. 2014, A&A, 568, L5

Cohen, M. 1980, AJ, 85, 29

Coughlin, J. L., Mullally, F., Thompson, S. E., et al. 2016, ApJS, 224, 12

Cox, E. G., Harris, R. J., Looney, L. W., et al. 2015, ApJ, 814, L28

Crutcher, R. M. 2012, ARA&A, 50, 29

Curtis, E. I., Richer, J. S., Swift, J. J., & Williams, J. P. 2010, MNRAS, 408, 1516

D'Alessio, P. 1996, PhD thesis, Instituto de Astronomía, UNAM, Apartado Postal 70-264, Ciudad Univesitaria, CP. 04510, México 20, D. F., México

Dapp, W. B., & Basu, S. 2010, A&A, 521, L56

Dapp, W. B., Basu, S., & Kunz, M. W. 2012, A&A, 541, A35

Davidson, J. A., Novak, G., Matthews, T. G., et al. 2011, ApJ, 732, 97

Davidson, J. A., Li, Z.-Y., Hull, C. L. H., et al. 2014, ApJ, 797, 74

Davis, C. J., Scholz, P., Lucas, P., Smith, M. D., & Adamson, A. 2008, MNRAS, 387, 954

Di Francesco, J., Myers, P. C., Wilner, D. J., Ohashi, N., & Mardones, D. 2001, ApJ, 562, 770

Dong, R., & Dawson, R. 2016, ApJ, 825, 77

Dullemond, C. P., & Dominik, C. 2004, A&A, 417, 159

Dunham, M. M., Arce, H. G., Mardones, D., et al. 2014a, ApJ, 783, 29

Dunham, M. M., Stutz, A. M., Allen, L. E., et al. 2014b, Protostars and Planets VI, 195

Eislöffel, J., Froebrich, D., Stanke, T., & McCaughrean, M. J. 2003, ApJ, 595, 259

Eisner, J. A. 2012, ApJ, 755, 23

Engargiola, G., & Plambeck, R. L. 1999, in The Physics and Chemistry of the Interstellar Medium, ed. V. Ossenkopf, J. Stutzki, & G. Winnewisser

Enoch, M. L., Evans, II, N. J., Sargent, A. I., & Glenn, J. 2009, ApJ, 692, 973

Enoch, M. L., Corder, S., Duchêne, G., et al. 2011, ApJS, 195, 21

Espaillat, C., Calvet, N., D'Alessio, P., et al. 2007, ApJ, 670, L135

Espaillat, C., Calvet, N., Luhman, K. L., Muzerolle, J., & D'Alessio, P. 2008, ApJ, 682, L125

Flock, M., Ruge, J. P., Dzyurkevich, N., et al. 2015, A&A, 574, A68

Foreman-Mackey, D., Hogg, D. W., Lang, D., & Goodman, J. 2013, PASP, 125, 306

Girart, J. M., Rao, R., & Marrone, D. P. 2006, Science, 313, 812

Goodman, J., & Weare, J. 2010, Communications in Applied Mathematics and Computational Science, Vol. 5, No. 1, p. 65-80, 2010, 5, 65

Grossman, E. N., Masson, C. R., Sargent, A. I., et al. 1987, ApJ, 320, 356

Gueth, F., & Guilloteau, S. 1999, A&A, 343, 571

Guilloteau, S., Piétu, V., Chapillon, E., et al. 2016, A&A, 586, L1

Gutermuth, R. A., Myers, P. C., Megeath, S. T., et al. 2008, ApJ, 674, 336

Harsono, D., Jørgensen, J. K., van Dishoeck, E. F., et al. 2014, A&A, 562, A77

Hatchell, J., & Dunham, M. M. 2009, A&A, 502, 139

Hatchell, J., Richer, J. S., Fuller, G. A., et al. 2005, A&A, 440, 151

Hayashi, C. 1966, ARA&A, 4, 171

Hennebelle, P., & Ciardi, A. 2009, A&A, 506, L29

Hennebelle, P., & Fromang, S. 2008, A&A, 477, 9

Herbig, G. H. 1962, Advances in Astronomy and Astrophysics, 1, 47

—. 1977, ApJ, 217, 693

—. 1998, ApJ, 497, 736

Hildebrand, R. H. 1983, QJRAS, 24, 267

Hirota, T., Honma, M., Imai, H., et al. 2011, PASJ, 63, 1

Hirota, T., Bushimata, T., Choi, Y. K., et al. 2008, PASJ, 60, 37

Hughes, A. M., Hull, C. L. H., Wilner, D. J., & Plambeck, R. L. 2013, AJ, 145, 115

Hughes, A. M., Andrews, S. M., Espaillat, C., et al. 2009, ApJ, 698, 131

Hull, C. L. H., Plambeck, R. L., Bolatto, A. D., et al. 2013, ApJ, 768, 159

Hull, C. L. H., Plambeck, R. L., Kwon, W., et al. 2014, ApJS, 213, 13

Isella, A., Guidi, G., Testi, L., et al. 2016, Physical Review Letters, 117, 251101

Jennings, R. E., Cameron, D. H. M., Cudlip, W., & Hirst, C. J. 1987, MNRAS, 226, 461

Jin, S., Li, S., Isella, A., Li, H., & Ji, J. 2016, ApJ, 818, 76

Joos, M., Hennebelle, P., & Ciardi, A. 2012, A&A, 543, A128

Joos, M., Hennebelle, P., Ciardi, A., & Fromang, S. 2013, A&A, 554, A17

Jørgensen, J. K., Hogerheijde, M. R., van Dishoeck, E. F., Blake, G. A., & Schöier, F. L. 2004, A&A, 413, 993

Jørgensen, J. K., van Dishoeck, E. F., Visser, R., et al. 2009, A&A, 507, 861

Jørgensen, J. K., Harvey, P. M., Evans, II, N. J., et al. 2006, ApJ, 645, 1246

Jørgensen, J. K., Bourke, T. L., Myers, P. C., et al. 2007, ApJ, 659, 479

Joy, A. H. 1942, PASP, 54, 15

—. 1945, ApJ, 102, 168

—. 1949, ApJ, 110, 424

Kanagawa, K. D., Muto, T., Tanaka, H., et al. 2015, ApJ, 806, L15

Kataoka, A., Machida, M. N., & Tomisaka, K. 2012, ApJ, 761, 40

Kataoka, A., Muto, T., Momose, M., et al. 2015, ApJ, 809, 78

Konigl, A., & Pudritz, R. E. 2000, Protostars and Planets IV, 759

Krumholz, M. R., Crutcher, R. M., & Hull, C. L. H. 2013, ApJ, 767, L11

Kwon, W., Looney, L. W., Crutcher, R. M., & Kirk, J. M. 2006, ApJ, 653, 1358

Kwon, W., Looney, L. W., & Mundy, L. G. 2011, ApJ, 741, 3

Kwon, W., Looney, L. W., Mundy, L. G., & Welch, W. J. 2015, ApJ, 808, 102

Lada, C. J. 1987, in IAU Symposium, Vol. 115, Star Forming Regions, ed. M. Peimbert & J. Jugaku, 1–17

Lada, C. J., Alves, J., & Lada, E. A. 1996, AJ, 111, 1964

Lada, C. J., & Wilking, B. A. 1984, ApJ, 287, 610

Ladd, E. F., Lada, E. A., & Myers, P. C. 1993, ApJ, 410, 168

Lay, O. P., Carlstrom, J. E., & Hills, R. E. 1995, ApJ, 452, L73

Lazarian, A. 2007, J.Quant.Spec.Radiat.Transf., 106, 225

Lee, C.-F., Ho, P. T. P., Li, Z.-Y., et al. 2017, Nature Astronomy, 1, 0152

Lee, C.-F., Mundy, L. G., Stone, J. M., & Ostriker, E. C. 2002, ApJ, 576, 294

Lee, C.-F., Rao, R., Ching, T.-C., et al. 2014, ApJ, 797, L9

Lee, K. I., Dunham, M. M., Myers, P. C., et al. 2015, ApJ, 814, 114

—. 2016, ApJ, 820, L2

Li, Z.-Y., Banerjee, R., Pudritz, R. E., et al. 2014, Protostars and Planets VI, 173

Li, Z.-Y., Krasnopolsky, R., & Shang, H. 2011, ApJ, 738, 180

—. 2013, ApJ, 774, 82

Loinard, L., Chandler, C. J., Rodríguez, L. F., et al. 2007, ApJ, 670, 1353

Lommen, D., Jørgensen, J. K., van Dishoeck, E. F., & Crapsi, A. 2008, A&A, 481, 141

Loomis, R. A., Öberg, K. I., Andrews, S. M., & MacGregor, M. A. 2017, ApJ, 840, 23

Looney, L. W., Mundy, L. G., & Welch, W. J. 2000, ApJ, 529, 477

Machida, M. N., Inutsuka, S.-I., & Matsumoto, T. 2011, PASJ, 63, 555

Machida, M. N., Inutsuka, S.-i., & Matsumoto, T. 2014, MNRAS, 438, 2278

Marvel, K. B., Wilking, B. A., Claussen, M. J., & Wootten, A. 2008, ApJ, 685, 285

Matthews, B. C., McPhee, C. A., Fissel, L. M., & Curran, R. L. 2009, ApJS, 182, 143

Maury, A. J., André, P., Hennebelle, P., et al. 2010, A&A, 512, A40

McCaughrean, M. J., Rayner, J. T., & Zinnecker, H. 1994, ApJ, 436, L189

McKee, C. F., & Ostriker, E. C. 2007, ARA&A, 45, 565

Mellon, R. R., & Li, Z.-Y. 2008, ApJ, 681, 1356

—. 2009, ApJ, 698, 922

Movsessian, T. A., Magakian, T. Y., Sargsyan, D. M., & Ogura, K. 2012, Astrophysics, 55, 471

Murillo, N. M., & Lai, S.-P. 2013, ApJ, 764, L15

Murillo, N. M., Lai, S.-P., Bruderer, S., Harsono, D., & van Dishoeck, E. F. 2013, A&A, 560, A103

Myers, P. C., & Ladd, E. F. 1993, ApJ, 413, L47

Ohashi, N., Saigo, K., Aso, Y., et al. 2014, ApJ, 796, 131

O'Linger, J. C., Cole, D. M., Ressler, M. E., & Wolf-Chase, G. 2006, AJ, 131, 2601

Ossenkopf, V., & Henning, T. 1994, A&A, 291, 943

Padovani, M., Brinch, C., Girart, J. M., et al. 2012, A&A, 543, A16

Pech, G., Zapata, L. A., Loinard, L., & Rodríguez, L. F. 2012, ApJ, 751, 78

Pérez, L. M., Isella, A., Carpenter, J. M., & Chandler, C. J. 2014, ApJ, 783, L13

Pérez, L. M., Carpenter, J. M., Chandler, C. J., et al. 2012, ApJ, 760, L17

Pérez, L. M., Carpenter, J. M., Andrews, S. M., et al. 2016, Science, 353, 1519

Piétu, V., Dutrey, A., Guilloteau, S., Chapillon, E., & Pety, J. 2006, A&A, 460, L43

Pinilla, P., de Juan Ovelar, M., Ataiee, S., et al. 2015, A&A, 573, A9

Pinilla, P., Flock, M., Ovelar, M. d. J., & Birnstiel, T. 2016, A&A, 596, A81

Pinilla, P., Pohl, A., Stammler, S. M., & Birnstiel, T. 2017, ArXiv e-prints, arXiv:1707.02321

Pinte, C., Dent, W. R. F., Ménard, F., et al. 2016, ApJ, 816, 25

Plunkett, A. L., Arce, H. G., Corder, S. A., et al. 2013, ApJ, 774, 22

Pollack, J. B., Hubickyj, O., Bodenheimer, P., et al. 1996, Icarus, 124, 62

Rao, R., Girart, J. M., Lai, S.-P., & Marrone, D. P. 2014, ApJ, 780, L6

Rebull, L. M., Stapelfeldt, K. R., Evans, II, N. J., et al. 2007, ApJS, 171, 447

Reipurth, B., Rodríguez, L. F., Anglada, G., & Bally, J. 2002, AJ, 124, 1045

Rodríguez, L. F., Anglada, G., & Curiel, S. 1999, ApJS, 125, 427

Rodríguez, L. F., Zapata, L. A., & Palau, A. 2014, ApJ, 790, 80

Ros, K., & Johansen, A. 2013, A&A, 552, A137

Sadavoy, S. I., Di Francesco, J., André, P., et al. 2014, ApJ, 787, L18

Sakai, N., Oya, Y., Higuchi, A. E., et al. 2017, MNRAS, 467, L76

Sandell, G., Aspin, C., Duncan, W. D., Russell, A. P. G., & Robson, E. I. 1991, ApJ, 376, L17

Sandell, G., & Knee, L. B. G. 2001, ApJ, 546, L49

Sandell, G., Knee, L. B. G., Aspin, C., Robson, I. E., & Russell, A. P. G. 1994, A&A, 285

Santangelo, G., Codella, C., Cabrit, S., et al. 2015, A&A, 584, A126

Sault, R. J., Teuben, P. J., & Wright, M. C. H. 1995, in Astronomical Society of the Pacific Conference Series, Vol. 77, Astronomical Data Analysis Software and Systems IV, ed. R. A. Shaw, H. E. Payne, & J. J. E. Hayes, 433

Schnee, S., Di Francesco, J., Enoch, M., et al. 2012, ApJ, 745, 18

Segura-Cox, D. M., Looney, L. W., Stephens, I. W., et al. 2015, ApJ, 798, L2

Segura-Cox, D. M., Harris, R. J., Tobin, J. J., et al. 2016, ApJ, 817, L14

Seifried, D., Banerjee, R., Pudritz, R. E., & Klessen, R. S. 2013, MNRAS, 432, 3320

Shakura, N. I., & Sunyaev, R. A. 1973, A&A, 24, 337

Shu, F. H. 1977, ApJ, 214, 488

Snell, R. L., Loren, R. B., & Plambeck, R. L. 1980, ApJ, 239, L17

Stephens, I. W., Looney, L. W., Kwon, W., et al. 2013, ApJ, 769, L15

—. 2014, Nature, 514, 597

Storm, S., Mundy, L. G., Fernández-López, M., et al. 2014, ApJ, 794, 165

Strom, K. M., Strom, S. E., & Vrba, F. J. 1976, AJ, 81, 308

Takahashi, S. Z., & Inutsuka, S.-i. 2014, ApJ, 794, 55

—. 2016, AJ, 152, 184

Takakuwa, S., Saito, M., Lim, J., et al. 2012, ApJ, 754, 52

Tazaki, R., Lazarian, A., & Nomura, H. 2017, ApJ, 839, 56

Tazzari, M., Testi, L., Natta, A., et al. 2017, ArXiv e-prints, arXiv:1707.01499

Terebey, S., & Padgett, D. L. 1997, in IAU Symposium, Vol. 182, Herbig-Haro Flows and the Birth of Stars, ed. B. Reipurth & C. Bertout, 507–514

Terebey, S., Shu, F. H., & Cassen, P. 1984, ApJ, 286, 529

Tobin, J. J., Hartmann, L., Calvet, N., & D'Alessio, P. 2008, ApJ, 679, 1364

Tobin, J. J., Hartmann, L., Chiang, H.-F., et al. 2012, Nature, 492, 83

—. 2013a, ApJ, 771, 48

—. 2011, ApJ, 740, 45

Tobin, J. J., Bergin, E. A., Hartmann, L., et al. 2013b, ApJ, 765, 18

Tobin, J. J., Chandler, C. J., Wilner, D. J., et al. 2013c, ApJ, 779, 93

Tobin, J. J., Looney, L. W., Wilner, D. J., et al. 2015a, ApJ, 805, 125

Tobin, J. J., Dunham, M. M., Looney, L. W., et al. 2015b, ApJ, 798, 61

Tobin, J. J., Kratter, K. M., Persson, M. V., et al. 2016a, Nature, 538, 483

Tobin, J. J., Looney, L. W., Li, Z.-Y., et al. 2016b, ApJ, 818, 73

van der Marel, N., Kristensen, L. E., Visser, R., et al. 2013, A&A, 556, A76

Weidenschilling, S. J. 1977, MNRAS, 180, 57

Welch, W. J., Hartmann, L., Helfer, T., & Briceño, C. 2000, ApJ, 540, 362

Wilking, B. A., & Lada, C. J. 1983, ApJ, 274, 698

Williams, J. P., & Cieza, L. A. 2011, ARA&A, 49, 67

Wolf, S., & D'Angelo, G. 2005, ApJ, 619, 1114

Wootten, A., & Mangum, J. 1993, in Bulletin of the American Astronomical Society, Vol. 25, American Astronomical Society Meeting Abstracts, 1367

Yang, H., Li, Z.-Y., Looney, L. W., et al. 2016, MNRAS, 460, 4109

Yang, H., Li, Z.-Y., Looney, L. W., Girart, J. M., & Stephens, I. W. 2017, ArXiv e-prints, arXiv:1705.05432

Yen, H.-W., Koch, P. M., Takakuwa, S., et al. 2015, ApJ, 799, 193

—. 2017, ApJ, 834, 178

Young, K. E., Young, C. H., Lai, S.-P., Dunham, M. M., & Evans, II, N. J. 2015, AJ, 150, 40

Zhang, K., Bergin, E. A., Blake, G. A., et al. 2016, ApJ, 818, L16

Zhang, K., Blake, G. A., & Bergin, E. A. 2015, ApJ, 806, L7